

# REPORT DOCUMENTATION PAGE

Form Approved  
OMB NO. 0704-0188

Public Reporting burden for this collection of information is estimated to average 1 hour per response, including the time for reviewing instructions, searching existing data sources, gathering and maintaining the data needed, and completing and reviewing the collection of information. Send comment regarding this burden estimates or any other aspect of this collection of information, including suggestions for reducing this burden, to Washington Headquarters Services, Directorate for Information Operations and Reports, 1215 Jefferson Davis Highway, Suite 1204, Arlington, VA 22202-4302, and to the Office of Management and Budget, Paperwork Reduction Project (0704-0188), Washington, DC 20503.

1. AGENCY USE ONLY (Leave Blank)		2. REPORT DATE 31 July 2005		3. REPORT TYPE AND DATES COVERED Final 1 Oct 01-31 July 05	
4. TITLE AND SUBTITLE Modeling of Beam Wave Pulse Propagation in Vegetation using Transport Theory				5. FUNDING NUMBERS DAAD190110755	
6. AUTHOR(S) Gerald M. Whitman, Felix K. Schwering, Michael Yu-Chi Wu				2005 JUL 29 PM 3:37	
7. PERFORMING ORGANIZATION NAME(S) AND ADDRESS(ES) New Jersey Institute of Technology 323 Martin Luther King Boulevard Newark, NJ 07102					
8. PERFORMING ORGANIZATION REPORT NUMBER					
9. SPONSORING / MONITORING AGENCY NAME(S) AND ADDRESS(ES) U. S. Army Research Office P.O. Box 12211 Research Triangle Park, NC 27709-2211				10. SPONSORING / MONITORING AGENCY REPORT NUMBER 43052EL 01	
11. SUPPLEMENTARY NOTES The views, opinions and/or findings contained in this report are those of the author(s) and should not be construed as an official Department of the Army position, policy or decision, unless so designated by other documentation.					
12 a. DISTRIBUTION / AVAILABILITY STATEMENT Approved for public release; distribution unlimited.				12 b. DISTRIBUTION CODE	
13. ABSTRACT (Maximum 200 words) The scalar time-dependent equation of radiative transfer in cylindrical coordinates was used to develop several new theories- both rigorous and approximate- for propagation and scattering of beam wave pulse trains in vegetation modeled as a random medium of discrete scatterers. Plots of specific intensity and received power in the random medium (vegetation) showed distortion due to pulse broadening, angular spread, power attenuation (especially at large penetration depths), and out-of-beam scattering. To allow for near- real- time modeling (of interest to the soldier in the field), three new approximate theories for beam wave propagation in vegetation were developed and numerically compared to the rigorous theory. A first order theory was shown to agree with the rigorous theory at short vegetation penetration depths; at larger depths, it agrees in the forward scatter direction only, but not otherwise. An asymptotic theory was shown to have the correct behavior in all scatter directions and to agree with the rigorous theory at large penetration depths. The third approximate theory was a composite solution which combined both the first order solution and the asymptotic solution and closed the gap between the first two approximate theories.					
14. SUBJECT TERMS Pulsed beam wave, propagation and scattering in vegetation, transport theory, reduced incident and diffuse intensity, random medium				15. NUMBER OF PAGES 84	
				16. PRICE CODE	
17. SECURITY CLASSIFICATION OR REPORT UNCLASSIFIED	18. SECURITY CLASSIFICATION ON THIS PAGE UNCLASSIFIED	19. SECURITY CLASSIFICATION OF ABSTRACT UNCLASSIFIED	20. LIMITATION OF ABSTRACT UL		

NSN 7540-01-280-5500

Standard Form 298 (Rev.2-89)  
Prescribed by ANSI Std. Z39-18  
298-102

Enclosure 1

**MODELING OF BEAM WAVE PULSE PROPAGATION IN VEGETATION  
USING TRANSPORT THEORY**

**By**

**Gerald M. Whitman  
Felix K. Schwering  
Michael Yu-Chi Wu**

**DISTRIBUTION STATEMENT A**  
Approved for Public Release  
Distribution Unlimited

**July 31, 2005**

**FINAL REPORT**

**New Jersey Institute of Technology**



## STATEMENT OF PROBLEM

The general problem being addressed in this investigation is how to develop accurate theoretical models for microwave and millimeter-wave propagation and scattering in vegetation. Such models are needed since vegetation along the propagation channel contributes to many problems and limitations that affect mobile radio systems. Of particular interest to the US Army is the development of models that provide real time data to the soldier in the field. Hence, both rigorous and approximate models are of interest.

At frequencies above 3GHz, the wavelength is of the order of, or small compared to, the dimensions and spacings of vegetation, such as leaves, twigs and branches. Vegetation has to be modeled as a random medium of discrete, lossy scatterers. Multiscattering is important and both the coherent and incoherent field components have to be taken into account. To account for these characteristics, the theoretical models developed here for propagation and scattering in vegetation at high frequency are based on radiative energy transfer theory (transport theory).

The specific problem analyzed is that of a periodic sequence of Gaussian pulses incident from free space (air) onto a forest region (vegetation). The forest is modeled as a half-space of randomly distributed particles that scatter and absorb electromagnetic energy. The incident pulse train is taken to be either a collimated (cylindrical) wave beam, which is pertinent for IR and optical communications, or a spherical wave that is confined within a certain solid angle, which is characteristic of radiation produced by a microwave or mm-wave antenna.

## SUMMARY OF THE MOST IMPORTANT RESULTS

The major contribution of this study is the development of several new theories - both rigorous and approximate - capable of characterizing the propagation and scattering of microwave and millimeter-wave pulsed beam waves in vegetation. These theories allowed for a comprehensive characterization of the influence of vegetation on the propagation of beam waves, which included a description of their attenuation, their angular spread, their distortion due to pulse broadening, and the determination of out-of-the-beam scattering.

The theories are based on solutions to the equation of radiative transfer in cylindrical coordinates. Such theories are new and provide better understanding of the effects of vegetation in the propagation channel. Two cases are considered. The first case deals with an incident collimated beam wave pulse train that enters a forest half-space. The second case assumes that the incident radiation upon the forest is a diverging spherical beam wave. In both cases, vegetation is modeled as a random medium of discrete scatterers.

To allow for real time determination of the attenuation and scattering of the field in vegetation, three approximate theories for both the collimated and spherical beams are developed. The first theory, a first order multiple scattering theory, allows estimation of the intensity at small penetration depths without resorting to computer intensive calculations while maintaining good accuracy. The second new theory yields an asymptotic solution to the transport equation, which is valid at large penetration depths into the forest. This allows a characterization of the field deep in the forest also without extensive calculations. The third theory, which combines the latter two approximate theories, attempts to close the gap between the first order theory and the asymptotic theory. As opposed to the rigorous theories, these approximate theories have been found to be numerically efficient. The importance of these approximate theories is that they provide real-time information to the soldier in the field quickly as opposed to the rigorous theory which, being computationally intensive, is time consuming.



## TABLE OF CONTENT

1. INTRODUCTION .....	1
2. FORMULATION .....	3
2.1 Incident Gaussian Beam Wave Pulse Train .....	3
2.2 Phase Function .....	5
2.3 The Scalar Time-Dependent Transport Equation in Cylindrical Coordinates .....	6
3. RIGOROUS SOLUTION FOR COLLIMATED BEAM WAVE.....	8
3.1 Homogeneous Solution .....	13
3.2 Particular Solution .....	13
3.4 Power Received by a Highly Directive Antenna in the Forest.....	16
4. RIGOROUS SOLUTION FOR SPHERICAL BEAM WAVE.....	20
4.1 Particular Solution .....	22
4.1.1 The Fourier-Cosine Approach.....	22
4.1.2 Finite Difference Solution.....	24
5. APPROXIMATE SOLUTIONS OF THE TIME-INDEPENDENT TRANSPORT EQUATION.....	26
5.1 Introduction.....	26
5.2 First order Multiple Scattering Solution .....	26
5.2.1 Collimated Beam .....	27
5.2.2 Spherical Beam.....	28
5.3 Asymptotic Solution .....	29
5.3.1 Case 1 .....	29
5.3.2 Case 2 .....	30
5.4 Composite Approximate Solution.....	31
5.4.1 Collimated and Spherical Beams.....	32
6. NUMERICAL RESULTS .....	34
6.1 Introduction.....	34
6.2 Scatter or Phase Function .....	34
6.3 Convergence in Received Diffuse Power .....	34
6.4 Comparisons with Quadrature Method .....	35
6.5 Additional Considerations.....	36
6.6 Boundary Condition .....	37
6.7 Power Attenuation, Pulse Broadening and Distortion.....	37
6.8 Angular Distribution of Diffuse Intensity .....	39
6.9 Approximate Solutions .....	39
7. CONCLUSION .....	42
8. REFERENCES .....	44

## TABLE OF FIGURES

<b>Figure 2.1</b>	Bounded beam wave pulse train incident onto a forest half-space.....	45
<b>Figure 2.2</b>	The basic geometry for scattering in the forest half-space of an incident beam wave pulse train. The "sphere" represents a scatter point in the forest. The tilted cylinder represents a receiving antenna, which is shown enlarged in Figure 2.3.....	46
<b>Figure 2.3</b>	The coordinate geometry of the receiving antenna, which is depicted as a tilted cylinder with a main beam direction $(\theta_M, \psi_M)$ ; note $\theta = \theta_M$ . ....	47
<b>Figure 5.1</b>	Geometry for asymptotic solution, case 2.....	48
<b>Figure 6.1</b>	Scatter or phase function $p(\gamma)$ simulated by using (2.18) and by (3.16) truncated at $N=31$ ...49	
<b>Figure 6.2</b>	Error analysis of the phase function, where $N'=N+1$ is the number of terms for the truncation of (3.16).....	50
<b>Figure 6.3</b>	Normalized received diffuse power $P_d'$ versus normalized time $t'$ for different values of $N$ for $w' \rightarrow \infty$ (plane wave), $\rho'=0$ , $z'=1$ , $\theta_M=0$ ( $\psi_M$ is undefined when $\rho'=0$ ), $v_{\max}=15$ . ....	51
<b>Figure 6.4</b>	Normalized received diffuse power $P_d'$ versus normalized time $t'$ for $N=23, 27, 39$ and $w'=10$ , $\rho'=0$ , $z'=1$ , $\theta_M=0$ , $v_{\max}=15$ .....	52
<b>Figure 6.5</b>	Normalized received diffuse power $P_d'$ versus normalized time $t'$ for different values of $\theta_M$ in the range $0^0 \leq \theta_M \leq 9^0$ and $w' \rightarrow \infty$ (plane wave), $\rho'=0$ , $z'=1$ , $v_{\max}=15$ , $N=31$ ....	53
<b>Figure 6.6</b>	Normalized received diffuse power $P_d'$ versus normalized time $t'$ for $w'=10$ , $\rho'=0$ , $z'=1$ , $\theta_M=0^0$ and $4.83^0$ , $v_{\max}=15$ , $N=39$ .....	54
<b>Figure 6.7</b>	Normalized received diffuse power $P_d'$ versus normalized time $t'$ for $w'=1, 10$ and $w' \rightarrow \infty$ (plane wave) with associated values of $N=31, 39$ and $47$ , respectively, and $\rho'=0$ , $z'=1$ , $\theta_M=0$ , $v_{\max}=15$ .....	55
<b>Figure 6.8</b>	Comparisons between Quadrature method (Q) and Spherical Harmonics-Hankel Transform method (S) of normalized received power $P'$ versus normalized time $t'$ for $z'=1, 3, 5, 10$ and $w'=1$ , $\rho'=0$ , $\theta_M=4.83^0$ , $v_{\max}=15$ , $N=31$ .....	56
<b>Figure 6.9</b>	Comparison between Quadrature method (Q) and Spherical Harmonics-Hankel Transform method (S) of the normalized received power $P'$ versus normalized time $t'$ for $w'=0.5, 1, 3, 5, \infty$ and $\rho'=0$ , $z'=1$ , $\theta_M=4.83^0$ , $v_{\max}=15$ , $N=27$ .....	57
<b>Figure 6.10</b>	Normalized reduced incident power $P_{ri}'$ versus normalized time $t'$ for $\rho'=0$ , $z'=1$ , $\theta_M=0$ for different values of $v_{\max}$ .....	58
<b>Figure 6.11</b>	Diffuse Intensity $I_{d,0}$ versus $\theta$ for $w'=10$ , $\rho'=0$ , $z'=0$ , $v=0$ and $N=23, 27, 31$ .....	59
<b>Figure 6.12</b>	Diffuse intensity $I_{d,0}$ versus $\theta$ for beamwidths $w'=0.5, 1, 2, 3, 5, 7, 10, \infty$ and $\rho'=0$ , $z'=0$ , $v=0$ , $N=31$ .....	60
<b>Figure 6.13</b>	Magnitude of diffuse intensity $ I_{d,1} $ versus $\theta$ for $w'=1, 2$ and $\rho'=0$ , $z'=0$ , $v=1$ , $N=31$ .....	61
<b>Figure 6.14</b>	Diffuse Intensity $I_{d,0}$ versus normalized penetration depth $z'$ for $w'=1$ , $\rho'=0$ , $\theta=0$ , $v=0$ , $N=31$ .....	62
<b>Figure 6.15</b>	Normalized received power $P'$ versus normalized time $t'$ for $\rho'$ varying from 0 to 5 and $w'=1$ , $z'=1$ , $\theta_M=0$ , $\psi_M=0$ , $v_{\max}=15$ , $N=31$ .....	63



<b>Figure 6.16</b>	Normalized received power $P'$ versus normalized time $t'$ for $\rho' = 0, 1, 2, 3$ and $w' = 1, z' = 3$ , $\theta_M = 0, \psi_M = 0, \nu_{\max} = 15, N = 27$ .....	64
<b>Figure 6.17</b>	Normalized received power $P'$ versus normalized time $t'$ for $z' = 0.5, 0.7, 1, 1.5, 2, 3$ and $w' = 1, \theta_M = 0, \psi_M = 0, \nu_{\max} = 15, N = 27$ , (a) $\rho' = 0$ , (b) $\rho' = 1$ , (c) $\rho' = 2$ , (d) $\rho' = 3$ . .....	65
<b>Figure 6.18</b>	Normalized received power $P'$ versus normalized time $t'$ for $z' = 1, 3, 5, 10$ and $w' = 1, \rho' = 0$ , $\theta_M = 4.83^\circ, \psi_M = 0, \nu_{\max} = 15, N = 27$ .....	66
<b>Figure 6.19</b>	Normalized received power $P'$ versus normalized time $t'$ for (a) $w' = 2$ , (b) $w' = 3$ , (c) $w' = 5$ , (d) $w' = 7$ with $\rho' = 0, 1, 5, 10$ and for $z' = 1, \theta_M = 4.83^\circ, \psi_M = 0, \nu_{\max} = 15, N = 27$ .....	67
<b>Figure 6.20</b>	Normalized received power $P'_d$ versus normalized time $t'$ for collimated beam wave with beamwidths $w' = 0.5, 1, 2, 3, 5, 7$ and for a plane wave ( $w' \rightarrow \infty$ ), $\rho' = 0, z' = 1$ , $\theta_M = 4.83^\circ, \nu_{\max} = 15$ ; $N = 31$ for the plane wave case and $N = 27$ for collimated beam waves....	68
<b>Figure 6.21</b>	Normalized received power $P'$ versus normalized time $t'$ for collimated beam waves with beamwidths $w' = 0.5, 1, 2, 3, 5, 7$ and for a plane wave ( $w' \rightarrow \infty$ ), $\rho' = 0, z' = 1$ , $\theta_M = 62^\circ, \nu_{\max} = 15, N = 31$ for the plane wave case and $N = 27$ for collimated beam waves. ....	69
<b>Figure 6.22</b>	Normalized received power $P'$ versus normalized time $t'$ for collimated beam waves with beamwidths $w' = 0.5, 1, 2, 3, 5, 7$ and for a plane wave ( $w' \rightarrow \infty$ ), $\rho' = 0, z' = 1$ , (a) $\theta_M = 87^\circ$ , (b) $\theta_M = 118^\circ$ , (c) $\theta_M = 150^\circ$ , (d) $\theta_M = 175^\circ$ , $\nu_{\max} = 15, N = 31$ for the plane wave case and $N = 27$ for collimated beam waves.....	70
<b>Figure 6.23</b>	Normalized received power $P'$ versus normalized time $t'$ for different values of $\theta_M$ and for (a) $z' = 1$ , (b) $z' = 3$ , (c) $z' = 5$ , and (d) $z' = 10$ with $w' = 1, \rho' = 0, \nu_{\max} = 15, N = 27$ . ....	71
<b>Figure 6.24</b>	Diffuse Intensity $I_{d,0}$ vs $\theta$ for $\rho' = 0, 1, 2, 2.5, 3$ at (a) $z' = 1$ and (b) $z' = 5$ with $w' = 1$ , $\psi = 0, \pi$ and $N = 31$ . ....	72
<b>Figure 6.25</b>	Diffuse Intensity $I_{d,0}$ vs $\theta$ for $\rho' = 0, 1, 2, 2.5, 3$ at (a) $z' = 1$ and (b) $z' = 5$ with $w' = 1$ , $\psi = -\pi/2, \pi/2$ and $N = 31$ .....	73
<b>Figure 6.26</b>	Diffuse Intensity $I_{d,0}$ vs normalized penetration depth $z'$ for the collimated beam case using the rigorous and approximate solutions for $\rho' = 0$ and $\theta = 0^\circ$ for (a) $0 \leq z' \leq 10$ and (b) $0 \leq z' \leq 100$ with $w' = 1, \psi = 0$ and $N = 31$ . Note that the values of $\beta$ do not apply in this case. ....	74
<b>Figure 6.27</b>	Diffuse Intensity $I_{d,0}$ vs normalized penetration depth $z'$ for the collimated beam case using the rigorous and approximate solutions for $\rho' = 0$ and $\theta = 30^\circ$ for (a) $0 \leq z' \leq 10$ and (b) $0 \leq z' \leq 100$ with $w' = 1, \psi = 0$ and $N = 31$ . Note that the values of $\beta$ are chosen to optimize the composite solution in this case. ....	75
<b>Figure 6.28</b>	Diffuse Intensity $I_{d,0}$ vs normalized penetration depth $z'$ for the collimated beam case using the rigorous and approximate solutions for $\rho' = 0$ and $\theta = 30^\circ$ for (a) $0 \leq z' \leq 10$ and (b) $0 \leq z' \leq 100$ with $w' = 1, \psi = 0$ and $N = 31$ . Note that the values of $\beta$ are chosen to optimize the composite solution for $\rho' = 2$ and $\theta = 0^\circ$ in Figure 6.34.....	76
<b>Figure 6.29</b>	Diffuse Intensity $I_{d,0}$ vs normalized penetration depth $z'$ for the collimated beam case using the rigorous and approximate solutions for $\rho' = 1$ and $\theta = 0^\circ$ for (a) $0 \leq z' \leq 10$ and (b)	



	$0 \leq z' \leq 100$ with $w'=1$ , $\psi=0$ and $N=31$ . Note that the values of $\beta$ are chosen to optimize the composite solution for $\rho'=0$ and $\theta=30^\circ$ in Figure 6.27. ....	77
<b>Figure 6.30</b>	Diffuse Intensity $I_{d,0}$ vs normalized penetration depth $z'$ for the collimated beam case using the rigorous and approximate solutions for $\rho'=1$ and $\theta=0^\circ$ for (a) $0 \leq z' \leq 10$ and (b) $0 \leq z' \leq 100$ with $w'=1$ , $\psi=0$ and $N=31$ . Note that the values of $\beta$ are chosen to optimize the composite solution for $\rho'=2$ and $\theta=0^\circ$ in Figure 6.34.....	78
<b>Figure 6.31</b>	Diffuse Intensity $I_{d,0}$ vs normalized penetration depth $z'$ for the collimated beam case using the rigorous and approximate solutions for $\rho'=1$ and $\theta=30^\circ$ for (a) $0 \leq z' \leq 10$ and (b) $0 \leq z' \leq 100$ with $w'=1$ , $\psi=0$ and $N=31$ . Note that the values of $\beta$ are chosen to optimize the composite solution for $\rho'=0$ and $\theta=30^\circ$ in Figure 6.27. ....	79
<b>Figure 6.32</b>	Diffuse Intensity $I_{d,0}$ vs normalized penetration depth $z'$ for the collimated beam case using the rigorous and approximate solutions for $\rho'=1$ and $\theta=30^\circ$ for (a) $0 \leq z' \leq 10$ and (b) $0 \leq z' \leq 100$ with $w'=1$ , $\psi=0$ and $N=31$ . Note that the values of $\beta$ are chosen to optimize the composite solution for $\rho'=2$ and $\theta=0^\circ$ in Figure 6.34.....	80
<b>Figure 6.33</b>	Diffuse Intensity $I_{d,0}$ vs normalized penetration depth $z'$ for the collimated beam case using the rigorous and approximate solutions for $\rho'=2$ and $\theta=0^\circ$ for (a) $0 \leq z' \leq 10$ and (b) $0 \leq z' \leq 100$ with $w'=1$ , $\psi=0$ and $N=31$ . Note that the values of $\beta$ are chosen to optimize the composite solution for $\rho'=0$ and $\theta=30^\circ$ in Figure 6.27. ....	81
<b>Figure 6.34</b>	Diffuse Intensity $I_{d,0}$ vs normalized penetration depth $z'$ for the collimated beam case using the rigorous and approximate solutions for $\rho'=2$ and $\theta=0^\circ$ for (a) $0 \leq z' \leq 10$ and (b) $0 \leq z' \leq 100$ with $w'=1$ , $\psi=0$ and $N=31$ . Note that the values of $\beta$ are chosen to optimize the composite solution in this case. ....	82
<b>Figure 6.35</b>	Diffuse Intensity $I_{d,0}$ vs normalized penetration depth $z'$ for the collimated beam case using the rigorous and approximate solutions for $\rho'=2$ and $\theta=30^\circ$ for (a) $0 \leq z' \leq 10$ and (b) $0 \leq z' \leq 100$ with $w'=1$ , $\psi=0$ and $N=31$ . Note that the values of $\beta$ are chosen to optimize the composite solution for $\rho'=0$ and $\theta=30^\circ$ in Figure 6.27. ....	83
<b>Figure 6.36</b>	Diffuse Intensity $I_{d,0}$ vs normalized penetration depth $z'$ for the collimated beam case using the rigorous and approximate solutions for $\rho'=2$ and $\theta=30^\circ$ for (a) $0 \leq z' \leq 10$ and (b) $0 \leq z' \leq 100$ with $w'=1$ , $\psi=0$ and $N=31$ . Note that the values of $\beta$ are chosen to optimize the composite solution for $\rho'=2$ and $\theta=0^\circ$ in Figure 6.34.....	84



## 1. INTRODUCTION

For line-of-sight communication, cellular communication in particular, current interest centers on radio-link performance, and how it is affected by wave attenuation, fading and co-channel interference. When vegetation, such as a forest, lies along the path of a radio-link, the radio performance is affected by strong multiscattering effects.

There are two methods that are usually used to study multiscattering effects in random media<sup>1</sup>, namely, analytical theory and transport theory [1]. Analytical theory is a very rigorous mathematical approach based on Maxwell's Equations. It is very complex and obtaining solutions often requires introducing strong simplifications which limit the solutions obtained to restricted parameter ranges. In contrast, radiative transfer theory deals with the transfer of energy through the multiscattering medium. In this theory, the basic equation that is solved is the equation of radiative transfer or transport equation. The radiative transfer theory developed heuristically from the conservation of energy principle in radiation space. The transport equation is equivalent to Boltzmann's equation found in the kinetic theory of gases and in neutron transport theory and is less rigorous than the analytical theory. However, transport theory has been very successfully applied in the study of many radiation problems, such as optical propagation through the atmosphere, remote sensing and radiation from stars.

In previous work, continuous wave (CW) millimeter wave and plane wave pulse propagation in vegetation were studied using the scalar transport theory [2-6]. In these studies, interest focused on the determination of the range and directional dependency of the received power as well as on pulse broadening and distortion. The scalar transport equation is capable of specifying the total energy density of radiation in two orthogonal polarizations, but not polarization or depolarization effects (see [4] for experimental justification of their neglect in these studies for millimeter waves in vegetation). In the earlier developed theory of a plane wave incident upon the forest half-space, it was shown that the range dependence in the forest (treated as a random medium) is not simply an exponential decrease at constant attenuation rate. What actually occurs for the received power is a high attenuation rate at short distances into the medium that evolves into a much lower attenuation rate at large distances. The theory explains this in terms of the interaction between the coherent and incoherent field components. The coherent component, dominating at

---

<sup>1</sup> In this study, a forest half-space is modeled as a random medium.

short distances, is highly attenuated (by absorption and scattering ) while the incoherent component, which is generated by the scattering of the coherent component, does not lose power by further (multiple) scattering - it scatters into itself - and thus dominates at large distances into the forest, decreasing at a much reduced attenuation rate. In the transition region between the high and low attenuation regimes, significant beam broadening and pulse broadening occurs.

In this study, the scalar time-dependent equation of radiative transfer is used to develop a theory for the propagation and scattering of narrow band<sup>1</sup> pulsed beam waves of finite cross-section in a medium that is characterized by many random discrete scatterers (vegetation) which scatter energy strongly in the forward scattering direction. Applications include the scattering of millimeter-waves in vegetation and the scattering of optical beams in the atmosphere. Strong forward scattering occurs at millimeter and optical frequencies since all scatter objects in a forest or in the atmosphere are large compared to wavelength. Again of interest are the range and directional dependency of received power, pulse broadening and distortion, in addition to the effect of a finite beamwidth when the incident field is not a plane wave. This case differs basically from the plane wave case in that scattering out of the beam occurs (while in the plane wave case ,any multiscattered wave trains will always remain within the infinitely wide beam).

---

<sup>1</sup> Narrow band refers to the relatively small frequency band about the carrier frequency, which permits the assumption that media parameters are independent of frequency.



## 2. FORMULATION

In this study, vegetation (a forest) is modeled as a statistically homogeneous half-space of randomly distributed particles that scatter and absorb electromagnetic energy. A periodic sequence of Gaussian pulses is taken to be incident from free space onto the planar boundary of the forest. The incident pulse train is assumed to be either (1) a cylindrically collimated or (2) a spherically diverging beam wave (see Figure 2.1).

Chang and Ishimaru [7] used scalar transport theory to study the scattering of a monochromatic collimated beam-wave in a random medium. Their approach, however, is computational intensive, and does not provide numerical data for off-axis beam scattering<sup>1</sup>. In the method presented here – which also involves using the scalar transport equation in cylindrical coordinates – a more analytical development is achieved, which permits numerical data to be obtained for off-axis beam scattering in the forest.

### 2.1 Incident Gaussian Beam Wave Pulse Train

For the cylindrically collimated case, a beam wave pulse train is assumed to be incident from the air region ( $z < 0$ ) onto the planar boundary of the random scattering medium (a forest), which occupies the half-space region  $z \geq 0$  (see Figures 2.1 and 2.2). At the origin, the magnitude of the instantaneous Poynting vector of the incident beam wave that flows in the  $+z$  direction is assumed to be given by  $S(t) = 2S_{ave}f(t)\cos^2(\omega_c t)$ ;  $f(t)$  is a positive, even function of time  $t$  that is periodic with period  $T$ , i.e.,  $f(t+T) = f(t)$ , and normalized such that

$$\frac{1}{T} \int_{-T/2}^{T/2} f(t) dt = 1 \quad (2.1)$$

$S_{ave}$  is the magnitude of the time average incident Poynting vector assuming  $T \gg T_c = 2\pi / \omega_c$ , where  $\omega_c$  is the carrier frequency.

For Gaussian incident pulses,  $f(t)$  takes the form

$$f(t) = \frac{\alpha_0}{\sqrt{\pi}} e^{-(\alpha_0 t/T)^2}, \quad -\frac{T}{2} \leq t \leq \frac{T}{2} \quad (2.2)$$

$\alpha_0 \equiv \text{const.}$

<sup>1</sup> Limited off-axis data, however, is available in [8].

Since the incident beam wave pulses are even, this periodic function of time can be represented by an even Fourier series at  $z = 0$  :

$$f(t) = \frac{b_0}{2} + \sum_{v=1}^{\infty} b_v \cos(v\omega t) = \text{Re} \left\{ \sum_{v=0}^{\infty} f_v e^{i v \omega t} \right\} \quad (2.3)$$

where

$$\omega = \frac{2\pi}{T}, \quad b_v = \frac{2}{T} \int_{-T/2}^{T/2} f(t) \cos(v\omega t) dt \quad (2.3a)$$

Hence, for the Gaussian pulses in (2.2),

$$f_v = \frac{\varepsilon_v b_v}{2} = \varepsilon_v e^{-(\pi v / \alpha_o)^2}, \quad \varepsilon_v = \begin{cases} 1, & v = 0 \\ 2, & v \neq 0 \end{cases} \quad (2.4)$$

$\alpha_o$  has to be chosen properly to ensure that the Gaussian function in (2.2) approaches zero as  $t \rightarrow \pm T/2$  allowing the limit of the integration in (2.3a) to be replaced by  $\pm \infty$ .

The specific intensity  $I_{inc}$  (power per unit area and per unit solid angle) of an incident collimated beam wave pulse train, that travels through air at the speed of light "c" in the positive z direction, is assumed to have a  $\rho$ -dependent Gaussian amplitude with beamwidth  $w$  and to carry power density  $S_{ave} = P_{ave} / (\pi w^2)$ , where  $P_{ave}$  is the average transmitted power. Thus, this incident intensity is given by

$$I_{inc} = \frac{P_{ave}}{\pi w^2} e^{-(\rho/w)^2} f\left(t - \frac{z}{c}\right) \frac{\delta(\theta)}{2\pi \sin \theta}, \quad z \leq 0 \quad (2.5)$$

with

$$f(t - z/c) = \text{Re} \left\{ \sum_{v=0}^{\infty} f_v e^{i v \omega (t - z/c)} \right\} \quad (2.5a)$$

and  $f_v$  given by (2.4) for the Gaussian pulses (2.2). In (2.5),  $\delta(\theta)$  is the Dirac delta function and  $\theta$  is defined as the scatter angle measured positive from the positive direction of the z-axis (see Figure 2.2).

For the diverging spherical case, the specific intensity of an incident spherical beam wave pulse train in air is given by

$$I_{inc} = \frac{P_{ave} D(\theta_0)}{4\pi R^2} f\left(t - \frac{R}{c}\right) \frac{\delta(\theta - \theta_0) \delta(\psi)}{\sin \theta} \quad z \leq 0 \quad (2.6)$$



with time-periodic pulse train  $f(t - R/c)$  having pulse repetition rate (frequency)  $1/T$  and represented by the Fourier series expansion

$$f(t - \frac{R}{c}) = \text{Re} \left\{ \sum_{v=0}^{\infty} f_v e^{i v \omega (t - R/c)} \right\}, \quad (2.6a)$$

with

$$R = [\rho^2 + (z - z_0)^2]^{1/2}, \quad \cos \theta_0 = (z - z_0) / R, \quad \psi = \phi - \phi_x \quad (2.6b)$$

$D(\theta_0)$  is the directive gain of a transmitting antenna located external to the forest in free space on the  $z$ -axis at  $z = z_0 < 0$ ;  $P_{ave}$  is the average radiated power. Spherical coordinate variables  $(R, \theta_0)$  are defined in Figure 2.1b; the cylindrical angles  $(\phi, \phi_x)$  and the rotating azimuthal coordinate angle  $\psi \equiv \phi - \phi_x$  are defined in Figure 2.2.

## 2.2 Phase Function

In transport theory, the random scatter medium is characterized by an absorption cross-section per unit volume  $\sigma_a$ , the scattering cross-section per unit volume  $\sigma_s$  and a power scatter or phase function  $p(\hat{s}, \hat{s}')$ . The phase function depends on both the incident power unit vector direction  $\hat{s}'$  or, equivalently, the in-scatter angles  $(\theta', \phi')$  and the scatter power unit vector direction  $\hat{s}$  or, equivalently, the out-scatter angles  $(\theta, \phi)$  for each scatter event (see Figure 2.2).

Since scattering surfaces in a forest have essentially random orientations, it is reasonable to assume that a forest scatters energy symmetrically about the direction of the incident radiation, i.e., that the scattering which occurs at each point in a forest can be characterized by a scatter function that depends on the angle  $\gamma$  between  $\hat{s}'$  and  $\hat{s}$ , where  $\gamma = \cos^{-1}(\hat{s}' \cdot \hat{s})$ , and, therefore, that the phase function can be written as

$$p(\hat{s}, \hat{s}') = p(\hat{s} \cdot \hat{s}') = p(\gamma) \quad (2.7)$$

In addition, since all scatter objects in a forest are large compared to the wavelength at millimeter-wave and optical frequencies, the forest scatters energy strongly in the forward direction but weakly in all other directions. For that reason, the scatter function is assumed to be characterized by a strong narrow lobe superimposed over an isotropic background. This type of scatter function can analytically be expressed as a Gaussian function added to a homogeneous term, i.e.,

$$p(\gamma) = \alpha q(\gamma) + (1 - \alpha) \quad , \quad q(\gamma) = \left( \frac{2}{\Delta\gamma_s} \right)^2 e^{-(\gamma/\Delta\gamma_s)^2} \quad , \quad \Delta\gamma_s \ll \pi \quad , \quad (2.8)$$

which is normalized such that

$$\iint_{4\pi} p(\gamma) d\Omega = 4\pi \quad (2.8a)$$

$d\Omega$  is the differential solid angle about the scatter angle  $\hat{s}$ ,  $\Delta\gamma_s$  denotes the width of the forward lobe in the scatter pattern and  $\alpha$  is the ratio of the forward scattered power to the total scattered power. The scatter function (2.8) was justified in [2] by reference to the theoretical and experimental comparison of results in [3, 4], and by the experiments conducted by Ulaby et al. in [9].

Therefore, in transport theory, according to the above discussion and taking the scatter function to be specified by (2.8), the random scatter medium, assumed here to be statistically homogeneous, is characterized by four spatially constant parameters, namely,  $\sigma_a$ ,  $\sigma_s$ ,  $\Delta\gamma_s$  and  $\alpha$ . These four parameters are understood to be "global" parameters in that they remain valid at all points in the random medium and apply to an average scatter event that occurs at every point in the scatter medium.

### 2.3 The Scalar Time-Dependent Transport Equation in Cylindrical Coordinates

In transport theory, the specific intensity "I" of the field in a random medium is governed by the radiative transfer equation (transport equation). In the normalized cylindrical coordinate system  $(\rho', z', \psi)$  for symmetric scattering about the direction of the incident radiation, the scalar transport equation takes the form [10]:

$$\frac{\partial}{\partial t'} I(\vec{r}', t', \hat{s}) + \hat{s} \cdot \nabla' I(\vec{r}', t', \hat{s}) = -I(\vec{r}', t', \hat{s}) + \frac{W_o}{4\pi} \iint_{4\pi} p(\gamma) I(\vec{r}', t', \hat{s}') d\Omega' \quad (2.9)$$

where

$$\hat{s} \cdot \nabla' \equiv \cos \theta \frac{\partial}{\partial z'} + \sin \theta \cos \psi \frac{\partial}{\partial \rho'} - \frac{1}{\rho'} \sin \theta \sin \psi \frac{\partial}{\partial \psi} \quad (2.9a)$$

$$\hat{s} \cdot \hat{s}' = \cos \gamma = \cos \theta \cos \theta' + \sin \theta \sin \theta' \cos(\psi - \psi') \quad (2.9b)$$

$$\psi = \phi - \phi_s, \quad d\Omega' = \sin \theta' d\theta' d\psi' \quad (2.9c)$$



The normalized space and time variable in (2.9) are given by  $\rho' = \sigma_t \rho$ ,  $z' = \sigma_t z$ ,  $t' = \sigma_t c t$  and  $W_0 = \sigma_s / \sigma_t$ ,  $\sigma_t = \sigma_a + \sigma_s$ . The parameter  $W_0$  is called the albedo and the parameters  $\sigma_a$ ,  $\sigma_s$  and  $\sigma_t$  are the absorption, scatter and extinction cross-sections per unit volume, respectively. Implicit in writing (2.9) is the assumption that all parameters are independent of frequency.

To obtain a unique solution to (2.9), with intensity  $I$  assumed to be time periodic, requires satisfaction of the following two boundary conditions:

$$\begin{aligned} I &= I_{inc} \quad \text{at} \quad z' = 0, \quad 0 \leq \theta \leq \pi/2 \\ I &\rightarrow 0 \quad \text{as} \quad z' \rightarrow \infty \end{aligned} \tag{2.10}$$

### 3. RIGOROUS SOLUTION FOR COLLIMATED BEAM WAVE

As is customary [1], the specific intensity is separated into two components, namely, the reduced incident intensity  $I_{ri}$  and the diffuse intensity  $I_d$  by letting

$$I = I_{ri} + I_d . \quad (3.1)$$

Substituting (3.1) into (2.9) and (2.10) yields the defining equations for  $I_{ri}$  and  $I_d$ , which take the forms

$$\frac{\partial}{\partial t'} I_{ri} + \hat{s} \cdot \nabla' I_{ri} + I_{ri} = 0 , \quad (3.2a)$$

$$\frac{\partial}{\partial t'} I_d + \hat{s} \cdot \nabla' I_d + I_d = \frac{W_o}{4\pi} \iint_{4\pi} p(\gamma) I_d d\Omega' + \frac{W_o}{4\pi} \iint_{4\pi} p(\gamma) I_{ri} d\Omega' , \quad (3.2b)$$

with boundary conditions

$$\begin{aligned} I_{ri} &= I_{inc} , \quad I_d = 0 & \text{at} \quad z' = 0, \quad 0 \leq \theta \leq \frac{\pi}{2} . \\ I_{ri} &\rightarrow 0 & \text{as} \quad z' \rightarrow \infty \end{aligned} \quad (3.2c)$$

where  $\hat{s} \cdot \nabla'$  is defined in (2.9a).

To solve (3.2), Fourier series representations are introduced for the time dependence of the intensities:

$$I_j(\rho', z', t', \theta, \psi) = \text{Re} \left\{ \sum_{\nu=0}^{\infty} \tilde{I}_{j,\nu}(\rho', z', \theta, \psi) e^{i\nu\omega' t'} \right\} \quad j = inc, ri, d \quad (3.5)$$

where  $T' = \sigma_t c T$ ,  $\omega' = 2\pi/T'$  and normalized angular frequency  $\omega' = \omega/(c\sigma_t)$ . Note that in the cylindrical case, both  $I_{inc,\nu}$  and, therefore,  $I_{ri,\nu}$  depend only on the three variables  $\rho', z', \theta$ , not four variables as written in (3.5). Observe also that although the specific intensity (power quantity) is always positive, the individual Fourier constituents  $I_{j,\nu}$  may be negative and thus cannot physically represent power.

Substituting (3.5) into (3.2) yields for  $z' > 0$

$$i\nu\omega' \tilde{I}_{ri,\nu} + \hat{s} \cdot \nabla' \tilde{I}_{ri,\nu} + \tilde{I}_{ri,\nu} = 0 \quad (3.6a)$$

$$i\nu\omega' \tilde{I}_{d,\nu} + \hat{s} \cdot \nabla' \tilde{I}_{d,\nu} + \tilde{I}_{d,\nu} = \frac{W_o}{4\pi} \iint_{4\pi} p(\gamma) \tilde{I}_{d,\nu} \sin \theta' d\theta' d\psi' + \frac{W_o}{4\pi} \iint_{4\pi} p(\gamma) \tilde{I}_{ri,\nu} \sin \theta' d\theta' d\psi' \quad (3.6b)$$



with boundary conditions

$$\begin{aligned}\tilde{I}_{ri,v} &= \tilde{I}_{inc,v} \quad , \quad \tilde{I}_{d,v} = 0 \quad \text{at} \quad z' = 0 \quad , \quad 0 \leq \theta \leq \frac{\pi}{2} \\ \tilde{I}_{ri,v} &\rightarrow 0 \quad , \quad \tilde{I}_{d,v} \rightarrow 0 \quad \text{as} \quad z' \rightarrow \infty\end{aligned}\quad (3.6c)$$

where  $v=0,1,2,\dots$

A comparison of (2.5) expressed in normalized variables with (3.5) gives

$$\tilde{I}_{inc,v} = \sigma_t^2 f_v \frac{P_{ave}}{\pi w'^2} e^{-(\rho'/w')^2} \frac{\delta(\theta)}{2\pi \sin \theta} e^{-iv\omega'z'/\cos \theta} \quad (3.7)$$

where  $\delta(\theta)$  is the Dirac delta function and  $w' = \sigma_t w$  is the normalized beamwidth; note that in (3.7),

$\cos \theta = 1$  because  $\theta = 0$  due to the Dirac delta function.

The first boundary condition in (3.6c) together with (3.7) and the definition of  $\tilde{I}_{ri,v}$  in (3.5) dictate that  $\tilde{I}_{ri,v}(\rho', z', \theta) \propto \delta(\theta)/[2\pi \sin \theta]$ . It then follows that

$$\begin{aligned}\hat{s} \cdot \nabla' \tilde{I}_{ri,v} &\equiv \cos \theta \frac{\partial}{\partial z'} \tilde{I}_{ri,v} + \sin \theta \cos \psi \frac{\partial}{\partial \rho'} \tilde{I}_{ri,v} - \frac{1}{\rho'} \sin \theta \sin \psi \frac{\partial}{\partial \psi} \tilde{I}_{ri,v} \\ &= \cos \theta \frac{\partial}{\partial z'} \tilde{I}_{ri,v}\end{aligned}\quad (3.8)$$

and (3.6a) reduces to

$$iv\omega' \tilde{I}_{ri,v} + \cos \theta \frac{\partial}{\partial z'} \tilde{I}_{ri,v} + \tilde{I}_{ri,v} = 0 \quad (3.9)$$

(3.9) is solved by direct integration and use of boundary conditions in (3.6c) to give for  $z' \geq 0$

$$\tilde{I}_{ri,v} = \sigma_t^2 f_v \frac{P_{ave}}{\pi w'^2} e^{-(\rho'/w')^2} e^{-(1+iv\omega')z'} \frac{\delta(\theta)}{2\pi \sin \theta} \quad (3.10)$$

where  $P_{ave}$  is time-average power,  $\rho' = \sigma_t \rho$  and  $z' = \sigma_t z$ ; the un-normalized coordinate variables  $(\rho, \theta)$

are depicted in Figure 2.2.

Let

$$\tilde{I}_{j,v}(\rho', z', \theta, \psi) = I_{j,v}(\rho', z', \theta, \psi) e^{-iv\omega'z'} \quad , \quad j = inc, ri, d \quad (3.11)$$

Substitution of the reduced incident intensity from (3.10) into (3.6b,c) and using (3.11) gives for  $z' > 0$

$$[1 + i\nu\omega'(1 - \cos\theta)]I_{d,\nu} + [\sin\theta \cos\psi \frac{\partial}{\partial\rho'} - \frac{1}{\rho'} \sin\theta \sin\psi \frac{\partial}{\partial\psi} + \cos\theta \frac{\partial}{\partial z'}]I_{d,\nu} \\ = \frac{W_o}{4\pi} \iint_{4\pi} [P(\gamma)I_{d,\nu}] \sin\theta' d\theta' d\psi' + \sigma_t^2 \frac{W_o}{4\pi} f_\nu P(\theta) \frac{P_{ave}}{\pi w'^2} e^{-(\rho'/w')^2} e^{-z'} \quad (3.12)$$

with boundary conditions

$$I_{d,\nu} = 0 \quad \text{at} \quad z' = 0 \quad , \quad 0 \leq \theta \leq \frac{\pi}{2} \\ I_{d,\nu} \rightarrow 0 \quad \text{as} \quad z' \rightarrow \infty \quad (3.12a)$$

where  $\nu = 0, 1, 2, \dots$

To solve (3.12),  $I_{d,\nu}$  is represented in terms of the Fourier-Hankel transform

$$I_{d,\nu}(\rho', z', \theta, \psi) = \sum_{m=0}^{\infty} \int_{k'=0}^{\infty} A_m^\nu(k', z', \theta) [J_m(k'\rho') \cos(m\psi)] k' dk' \quad (3.13a)$$

with inverse transform

$$A_m^\nu(k', z', \theta) = \int_{\psi=0}^{2\pi} \int_{\rho=0}^{\infty} I_{d,\nu}(\rho', z', \theta, \psi) [J_m(k'\rho') \cos(m\psi)] \rho' d\rho' d\psi \quad (3.13b)$$

The representation in (3.13) for  $I_{d,\nu}$  is an expansion in terms of basis functions  $\cos(m\psi)J_m(k'\rho')$  which are complete and obey well-known orthogonality properties. The  $\theta$ -dependent coefficients  $A_m^\nu(k'; z', \theta)$  are further expanded in terms of Associate Legendre functions

$$A_m^\nu(k', z', \theta) = \sum_{l=m}^{\infty} A_{m,l}^\nu(k', z') P_l^m(\cos\theta) = \sum_{l=m}^{\infty} (2l+1) \bar{A}_{m,l}^\nu(k', z') P_l^m(\cos\theta) \quad (3.14)$$

so that (3.13a) becomes

$$I_{d,\nu}(\rho', z', \theta, \psi) = \sum_{m=0}^{\infty} \int_{k'=0}^{\infty} \sum_{l=m}^{\infty} (2l+1) \bar{A}_{m,l}^\nu(k', z') P_l^m(\cos\theta) J_m(k'\rho') \cos(m\psi) k' dk' \quad (3.15)$$

Since scattering is assumed to be symmetric about the direction of the incident wave, the phase function is a function of  $\gamma$  only and is conveniently represented as a series of Legendre polynomials  $P_l$  [1]

$$P(\gamma) = \sum_{l=0}^{\infty} (2l+1) g_l P_l(\cos\gamma) \quad (3.16)$$



The Legendre polynomials are then expressed in terms of Associated Legendre functions via the expansion [1]

$$\begin{aligned} P_l(\cos \gamma) &= P_l(\mu)P_l(\mu') + 2 \sum_{n=1}^l \frac{(l-n)!}{(l+n)!} P_l^n(\mu)P_l^n(\mu') \cos(n(\psi - \psi')) \\ &= \sum_{n=0}^l \frac{2(l-n)!}{\varepsilon_n(l+n)!} P_l^n(\mu)P_l^n(\mu') \cos(n(\psi - \psi')) \end{aligned} \quad (3.17)$$

$$\text{with } \mu = \cos \theta \quad \text{and} \quad \varepsilon_n = \begin{cases} 2, & n=0 \\ 1, & n=1, 2, \dots \end{cases} \quad (3.17a)$$

to give

$$p(\gamma) = \sum_{l=0}^{\infty} \sum_{n=0}^l (2l+1) \frac{2(l-n)!}{\varepsilon_n(l+n)!} g_l P_l^n(\mu)P_l^n(\mu') \cos n(\psi - \psi') \quad (3.18)$$

For the scatter function (2.8),

$$g_l = \frac{2\alpha}{\Delta\gamma_s^2} \int_{\gamma=0}^{\pi} e^{-(\gamma/\Delta\gamma_s)^2} P_l(\cos \gamma) \sin \gamma d\gamma + (1-\alpha)\delta_{0l}, \quad \delta_{0l} = \begin{cases} 1, & \text{for } l=0 \\ 0, & \text{for } l \neq 0 \end{cases} \quad (3.19)$$

Substituting (3.15), (3.18) and (3.19) into (3.12), using orthogonal properties, recursion relations and various identities of the functions  $J_m(k'\rho')$ ,  $\cos(m\psi)$  and  $P_l^m(\cos \theta)$ , and truncating at  $(m=N, l=N)$  yields the following inhomogeneous system of linear first order differential equations:

$$\begin{aligned} (l-m) \left[ \frac{\partial}{\partial z'} \bar{A}_{m,l-1}^\nu - i\nu\omega' \bar{A}_{m,l-1}^\nu \right] + (l+m+1) \left[ \frac{\partial}{\partial z'} \bar{A}_{m,l+1}^\nu - i\nu\omega' \bar{A}_{m,l+1}^\nu \right] + (2l+1) [1 - W_0 g_l + i\nu\omega'] \bar{A}_{m,l}^\nu \\ + \frac{k'}{2} [(l-m-1)(l-m) \bar{A}_{m+1,l-1}^\nu - (l+m+1)(l+m+2) \bar{A}_{m+1,l+1}^\nu] + \frac{k'}{2} \hat{\varepsilon}_{m-1} [\bar{A}_{m-1,l-1}^\nu - \bar{A}_{m-1,l+1}^\nu] \\ = \frac{W_0}{8\pi^2} P_{ave} f_\nu e^{-(k'w'/2)^2} (2l+1) g_l \delta_{m0} e^{-z'} \end{aligned} \quad (3.20)$$

$$\text{for } m = 0, 1, 2, \dots, N \quad l = m, m+1, \dots, N \quad 0 \leq k' < \infty$$

with

$$\hat{\varepsilon}_{m-1} = \begin{cases} 2, & m=1 \\ 1, & m=2, 3, \dots \\ 0, & m=0 \end{cases} \quad (3.20a)$$

Introducing the normalization

$$\bar{A}_{m,l}^\nu(k', z') = b_{m,l}^\nu(k', z') \frac{Q^\nu(k', w')}{U_l^m V^m} \quad (3.21)$$

where

$$Q^\nu(k', w') = \sqrt{\pi} \frac{W_0}{4\pi^2} P_{ave} f_\nu e^{-(k'w'/2)^2} \quad U_l^m = \sqrt{\frac{2}{2l+1} \frac{(l+m)!}{(l-m)!}} \quad V^m = \sqrt{\pi \varepsilon_m}$$

$$\varepsilon_m = \begin{cases} 2, & m=0 \\ 1, & m=1, 2, \dots \end{cases} \quad (3.21a)$$

allows (3.15) to be rewritten as

$$I_{d,\nu}(\rho', z', \theta, \psi) = \sum_{m=0}^{\infty} \int_{k'=0}^{\infty} \sum_{l=m}^{\infty} (2l+1) Q^\nu(k', w') b_{m,l}^\nu(k', z') \frac{P_l^m(\cos \theta) \cos(m\psi)}{U_l^m V^m} J_m(k' \rho') k' dk' \quad (3.22)$$

and simplifies (3.20), which becomes

$$\alpha_1 \left[ \frac{\partial}{\partial z'} b_{m,l-1}^\nu - i\omega' b_{m,l-1}^\nu \right] + \alpha_2 \left[ \frac{\partial}{\partial z'} b_{m,l+1}^\nu - i\omega' b_{m,l+1}^\nu \right] + \alpha_3 [1 - W_0 g_l + i\omega'] b_{m,l}^\nu$$

$$+ \frac{k'}{2} \bar{\varepsilon}_m [\alpha_4 b_{m+1,l-1}^\nu - \alpha_5 b_{m+1,l+1}^\nu] + \frac{k'}{2} \delta_m [\alpha_6 b_{m-1,l-1}^\nu - \alpha_7 b_{m-1,l+1}^\nu] = g_l \delta_{m0} e^{-z'}$$

$$m = 0, 1, 2, \dots, N; \quad l = m, m+1, \dots, N; \quad 0 \leq k', z' < \infty$$

with

$$\bar{\varepsilon}_m = \begin{cases} \sqrt{2} & , \quad m=0 \\ 1 & , \quad m=1, 2, 3, \dots, N \end{cases} \quad \delta_m = \begin{cases} 0 & , \quad m=0 \\ \sqrt{2} & , \quad m=1 \\ 1 & , \quad m=2, 3, \dots, N \end{cases}$$

$$\delta_m = \begin{cases} 0 & , \quad m=0 \\ \sqrt{2} & , \quad m=1 \\ 1 & , \quad m=2, 3, \dots, N-1, N \end{cases} \quad \delta_{m0} = \begin{cases} 1 & , \quad m=0 \\ 0 & , \quad m \neq 0 \end{cases} \quad (3.23.a)$$

$$\alpha_1 \equiv \sqrt{\frac{(l-m)(l+m)(2l-1)}{(2l+1)^2}}, \alpha_2 \equiv \sqrt{\frac{(l-m+1)(l+m+1)(2l+3)}{(2l+1)^2}}, \alpha_3 \equiv \sqrt{2l+1},$$

$$\alpha_4 \equiv \sqrt{\frac{(l-m-1)(l-m)(2l-1)}{(2l+1)^2}}, \alpha_5 \equiv \sqrt{\frac{(l+m+1)(l+m+2)(2l+3)}{(2l+1)^2}},$$

$$\alpha_6 \equiv \sqrt{\frac{(l+m)(l+m-1)(2l-1)}{(2l+1)^2}}, \alpha_7 \equiv \sqrt{\frac{(l-m+2)(l-m+1)(2l+3)}{(2l+1)^2}} \quad (3.23.b)$$



### 3.1 Homogeneous Solution

The solution of (3.23) requires determination of both the homogeneous and particular solutions. For the former, the right hand side of (3.23) is set equal to zero and the homogeneous solution is assumed to be of the form

$$b_{m,l}^{\nu,h}(z',k') = G_{m,l}^{\nu}(k')e^{-z'/\sigma}. \quad (3.24)$$

Substitution of (3.24) into (3.23) with the right hand side set to zero yields the homogeneous system of linear equations

$$\alpha_1 G_{m,l-1}^{\nu} + \alpha_2 G_{m,l+1}^{\nu} = \sigma \left\{ -c_{\nu} [\alpha_1 G_{m,l-1}^{\nu} + \alpha_2 G_{m,l+1}^{\nu}] + b_{\nu l} [\alpha_3 G_{m,l}^{\nu}] + \right. \\ \left. \frac{k'}{2} \bar{\varepsilon}_m [\alpha_4 G_{m+1,l-1}^{\nu} - \alpha_5 G_{m+1,l+1}^{\nu}] + \frac{k'}{2} \delta_m [\alpha_6 G_{m-1,l-1}^{\nu} - \alpha_7 G_{m-1,l+1}^{\nu}] \right\} \\ \text{for } m = 0, 1, 2, \dots, N \quad l = m, m+1, \dots, N \quad 0 \leq k' < \infty \quad (3.25)$$

where  $b_{\nu l} = 1 - W_0 g_l + i\nu\omega'$ ,  $c_{\nu} = i\nu\omega'$ ;  $(\bar{\varepsilon}_m, \delta_m)$  and  $\alpha_n, n = 1, 2, \dots, 7$ , are given in (3.23.a,b), respectively. Writing (3.25) in matrix form gives the generalized eigenvalue equation

$$[\mathbf{A}_0] \mathbf{G} = \sigma [\mathbf{C}_0] \mathbf{G} \quad (3.26)$$

where matrices  $[\mathbf{A}_0]$  and  $[\mathbf{C}_0]$  are matrices. The eigenvalues ( $\sigma$ ) and eigenvectors ( $\mathbf{G}$ ) are determined by using the QZ method algorithm in the LAPACK library [11].

### 3.2 Particular Solution

The particular solution to (3.23) is obtained by assuming

$$b_{m,l}^{\nu p}(z',k') = F_{m,l}^{\nu}(k')e^{-z'} \quad (3.27)$$

which, when substituted into (3.23), gives the system of linear equations

$$\alpha_1 [-F_{m,l-1}^{\nu} a_{\nu}] + \alpha_2 [-F_{m,l+1}^{\nu} a_{\nu}] + \alpha_3 b_{\nu l} F_{m,l}^{\nu} \\ + \frac{k'}{2} \bar{\varepsilon}_m [\alpha_4 F_{m+1,l-1}^{\nu} - \alpha_5 F_{m+1,l+1}^{\nu}] + \frac{k'}{2} \delta_m [\alpha_6 F_{m-1,l-1}^{\nu} - \alpha_7 F_{m-1,l+1}^{\nu}] \\ = g_l \delta_{m0} \quad \text{for } m = 0, 1, \dots, N \quad \text{and } l = m, m+1, \dots, N \quad (3.28)$$

where  $a_\nu = 1 + i\nu\omega'$  with  $(\bar{\varepsilon}_m, \delta_m, \delta_{m0}, b_{\nu l}, g_l \text{ and } \alpha_n, n = 1, 2, \dots, 7)$  defined in (3.23a,b). In matrix form (3.28) is written as

$$[\mathbf{B}_0]\mathbf{F} = \mathbf{g} \quad (3.29)$$

where  $[\mathbf{B}_0]$  is a matrix while  $\mathbf{F}$  and  $\mathbf{g}$  are column vectors. The ZGESVX routine from the LAPACK library is used to find the particular solution [11].

The general solution to (3.23) is the superposition of the particular solution and  $N_h = (N+1)^2/4$  allowable homogeneous solutions that obey the condition that  $\text{Re}\{1/\sigma\} > 0$ , which ensure that solutions decay as  $z' \rightarrow \infty$ . Thus, the general solution is obtained as

$$b_{m,l}^\nu(k', z') = b_{m,l}^{\nu p}(k', z') + \sum_{i=1}^{N_h} a_i b_{m,l}^{\nu,i}(k', z') = F_{m,l}^\nu(k') e^{-z'} + \sum_{i=1}^{N_h} a_i G_{m,l}^{\nu,i}(k') e^{-z'/\sigma_i} \quad (3.30)$$

where  $a_i, i = 1, \dots, N_h$ , are arbitrary constants that are determined from the boundary condition at  $z' = 0$ .

Thus, using (3.30) in (3.22) and incorporating the truncations, the diffuse intensity is expressed as

$$I_{d,\nu}(\rho', z', \theta, \psi) = \sum_{m=0}^N \int_{k'=0}^{k'_{\max}} \sum_{l=m}^N \{J_m(k'\rho') k' dk' (2l+1) Q^\nu(k', w') [F_{m,l}^\nu(k') e^{-z'} + \sum_{i=1}^{N_h} a_i G_{m,l}^{\nu,i}(k') e^{-z'/\sigma_i}] \cdot \frac{P_l^m(\cos \theta)}{U_l^m} \frac{\cos(m\psi)}{V^m}\} k' dk' \quad (3.31)$$

### 3.3 Boundary Condition at Entrance to Forest ( $z' = 0$ ) to Find the Coefficients $a_i$

From (3.12a),  $I_{d,\nu}$  must satisfy the boundary condition

$$I_{d,\nu}(\rho', z' = 0, \theta, \psi) = 0 \quad \text{for } z' = 0, 0 \leq \theta \leq \frac{\pi}{2}, 0 \leq \rho' < \infty, 0 \leq \psi \leq 2\pi \quad (3.32)$$

Introducing (3.31) into (3.32) gives

$$I_{d,\nu}(\rho', z' = 0, \theta, \psi) = \int_{k'=0}^{k'_{\max}} I_{d,\nu}(k', z' = 0, \theta, \psi) J_m(k'\rho') k' dk' = 0 \quad (3.33)$$

where

$$I_{d,\nu}(k', z' = 0, \theta, \psi) \equiv \sum_{m=0}^N \sum_{l=m}^N (2l+1) Q^\nu(k', w') b_{m,l}^\nu(k', z') \frac{P_l^m(\cos \theta)}{U_l^m} \frac{\cos(m\psi)}{V^m} \quad (3.33a)$$

with



$$b_{m,l}^{\nu}(k', z') = F_{m',l'}^{\nu} + \sum_{i=1}^{N_h} a_i G_{m',l'}^{\nu,i} \quad (3.33b)$$

Multiplying (3.33) by  $J_m(k''\rho')$ , integrating over  $\rho'$  from zero to infinity, interchanging the order of integration and using the completeness relation

$$\int_{\rho'=0}^{\infty} J_m(k'\rho') J_m(k''\rho') \rho' d\rho' = \delta(k' - k'') / k' \quad (3.34)$$

yields

$$I_{d,\nu}(k', z' = 0, \theta, \psi) = \int_{\rho'=0}^{\infty} I_{d,\nu}(\rho', z' = 0, \theta, \psi) J_m(k'\rho') \rho' d\rho' = 0 \quad (3.35)$$

Thus with (3.33a), the following boundary condition is obtained:

$$I_{d,\nu}(k', z' = 0, \theta, \psi) \equiv \sum_{m=0}^N \sum_{l=m}^N (2l+1) Q^{\nu}(k', w') b_{m,l}^{\nu}(k', z') \frac{P_l^m(\cos \theta)}{U_l^m} \frac{\cos(m\psi)}{V^m} = 0 \quad (3.36)$$

$$\text{for } z' = 0, \quad 0 \leq \theta \leq \frac{\pi}{2}, \quad 0 \leq k' < \infty, \quad 0 \leq \psi \leq 2\pi$$

The boundary condition (3.36) is satisfied by using the normalized spherical harmonic functions as testing functions in the weighted residual method [12]. Hence,

$$\int_{\psi=0}^{2\pi} \int_{\theta=0}^{\pi/2} I_{d,\nu}(k', z' = 0, \theta, \psi) \left[ \frac{P_l^m(\cos \theta)}{U_l^m} \right] \left[ \frac{\cos(m\psi)}{V^m} \right] \sin \theta d\theta d\psi = 0 \quad (3.37)$$

for values of  $(l - m)$  which are odd. Substituting (3.33a,b) into (3.37) yields

$$\begin{aligned} & Q^{\nu}(k', w') \sum_{m'=0}^N \sum_{l'=m'}^N (2l'+1) \left[ F_{m',l'}^{\nu} + \sum_{i=1}^{N_h} a_i G_{m',l'}^{\nu,i} \right] \\ & \underbrace{\int_{\psi=0}^{2\pi} \left[ \frac{\cos(m'\psi)}{V^{m'}} \right] \left[ \frac{\cos(m\psi)}{V^m} \right] d\psi}_{\equiv \delta_{mm'} = \begin{cases} 1, m=m' \\ 0, m \neq m' \end{cases}} \underbrace{\int_{\theta=0}^{\pi/2} \left[ \frac{P_{l'}^{m'}(\cos \theta)}{U_{l'}^{m'}} \right] \left[ \frac{P_l^m(\cos \theta)}{U_l^m} \right] \sin \theta d\theta}_{\equiv \hat{I}_{l,l'}^{m,m'}} = 0 \end{aligned} \quad (3.38)$$

Thus,

$$\sum_{i=1}^{N_h} a_i(k') \left[ \underbrace{\sum_{l'=m}^N (2l'+1) G_{m,l'}^{v,i}(k') \hat{I}_{l,l'}^m}_{\equiv S_{m,l}^{v,i}(k')} \right] = \left[ \underbrace{-\sum_{l'=m}^N (2l'+1) F_{m,l'}^v(k') \hat{I}_{l,l'}^m}_{\equiv T_{m,l}^v(k')} \right]$$

or, equivalently,

$$\sum_{i=1}^{N_h} a_i(k') S_{m,l}^{v,i} = T_{m,l}^v(k') \quad (3.39)$$

where

$$S_{m,l}^{v,i}(k') = \sum_{l'=m}^N (2l'+1) G_{m,l'}^{v,i}(k') \hat{I}_{l,l'}^m \quad T_{m,l}^v(k') = -\sum_{l'=m}^N (2l'+1) F_{m,l'}^v(k') \hat{I}_{l,l'}^m$$

with

$$\hat{I}_{l,l'}^m = \int_{\theta=0}^{\pi/2} \left[ \frac{P_{l'}^m(\cos \theta)}{U_{l'}^m} \right] \left[ \frac{P_l^m(\cos \theta)}{U_l^m} \right] \sin \theta d\theta$$

$$= \begin{cases} \hat{J}_{l,l'}^m & \text{for } m \geq 0 \text{ such that } l-m = \text{odd}, l-l' = \text{odd} \\ \frac{1}{2} & \text{for } m \geq 0 \text{ such that } l-m = \text{odd}, l-l' = 0 \\ 0 & \text{otherwise} \end{cases}$$

$$\hat{J}_{l,l'}^m = \frac{1}{2} (-1)^{(l'+l)/2+m+1/2} \frac{\sqrt{(2l+1)(2l'+1)((l+m)^2 - m^2)}}{(l'-l)(l'+l+1)} \cdot R(l'-m) R(l'+m) R(l+m+1) R(l-m+1)$$

$$R(\chi) \equiv \frac{\sqrt{\chi!}}{2^{\chi/2} \left(\frac{\chi}{2}\right)!}, \quad \chi = \text{even} \quad (3.39a)$$

Assume that a highly directive, lossless antenna of narrow beamwidth and narrow bandwidth is located inside the forest [2]. This receiving antenna is characterized by an effective aperture  $A(\gamma_R)$ , where  $\gamma_R$  is the angle included between the direction of observation  $(\theta_R, \psi_R)$  and the pointing direction of the antenna axis, i.e., the main beam direction  $(\theta_M, \psi_M)$ ; see Figures 2.2 and 2.3. Hence,

### 3.4 Power Received by a Highly Directive Antenna in the Forest

$$\cos \gamma_R = \cos \theta_R \cos \theta_M + \sin \theta_R \sin \theta_M \cos(\psi_R - \psi_M) \quad (3.40)$$

In transport theory, powers add. Thus, the instantaneous power received by the antenna is the sum of the intensity contributions coming from all directions multiplied by the effective aperture of the antenna, i.e.,



$$P^R(z', \rho', t', \theta_M, \psi_M) = \text{Re} \left\{ \sum_{v=0}^{\infty} P_v^R(z', \rho', \theta_M, \psi_M) e^{i v \omega (t' - z')} \right\} \quad (3.41)$$

where

$$P_v^R(z', \rho', \theta_M, \psi_M) = \iint_{4\pi} A_e(\gamma_R) I_v(z', \rho', \theta_R, \psi_R) \sin \theta_R d\theta_R d\psi_R \quad (3.41a)$$

and

$$I_v = I_{d,v} + I_{ri,v} \quad (3.41b)$$

Note that  $\theta = \theta_R$  and  $\psi = \psi_R$ .

For millimeter waves, the carrier frequency is very large and, therefore, the bandwidth of the received signal is narrow. For such a small bandwidth, the effective aperture and gain of the receiving antenna can be taken to be independent of frequency and to be related by the general expression

$$A_e(\gamma_R) = \frac{\lambda_o^2}{4\pi} D(\gamma_R) \quad (3.42)$$

where  $\lambda_o$  is the free space wavelength and  $D(\gamma_R)$  is the directive gain of the antenna at the carrier frequency.

Assume that the directive gain is Gaussian with a narrow beamwidth  $\Delta\gamma_M$  and no sidelobes, i.e.,

$$D(\gamma_R) = \left( \frac{2}{\Delta\gamma_M} \right)^2 e^{-(\gamma_R / \Delta\gamma_M)^2}, \quad \Delta\gamma_M \ll \pi, \quad (3.43)$$

which is normalized such that

$$\iint_{4\pi} D(\gamma_R) \sin \theta_R d\theta_R d\psi_R = 4\pi \quad (3.43a)$$

Using (3.41b), (3.42) and (3.43), the received instantaneous power  $P^R$  in (3.41) is obtained as the sum of diffuse power  $P_d^R$  and reduced incident power  $P_{ri}^R$ . The received diffuse power is obtained as

$$P_d^R(z', \rho', t', \theta_M, \psi_M) = \text{Re} \left\{ \sum_{v=0}^{\infty} P_{d,v}^R(z', \rho', \theta_M, \psi_M) e^{i v \omega (t' - z')} \right\} \quad (3.44)$$

where

$$\begin{aligned}
P_{d,v}^R(z', \rho', \theta_M, \psi_M) &= \iint_{4\pi} A_e(\gamma_R) I_{d,v}(z', \rho', \theta_R, \psi_R) \sin \theta_R d\theta_R d\psi_R \\
&= \frac{\lambda_o^2}{4\pi} \iint_{4\pi} D(\gamma_R) I_{d,v}(z', \rho', \theta_R, \phi_R) \sin \theta_R d\theta_R d\psi_R \\
&\cong \frac{\lambda_o^2}{4\pi} I_{d,v}(z', \rho', \theta_M, \psi_M) \iint_{4\pi} D(\gamma_R) \sin \theta_R d\theta_R d\psi_R \\
&= \lambda_o^2 I_{d,v}(z', \rho', \theta_M, \psi_M) \quad .
\end{aligned} \tag{3.44a}$$

Similarly, the received reduced incident power is obtained as

$$P_{ri}^R(z', \rho', t', \theta_M, \psi_M) = \text{Re} \left\{ \sum_{v=0}^{\infty} P_{ri,v}^R(z', \rho', \theta_M, \psi_M) e^{i v \omega' (t' - z')} \right\} \tag{3.45}$$

where

$$\begin{aligned}
P_{ri,v}^R(z', \rho', \theta_M, \psi_M) &= \iint_{4\pi} A_e(\gamma_R) I_{ri,v}(z', \rho', \theta_R, \phi_R) \sin \theta_R d\theta_R d\psi_R \\
&\approx \frac{\lambda_o^2}{4\pi} \sigma_t^2 \frac{P_{ave}}{\pi w'^2} f_v e^{-(\rho'/w')^2} e^{-z'} \int_0^{2\pi} \int_0^{\pi} D(\gamma_R) \frac{\delta(\theta_R)}{2\pi \sin \theta_R} \sin \theta_R d\theta_R d\psi_R \\
&= \frac{\lambda_o^2}{4\pi} \sigma_t^2 \frac{P_{ave}}{\pi w'^2} f_v e^{-(\rho'/w')^2} e^{-z'} D(\theta_M) \quad .
\end{aligned} \tag{3.45a}$$

The instantaneous received power is normalized to the received time-averaged power at  $z' = 0, \rho' = 0,$

$\theta_M = 0$  and  $\psi_M = 0$ , which is given by

$$\langle P^R(0, 0, t', 0, 0) \rangle \equiv \frac{1}{T'} \int_{-T'/2}^{T'/2} P^R(0, 0, t', 0, 0) dt' = \frac{\lambda_o^2}{4\pi} D(0) \sigma_t^2 \frac{P_{ave}}{\pi w'^2} \tag{3.46}$$

since  $I_{d,v}$  is zero at  $z' = 0$  and using (2.1) and (2.3). Thus, the normalized total instantaneous power is the sum of the reduced incident and the diffuse normalized received powers, namely,

$$P'(z', \rho', t', \theta_M, \psi_M) = \frac{P^R(z', \rho', t', \theta_M, \psi_M)}{\langle P^R(0, 0, t', 0, 0) \rangle} = P'_{ri} + P'_d. \tag{3.47}$$

Using (3.44-3.47), the total normalized instantaneous received power becomes

$$P'(z', \rho', t', \theta_M, \psi_M) = P'_{ri} + P'_d = \text{Re} \left\{ \sum_{v=0}^{\infty} P'_v(z', \rho', \theta_M, \psi_M) e^{i v \omega' (t' - z')} \right\} \tag{3.48}$$

where

$$P'_v(z', \rho', \theta_M, \psi_M) = P'_{ri,v} + P'_{d,v} = \frac{D(\theta_M)}{D(0)} e^{-(\rho'/w')^2} f_v e^{-z'} + \frac{4\pi(\pi w'^2)}{\sigma_t^2 P_{ave} D(0)} I_{d,v}(z', \rho', \theta_M, \psi_M)$$



Observe from (3.48) that

$$P'_{ri} = \sum_{\nu=0}^{\infty} P'_{\nu,ri} = \frac{D(\theta_M)}{D(0)} e^{-(\rho'/w')^2} e^{-z'} \operatorname{Re} \sum_{\nu=0}^{\infty} f_{\nu} e^{i\nu\omega'(t'-z')} = \frac{D(\theta_M)}{D(0)} e^{-(\rho'/w')^2 - z'} f(t' - z') \quad (3.49)$$

This result was expected since the reduced incident power  $P'_{ri}$  is the power of the incident beam wave pulse train which, as it travels through the forest along a straight path, decays exponentially due to absorption and scattering, but maintains its narrow beamwidth. The  $\theta$ -dependence of  $P'_{ri}$  thus reproduces the radiation pattern of the receiving antenna. On the other hand, the diffuse intensity, generated by scattering of the reduced incident intensity and by self-regeneration due to multiscattering, is characterized by a broad beamwidth which is larger than that of the receiving antenna. Hence, the receiving antenna acts to probe the angular distribution of the diffuse intensity  $I_{d,\nu}$  as seen from (3.48). Note that at  $z' = 0$ ,  $\rho' = 0$  and for  $\theta_M = 0$ ,  $P_{ri} = f(t')$ . In numerical results, the summation in (3.48) is truncated at a value  $\nu = \nu_{\max}$  that ensures convergence.

#### 4. RIGOROUS SOLUTION FOR SPHERICAL BEAM WAVE

The important practical case of a spherical wave (radiated by an antenna placed in the air region external to the forest half-space) is assumed to be incident upon the forest. Such an incident beam is given by (2.6) and illustrated in Figure 2.1b. In (2.6), the antenna power pattern or directive gain  $D$  is assumed to be rotationally symmetric so that it depends only on the angle  $\theta_0$ .

Following the development of the rigorous solution for the collimated beam, the specific intensity for the spherical beam is assumed to be the sum (3.1) of the reduced incident intensity, defined by (3.2a), and the diffuse intensity, which is governed by (3.2b), that satisfy the boundary conditions (3.2c).

Introducing the Fourier series representation (3.5) into (3.2) yields the defining equations (3.6) for the transformed intensities  $\tilde{I}_{j,v}(\rho', z', \theta, \psi)$ ,  $j = inc, ri, d$ . Using the expression for the incident spherical beam (2.6) with the Fourier series representation (3.5) gives

$$\tilde{I}_{inc,v} = \sigma_t^2 f_v \frac{P_{inc} D(\theta_0)}{4\pi R'^2} \frac{\delta(\theta - \theta_0) \delta(\psi)}{\sin \theta} e^{-i\nu\omega'(z' - z'_0)/\cos \theta} \quad (4.1)$$

where  $R' = \sigma_t R$ ,  $z'_0 = \sigma_t z_0$  with  $(R, \theta_0)$  defined in (2.6b) and in Figure 2.1b.

Use of (4.1) and boundary conditions in (3.6c) give the reduced incident intensity for the spherical beam for  $z' > 0$  as

$$\tilde{I}_{ri,v} = \sigma_t^2 f_v \frac{P_{ave} D(\theta_0)}{4\pi R'^2} e^{-(1+i\nu\omega')z'/\cos \theta_0} e^{i\nu\omega'z'_0/\cos \theta_0} \frac{\delta(\theta - \theta_0) \delta(\psi)}{\sin \theta_0} \quad (4.2)$$

where  $P_{ave}$  is time-average radiated power and  $z_0 < 0$ . Equation (4.2) can be shown to satisfy (3.6a).

Substitution of the reduced incident intensity from (4.2) into (3.6b,c) and using (3.11) gives for  $z' > 0$

$$\begin{aligned} & [1 + i\nu\omega'(1 - \cos \theta)] I_{d,v} + [\sin \theta \cos \psi \frac{\partial}{\partial \rho'} - \frac{1}{\rho'} \sin \theta \sin \psi \frac{\partial}{\partial \psi} + \cos \theta \frac{\partial}{\partial z'}] I_{d,v} \\ & = \frac{W_o}{4\pi} \iint_{4\pi} [P(\gamma) I_{d,v}] \sin \theta' d\theta' d\psi' + \sigma_t^2 \frac{W_o}{4\pi} f_v P(\gamma_0) \frac{P_{ave} D(\theta_0)}{4\pi R'^2} e^{-z'/\cos \theta_0} \end{aligned} \quad (4.3)$$

with boundary conditions



$$\begin{aligned} I_{d,\nu} &= 0 \quad \text{at} \quad z' = 0 \quad , \quad 0 \leq \theta \leq \frac{\pi}{2} \\ I_{d,\nu} &\rightarrow 0 \quad \text{as} \quad z' \rightarrow \infty \end{aligned} \quad (4.3a)$$

where  $\nu = 0, 1, 2, \dots$

To solve (4.3),  $I_{d,\nu}$  is represented as in (3.22) in terms of the Fourier-Hankel transform and Associate Legendre functions as follows:

$$I_{d,\nu}(\rho', z', \theta, \psi) = \sum_{m=0}^{\infty} \int_{k'=0}^{\infty} \sum_{l=m}^{\infty} (2l+1) Q^{\nu}(k', w') b_{m,l}^{\nu}(k', z') \frac{P_l^m(\cos \theta) \cos(m\psi)}{U_l^m V^m} J_m(k' \rho') k' dk' \quad (4.4)$$

where  $U_l^m$  and  $V^m$  are defined in (3.21a) and

$$Q^{\nu} = \frac{W_0}{4\pi^{3/2}} P_{ave} f_{\nu} \quad (4.4a)$$

Substituting (4.4) into (4.3) using the phase function (3.18) with (3.19) gives the inhomogeneous linear system of equations that needs to be solved

$$\begin{aligned} &\alpha_1 \left[ \frac{\partial}{\partial z'} b_{m,l-1}^{\nu} - i\nu \omega' b_{m,l-1}^{\nu} \right] + \alpha_2 \left[ \frac{\partial}{\partial z'} b_{m,l+1}^{\nu} - i\nu \omega' b_{m,l+1}^{\nu} \right] + \alpha_3 [1 - W_0 g_l + i\nu \omega'] b_{m,l}^{\nu} \\ &+ \frac{k'}{2} \bar{\varepsilon}_m [\alpha_4 b_{m+1,l-1}^{\nu} - \alpha_5 b_{m+1,l+1}^{\nu}] + \frac{k'}{2} \delta_m [\alpha_6 b_{m-1,l-1}^{\nu} - \alpha_7 b_{m-1,l+1}^{\nu}] = \frac{1}{[\varepsilon_m (2l+1)]^{1/2}} g_l P_l^m(k', z') \end{aligned} \quad (4.5)$$

$$m = 0, 1, 2, \dots, N; \quad l = m, m+1, \dots, N; \quad 0 \leq k', z' < \infty$$

with

$$\begin{aligned} \bar{\varepsilon}_m &= \begin{cases} \sqrt{2} & , \quad m = 0 \\ 1 & , \quad m = 1, 2, \dots, N \end{cases} \\ \delta_m &= \begin{cases} 0 & , \quad m = 0 \\ \sqrt{2} & , \quad m = 1 \\ 1 & , \quad m = 2, 3, \dots, N \end{cases} \quad \varepsilon_m = \begin{cases} 2 & , \quad m = 0 \\ 1 & , \quad m = 1, 2, \dots, N \end{cases} \\ \delta_m &= \begin{cases} 0 & , \quad m = 0 \\ \sqrt{2} & , \quad m = 1 \\ 1 & , \quad m = 2, 3, \dots, N-1, N \end{cases} \quad \delta_{m0} = \begin{cases} 1 & , \quad m = 0 \\ 0 & , \quad m \neq 0 \end{cases} \end{aligned} \quad (4.5a)$$

$$\begin{aligned}
\alpha_1 &\equiv \sqrt{\frac{(l-m)(l+m)(2l-1)}{(2l+1)^2}}, \alpha_2 \equiv \sqrt{\frac{(l-m+1)(l+m+1)(2l+3)}{(2l+1)^2}}, \alpha_3 \equiv \sqrt{2l+1}, \\
\alpha_4 &\equiv \sqrt{\frac{(l-m-1)(l-m)(2l-1)}{(2l+1)^2}}, \alpha_5 \equiv \sqrt{\frac{(l+m+1)(l+m+2)(2l+3)}{(2l+1)^2}}, \\
\alpha_6 &\equiv \sqrt{\frac{(l+m)(l+m-1)(2l-1)}{(2l+1)^2}}, \alpha_7 \equiv \sqrt{\frac{(l-m+2)(l-m+1)(2l+3)}{(2l+1)^2}}
\end{aligned} \tag{4.5b}$$

and

$$p_l^m(k', z') = \int_{\rho'=0}^{\infty} D(\theta_0) \frac{e^{-z'/\cos\theta_0}}{R'^2} \frac{P_l^m(\cos\theta_0)}{U_l^m} J_m(k'\rho') \rho' d\rho' \tag{4.5b}$$

Note that the linear system (4.5) is identical to (3.23) for the collimated beam except for the forcing term that is proportional to (4.5b). The homogeneous solution of (4.5) thus remains the same (and is given in (3.30)), but the particular solution differs.

#### 4.1 Particular Solution

Although the spherical beam appears very similar to the collimated beam in the formulation of the solution, the computational complexity involved is significant. Two approaches to finding the particular solution are presented below.

##### 4.1.1 The Fourier-Cosine Approach

Let

$$p_{m,l}(k', z') = e^{-z'} G_{m,l}(k', z') \tag{4.6}$$

with

$$G_{m,l}(k', z') = \int_{\rho'=0}^{\infty} D(\theta_0) \frac{e^{-z'/\cos\theta_0 + z'}}{R'^2} \frac{P_l^m(\cos\theta_0)}{U_l^m} J_m(k'\rho') \rho' d\rho' \tag{4.6a}$$

In (4.6), the exponential factor  $e^{-z'}$  was removed from the integral over  $\rho'$  in the forcing term  $p_l^m(k', z')$  in the system of equations (4.5). The remaining integral (4.6a) still approaches zero as  $z' \rightarrow \infty$ , i.e.,  $G_{m,l}(k', z') \rightarrow 0$  for  $z' \rightarrow \infty$  as required for the Fourier-Cosine transform to exist.

The Fourier-Cosine transform of  $G_{m,l}(k', z')$  takes the form



$$G_{m,l}(k', z') = \int_{u=0}^{\infty} \tilde{G}_{m,l}(k', u) \cos(uz') du = \frac{1}{2} \int_{u=-\infty}^{\infty} \tilde{G}_{m,l}(k', u) e^{iuz'} du \quad (4.7)$$

where

$$\begin{aligned} \tilde{G}_{m,l}(k', u) &= \tilde{G}_{m,l}(k', -u) = \frac{2}{\pi} \int_{z'=0}^{\infty} G_{m,l}(k', z') \cos(uz') dz' \\ &= \frac{2}{\pi} \int_{z'=0}^{\infty} \int_{\rho'=0}^{\infty} D(\theta_0) \frac{e^{-z'/\cos\theta_0 + z'}}{R'^2} \frac{P_l^m(\cos\theta_0)}{U_l^m} J_m(k'\rho') \cos(uz') \rho' d\rho' dz' \end{aligned} \quad (4.7a)$$

Thus, the forcing term in (4.5) for the coefficients  $b_{m,l}^{\nu}$  becomes

$$p_{m,l}(k', z') = e^{-z'} G_{m,l}(k', z') = \frac{1}{2} \int_{u=-\infty}^{\infty} \tilde{G}_{m,l}(k', u) e^{-[1-iu]z'} du \quad (4.8)$$

In this form, the  $z$ -dependence of  $p_{m,l}(k', z')$  is exponential, as desired, and the calculation of the particular solution follows standard procedure, i.e., one assumes that

$$b_{m,l}^{\nu,p}(k', z') = \int_{u=-\infty}^{\infty} \tilde{b}_{m,l}^{\nu,p}(k', u) e^{-[1-iu]z'} du \quad (4.9)$$

And, therefore,

$$\frac{\partial b_{m,l}^{\nu,p}(k', z')}{\partial z'} = - \int_{u=-\infty}^{\infty} [1-iu] \tilde{b}_{m,l}^{\nu,p}(k', u) e^{-[1-iu]z'} du \quad (4.10)$$

Substitution of (4.9) and (4.10) into (4.5) yields the following linear system of equations

$$\begin{aligned} \alpha_1 [-[1-iu] \tilde{b}_{m,l-1}^{\nu,p} - i\nu\omega' \tilde{b}_{m,l-1}^{\nu,p}] + \alpha_2 [-[1-iu] \tilde{b}_{m,l+1}^{\nu,p} - i\nu\omega' \tilde{b}_{m,l+1}^{\nu,p}] + \alpha_3 [1-W_0 g_l + i\nu\omega'] \tilde{b}_{m,l}^{\nu,p} \\ + \frac{k'}{2} \bar{\varepsilon}_m [\alpha_4 \tilde{b}_{m+1,l-1}^{\nu,p} - \alpha_5 \tilde{b}_{m+1,l+1}^{\nu,p}] + \frac{k'}{2} \delta_m [\alpha_6 \tilde{b}_{m-1,l-1}^{\nu,p} - \alpha_7 \tilde{b}_{m-1,l+1}^{\nu,p}] = \frac{1}{2[\varepsilon_m(2l+1)]^{1/2}} g_l \tilde{G}_{m,l}(k', u) \end{aligned} \quad (4.11)$$

$$m = 0, 1, 2, \dots, N; \quad l = m, m+1, \dots, N; \quad 0 \leq k', z' < \infty$$

where all parameters have been defined in (4.5).

Once the linear system (4.11) is solved, the particular solution is found via (4.9). Because of the common exponential factor  $e^{-z'}$  in (4.9), the particular solution decreases with  $z'$  as required. Partial fields that increase with  $z'$  (which in principle are allowed by the transport equation but are unphysical) are automatically excluded in this formulation. Since the exponential factor was removed from the modified

forcing term  $G_{m,l}(k', z')$ , this term decreases slowly with  $z'$  and extends over a relatively wide  $z'$ -range.

Hence, its Fourier transform  $\tilde{G}_{m,l}(k', u)$  is relatively narrow-band in  $u$ , which reduces the numerical burden associated with the computation of the overall particular solution since only narrow band of  $u$  values are needed. Once the particular solution is determined, the final specific intensity and the received power are found by proceeding in the manner described in Chapter 3.

The method presented above for the spherical beam is computationally demanding. This is because calculation of  $\tilde{G}_{m,l}(k', u)$  requires evaluation of a double integral over  $\rho'$  and  $z'$  via (4.7a) and the determination of the overall particular solution then requires an additional integration over  $u$  (though over a limited  $u$ -range). In addition, a summation over  $\nu$  is needed to obtain the time-dependent specific intensity. In this report, only the time-independent case is numerically treated for the spherical beam.

#### 4.1.2 Finite Difference Solution

An alternative approach to finding the particular solution for the spherical beam case is to use a finite difference scheme to solve (4.5). In this approach, the  $z'$ -coordinate is discretized by setting  $z' = j\Delta z'$ ,  $j = 0, 1, 2, \dots$ , and the differential quotients in (4.5) are replaced by the difference quotients:

$$\frac{\partial b_{m,l}^{\nu,p}(k', z')}{\partial z'} \approx \frac{b_{m,l}^{\nu,p}(k', j\Delta z') - b_{m,l}^{\nu,p}(k', (j-1)\Delta z')}{\Delta z'} \quad (4.12)$$

To solve the resultant system of equations, the finite difference method requires values for all the coefficients in a boundary plane  $z = \tilde{z}$ . This is provided by approximating the diffuse intensity in the boundary plane using first order multiple scattering theory. This scattering theory yields good results for the diffuse intensity at small penetration depths into the forest. Hence, the boundary plane can be chosen to be located at  $\tilde{z} = 0$  or 1, for example, whichever is more accurate.

With the diffuse intensity  $I_d \approx I_{d,0}^{FO}(\rho', z' = \tilde{z}', \theta, \psi)$  known from first order theory (the time-independent case is only considered, which means that  $\nu = 0$  in (3.5)), the coefficients  $b_{m,l}^{\nu,p}(k', \tilde{z}')$  are found by using the representation

$$I_{d,0}(\rho', \tilde{z}', \theta, \psi) = \sum_{m=0}^{\infty} \int_{k'=0}^{\infty} \sum_{l=m}^{\infty} (2l+1) Q^0(k', w) b_{m,l}^{0,p}(k', z') \frac{P_l^m(\cos \theta)}{U_l^m} \frac{\cos(m\psi)}{V^m} J_m(k' \rho') k' dk' \quad (4.13)$$



where  $Q^\nu(k', w') b_{m,l}^{\nu,p}(k', z') = Q^0(k', w') b_{m,l}^{0,p}(k', z')$  for  $\nu = 0$  and then using the orthogonal relations

$$\int_{\theta=0}^{\pi} \frac{P_l^m(\cos \theta)}{U_l^m} \frac{P_{l'}^m(\cos \theta)}{U_{l'}^m} \sin \theta d\theta = \delta_{l,l'} \quad , \quad \int_{\psi=0}^{2\pi} \frac{\cos(m\psi)}{V^m} \frac{\cos(m'\psi)}{V^{m'}} d\psi = \delta_{m,m'} \quad ,$$

$$\int_{\rho'=0}^{\infty} J_m(k'\rho') J_m(\tilde{k}'\rho') \rho' d\rho' = \frac{\delta(k' - \tilde{k}')}{\tilde{k}'} \quad (4.14)$$

to obtain

$$b_{m,l}^{0,p}(k', \tilde{z}') =$$

$$\int_{\rho'=0}^{\infty} \left[ \int_{\psi=0}^{2\pi} \int_{\theta=0}^{\pi} I_{d,0}^{FO}(\rho', \tilde{z}', \theta, \psi) \frac{P_l^m(\cos \theta)}{U_l^m} \frac{\cos(m\psi)}{V^m} \sin \theta d\theta d\psi \right] J_m(k'\rho') \rho' d\rho' \sin \theta d\theta d\psi \quad (4.15)$$

Again, once the particular solution is obtained, the procedure in Chapter 3 is used to find the specific intensity and the received power.

## 5. APPROXIMATE SOLUTIONS OF THE TIME-INDEPENDENT TRANSPORT EQUATION

### 5.1 Introduction

Although very accurate, the rigorous solutions presented are computationally intensive and take considerable computer time to generate meaningful data. They are thus limited in their utilization for real time applications as are often needed in military situations. To provide such real time data, approximate solutions are invaluable even though they are not as accurate as the rigorous solutions. Three approximate solutions are developed here for both the collimated and spherical beams. The first one is the first order multiple scattering solution which is valid at short penetration depths into the forest half-space. The second approximate solution is an asymptotic solution that is valid at large penetration depths. The third approximate solution, which is referred to as the composite approximate solution, is a combination of the first two. These solutions are simpler than the rigorous ones and are capable of providing real time results for the problem of propagation and scattering of millimeter-waves in a forest region.

### 5.2 First order Multiple Scattering Solution

The time-independent transport equations in cylindrical coordinates for the reduced incident and diffuse intensities along with boundary conditions are specified in (3.2). For first order scattering, the phase (scatter) function in the second integral on the right side of (3.2b) remains the same, however, the phase function in the first integral is approximated by a  $\delta$ -function in the forward direction. Physically, the second integral depicts coherent scattering into incoherent scattering, which is first order scattering, while the first integral describes incoherent scattering into itself, which is higher order scattering. The justification for using the delta function to characterize the higher order scattering in the transport equation is based on the assumption that particles (leaves, twigs, etc.) in the forest scatter strongly into the forward direction. Hence, the phase function in the first integral on the right side of (3.2b) is assumed to be given by

$$p(\gamma) \approx 4\pi\hat{\alpha} \frac{\delta(\theta - \theta')}{\sin \theta'} \delta(\phi - \phi') \quad (5.1)$$

where  $\hat{\alpha}$  is a parameter that is chosen to optimize this approximation.

Substitution of (5.1.1) into (3.2b) yields



$$\hat{s} \cdot \nabla' I_d + \bar{\sigma}_t I_d(\rho', \phi_x, z', \theta, \phi) = \frac{W_0}{4\pi} \iint_{4\pi} p(\gamma) I_{ri}(\rho', \phi_x, z', \tilde{\theta}, \tilde{\phi}) d\tilde{\Omega} \quad (5.2)$$

where

$$\bar{\sigma}_t \equiv 1 - \hat{\alpha} W_0 \quad (5.2a)$$

$$\cos \gamma = \cos \theta \cos \tilde{\theta} + \sin \theta \sin \tilde{\theta} \cos(\phi - \tilde{\phi}) \quad (5.2b)$$

and  $\partial / \partial \psi = -\partial / \partial \phi_x$  is used in the definition of the operator  $\hat{s} \cdot \nabla'$  in (2.9a) since  $\psi = \phi - \phi_x$ .

The solution  $I_d^{FO}$  to (5.2) that satisfies boundary conditions (3.2), called the first order multiple scattering solution, can be shown to be given by

$$I_d^{FO}(\rho', \phi_x, z', \theta, \phi) = \frac{W_0}{4\pi \cos \theta} \int_{\tilde{z}'=0}^{z'} e^{-\bar{\sigma}_t \frac{(z'-\tilde{z}')}{\cos \theta}} \left[ \iint_{4\pi} p(\gamma) I_{ri}(\tilde{\rho}', \tilde{\phi}_x, \tilde{z}', \tilde{\theta}, \tilde{\phi}) \sin \tilde{\theta} d\tilde{\theta} d\tilde{\phi} \right] d\tilde{z}'$$

for  $0 \leq \theta \leq \pi/2$  (5.3a)

$$I_d^{FO}(\rho', \phi_x, z', \theta, \phi) = -\frac{W_0}{4\pi \cos \theta} \int_{\tilde{z}'=z'}^{\infty} e^{-\bar{\sigma}_t \frac{(z'-\tilde{z}')}{\cos \theta}} \left[ \iint_{4\pi} p(\gamma) I_{ri}(\tilde{\rho}', \tilde{\phi}_x, \tilde{z}', \tilde{\theta}, \tilde{\phi}) \sin \tilde{\theta} d\tilde{\theta} d\tilde{\phi} \right] d\tilde{z}'$$

for  $\pi/2 \leq \theta \leq \pi$  (5.3b)

where  $\tilde{\theta}, \tilde{\phi}, \tilde{z}'$  are integration variables,  $\gamma$  is defined by (5.2b) and

$$\tilde{\rho}' = [\rho'^2 + (z' - \tilde{z}')^2 \tan^2 \theta - 2\rho'(z' - \tilde{z}') \tan \theta \cos(\phi - \tilde{\phi}_x)]^{1/2} \quad (5.3c)$$

$$\tan \tilde{\phi}_x = \frac{\rho' \sin \phi_x - (z' - \tilde{z}') \tan \theta \sin \phi}{\rho' \cos \phi_x - (z' - \tilde{z}') \tan \theta \cos \phi} \quad (5.3d)$$

Note that  $I_d^{FO}$  is continuous at  $\theta = \pi/2$ .

### 5.2.1 Collimated Beam

For the collimated beam having a Gaussian beam profile, the reduced incident intensity (3.10)

with  $\nu = 0$  is given for  $z' > 0$  by

$$I_{ri} = \tilde{I}_{ri,0}(\tilde{\rho}', \tilde{z}', \tilde{\theta}) = \sigma_t^2 \frac{P_{ave}}{\pi w'^2} e^{-(\tilde{\rho}'/w')^2} e^{-\tilde{z}'} \frac{\delta(\tilde{\theta})}{2\pi \sin \tilde{\theta}} \quad (5.4)$$

Substitution of (5.4) into (5.3) gives

$$I_d^{FO}(\rho', z', \theta, \psi) = \sigma_t^2 \frac{W_0 P_{ave} p(\theta)}{4\pi^2 w'^2 \cos \theta} \int_{\tilde{z}'=0}^{z'} e^{-\tilde{\sigma}_t(z'-\tilde{z}')-\tilde{z}'} e^{-(\tilde{\rho}'/w')^2} d\tilde{z}' \quad \text{for } 0 \leq \theta \leq \pi/2 \quad (5.5a)$$

$$I_d^{FO}(\rho', z', \theta, \psi) = -\sigma_t^2 \frac{W_0 P_{ave} p(\theta)}{4\pi^2 w'^2 \cos \theta} \int_{\tilde{z}'=z'}^{\infty} e^{-\tilde{\sigma}_t(z'-\tilde{z}')-\tilde{z}'} e^{-(\tilde{\rho}'/w')^2} d\tilde{z}' \quad \text{for } \pi/2 \leq \theta \leq \pi \quad (5.5b)$$

where  $\psi = \phi - \phi_x$  and  $\tilde{\rho}'$  is given by (5.3c).

The solution (5.5) is a first order multiple scattering solution, but with an improvement in that higher order scattering is included because of the approximation (5.1) which is justified because the phase function has a strong forward lobe.

### 5.2.2 Spherical Beam

For the spherical beam having a rotationally symmetric pattern function, the reduced incident intensity (4.2) with  $\nu = 0$  is given by

$$I_{ri} = \tilde{I}_{ri,0}(\rho', \phi_x, z'; \tilde{\theta}, \tilde{\phi}) = \sigma_t^2 \frac{P_{ave} D(\tilde{\theta}_0)}{4\pi \tilde{R}'^2} e^{-\tilde{z}'/\cos \tilde{\theta}_0} \frac{\delta(\tilde{\theta} - \tilde{\theta}_0) \delta(\tilde{\phi} - \tilde{\phi}_x)}{\sin \tilde{\theta}_0} \quad (5.6)$$

where

$$\cos \tilde{\theta}_0 = (\tilde{z}' - z'_0) / \tilde{R}', \quad \sin \tilde{\theta}_0 = \tilde{\rho}' / \tilde{R}', \quad \tilde{R}' = [\tilde{\rho}'^2 + (\tilde{z}' - z'_0)^2]^{1/2} \quad (5.6a)$$

Upon substitution of (5.6) into (5.3) it can be shown that

$$I_d^{FO}(\rho', z'; \theta, \psi) = \sigma_t^2 \frac{W_0 P_{ave}}{(4\pi)^2 \cos \theta} \int_{\tilde{z}'=0}^{z'} p(\tilde{\gamma}) \frac{D(\tilde{\theta}_0)}{\tilde{R}'^2} e^{-\tilde{\sigma}_t[\frac{(z'-\tilde{z}')}{\cos \theta}] - [\frac{\tilde{z}'}{\cos \tilde{\theta}_0}]} d\tilde{z}' \quad \text{for } 0 \leq \theta \leq \frac{\pi}{2} \quad (5.7a)$$

$$I_d^{FO}(\rho', z'; \theta, \psi) = -\sigma_t^2 \frac{W_0 P_{ave}}{(4\pi)^2 \cos \theta} \int_{\tilde{z}'=z'}^{\infty} p(\tilde{\gamma}) \frac{D(\tilde{\theta}_0)}{\tilde{R}'^2} e^{-\tilde{\sigma}_t[\frac{(z'-\tilde{z}')}{\cos \theta}] - [\frac{\tilde{z}'}{\cos \tilde{\theta}_0}]} d\tilde{z}' \quad \text{for } \frac{\pi}{2} \leq \theta \leq \pi \quad (5.7b)$$

where  $\psi = \phi - \phi_x$  and

$$\cos \tilde{\gamma} = \cos \theta \cos \tilde{\theta}_0 + \sin \theta \sin \tilde{\theta}_0 \cos \tilde{\psi}, \quad \tilde{\psi} = \phi - \phi_x \quad (5.7c)$$

Note that in the integrands in (5.7a,b), the expressions  $\cos \tilde{\gamma}$ ,  $\cos \tilde{\theta}_0$ ,  $\sin \tilde{\theta}_0$  and  $\tilde{R}'$  are functions of all the variables, i.e. they are functions of  $\rho', z', \theta, \psi$  and of the integration variable  $\tilde{z}$ .



### 5.3 Asymptotic Solution

#### 5.3.1 Case 1

In the forest at distant observation points on or near the  $z'$ -axis, the reduced incident intensity is negligible while the diffuse intensity decreases exponentially with  $z'$ , is independent of  $\rho'$  and  $\phi_x$ , and exhibits a scatter pattern that depends only on  $\theta$ , but not on  $\phi$  (observations that were made on examination of data of the rigorous solution for the collimated beam). In the development of an asymptotic theory for  $z' \gg 1$ ,  $\rho' \ll 1$  in the range  $0 \leq \theta \leq \pi$ , the time-independent transport equation in cylindrical coordinates (3.12) for diffuse intensity  $I_d = I_{d,0}$ ,  $\nu = 0$ , was shown to reduce to

$$\cos \theta \frac{\partial}{\partial z'} I_{d,0} + I_{d,0} = \frac{W_0}{4\pi} \iint_{4\pi} p(\gamma) I_{d,0} \sin \theta' d\theta' d\psi' \quad (5.8)$$

with boundary condition

$$I_{d,0} \rightarrow 0 \text{ as } z' \rightarrow \infty \quad (5.8a)$$

where  $\cos \gamma$  is given in (2.9b).

For  $z' \gg 1$  and  $\rho' \ll 1$ , assume that

$$I_d = I_{d,0} \approx I_{d,0}^{asy} \equiv A_0 e^{-\bar{\sigma}_\infty z'} S_\infty(\cos \theta) \quad (5.9)$$

with scatter pattern  $S_\infty(\cos \theta)$  taken to be a function of  $\cos \theta$  that is normalized to unity for  $\theta = 0$  and where  $A_0$  is a positive, real constant. Substitution of (5.9) into (5.8) gives

$$(1 - \bar{\sigma}_\infty \cos \theta) S_\infty(\cos \theta) = \frac{W_0}{4\pi} \iint_{4\pi} p(\gamma) S_\infty(\cos \theta') \sin \theta' d\theta' d\psi' \quad (5.10)$$

To solve (5.10), it is convenient to represent both  $S_\infty(\cos \theta)$  and  $p(\gamma)$  in terms of Legendre polynomials. Hence, assume

$$S_\infty(\cos \theta) = \sum_{l=0}^{\infty} (2l+1) b_l P_l(\cos \theta) \quad (5.11)$$

and, as in (3.16), assume

$$p(\gamma) = \sum_{l=0}^{\infty} (2l+1) g_l P_l(\cos \gamma) \quad (5.12)$$

where, as before in (3.19) for the scatter function (2.8),

$$g_l = \frac{2\alpha}{\Delta\gamma_s^2} \int_{\gamma=0}^{\pi} e^{-(\gamma/\Delta\gamma_s)^2} P_l(\cos \gamma) \sin \gamma d\gamma + (1-\alpha)\delta_{0l}, \quad \delta_{0l} = \begin{cases} 1, & \text{for } l=0 \\ 0, & \text{for } l \neq 0 \end{cases} \quad (5.12a)$$

Using the expansion (3.17) to convert (5.12) into the form (3.18) reduces the double integral in (5.10) to a single integral over  $\theta'$  since

$$\frac{1}{2\pi} \int_{\theta'=0}^{2\pi} p(\gamma) d\psi' \equiv \bar{p}(\cos \theta, \cos \theta') = \sum_{l=0}^{\infty} (2l+1) g_l P_l(\cos \theta) P_l(\cos \theta') \quad (5.13)$$

Hence, (5.10) becomes

$$(1 - \bar{\sigma}_{\infty} \cos \theta) S_{\infty}(\cos \theta) = \frac{W_0}{2} \int_{\theta'=0}^{\pi} \bar{p}(\cos \theta, \cos \theta') S_{\infty}(\cos \theta') \sin \theta' d\theta' \quad (5.14)$$

which is an integral equation for  $S_{\infty}(\cos \theta)$ .

Substituting (5.11) and the summation in (5.13) into (5.14) and using orthogonality and recursion relations yield the linear system of equations for the expansion coefficients  $b_l$ :

$$lb_{l-1} - \frac{1}{\bar{\sigma}_{\infty}} (2l+1)(1 - W_0 g_l) + (l+1)b_{l+1} = 0, \quad l = 0, 1, 2, \dots \quad (5.15)$$

The eigensolution  $b_l$  to the linear system (5.15) associated with the smallest real eigenvalue  $\bar{\sigma}_{\infty, \min}$  is used to construct the solution  $S_{\infty}(\cos \theta)$  in (5.9). All the other larger real eigenvalues decay faster and are ignored in the far zone. Because the diffuse intensity  $I_d$  physically represents power, it is a positive quantity and, therefore, the solution  $S_{\infty}(\cos \theta)$  used in (5.9) is also positive for all  $0 \leq \theta \leq \pi$ . As is shown in the numerical results,  $S_{\infty}(\cos \theta)$  is characterized by a strong maximum in the forward direction  $\theta = 0$  and is small in the backward region  $\pi/2 \leq \theta \leq \pi$ .

### 5.3.2 Case 2

A second asymptotic solution to the time-independent transport equation is developed below for  $z' \gg 1$ ,  $\rho' \gg 1$  with the requirement that  $\tan \theta_0 = \rho'/(z' - z'_0)$  remain sufficiently small in comparison to the angle width of  $S_{\infty}(\cos \theta)$ ;  $z'_0$  and  $\theta_0$  are defined in Figure 5.1. This latter constraint confines the observation point in a conical region about the beam axis. Hence, the diffuse intensity is assumed to be symmetric about the direction  $\theta_0$  rather than  $\theta = 0$  and to take the form



$$I_d = I_{d,0} \approx I_{d,0}^{asy} \equiv A_1 e^{-\bar{\sigma}_\infty R'} S_\infty(\cos \theta_1) \quad (5.16)$$

with  $S_\infty(\cos \theta_1)$  normalized to unity for  $\theta_1 = 0$  and where  $A_1$  is a positive, real constant.  $R'$  is the radial distance from the reference point  $\rho' = 0, z' = z'_0$  to the observation point  $(\rho', z', \phi_x)$  in the far zone, and the angle  $\theta_1$  is the elevation angle in the scatter direction counted from the direction  $(\theta_0, \phi_x)$  through the observation point; see Figure 5.1.

Substitution of (5.16) into the time-independent transport equation (3.12), with the reduced incident intensity set to zero since it is very small for  $z' \gg 1, \rho' \gg 1$ , gives

$$(1 - \bar{\sigma}_\infty \cos \theta_1) S_\infty(\cos \theta_1) = \frac{W_0}{4\pi} \iint_{4\pi} p(\gamma_1) S_\infty(\cos \theta'_1) \sin \theta'_1 d\theta'_1 d\psi'_1 \quad (5.17)$$

with

$$\cos \gamma_1 = \cos \theta_1 \cos \theta'_1 + \sin \theta_1 \sin \theta'_1 \cos(\psi_1 - \psi'_1) \quad (5.17a)$$

In Figure 5.1, only the angle  $\theta_1$  is shown, not the rotational azimuthal angle  $\psi_1 \equiv \phi_1 - \phi_x$ ;  $\psi_1$  could be included in Figure 5.1 as the azimuthal angle corresponding to the elevation angle  $\theta_1$  defined in the plane normal to the direction  $\theta_1 = 0$ . This definition for  $\psi_1$  is allowed because the integral takes a form which is independent of how the angular coordinate system is chosen since the phase function depends only on the difference between the directions of incidence and scattering.

Observe that the integral equation (5.17) for  $S_\infty(\cos \theta_1)$  is identical to the integral equation (5.10) for  $S_\infty(\cos \theta)$ , except for the substitution  $\theta \rightarrow \theta_1$ , which is purely a mathematical operation. Hence, the solution to (5.17) follows the development for the solution to (5.10) given above.

#### 5.4 Composite Approximate Solution

The first order multiple scattering solution of the time-independent transport equation, which is valid at small penetration depths  $z'$  in the forest, was shown to be given by (5.5) for the collimated beam and by (5.7) for the spherical beam. At large penetration depths ( $z' \gg 1$ ) and for fixed, relatively small off-axis observation points, the diffuse intensity was shown to take the asymptotic form (5.9) with  $\bar{\sigma}_\infty = \bar{\sigma}_{\infty, \min}$ . Note that both the asymptotic attenuation rate  $\bar{\sigma}_\infty$  and the asymptotic scatter pattern  $S_\infty$  depend only on

$p(\gamma)$  and  $W_0$ , i.e., on the parameters of the random medium, but are largely independent of the parameters of the incident beam. Using both the first order multiple scattering solution and the asymptotic solution, the following composite approximate solution is proposed for all  $z'$  and moderate values of  $\rho'$

$$I_d(\rho', z', \theta, \psi) \approx I_d^{comp}(\rho', z', \theta, \psi) \equiv I_d^{FO}(\rho', z', \theta, \psi)e^{-\beta z'} + I_d^{FO}(0, z', 0, 0)S_\infty(\cos \theta)[1 - e^{-\beta z'}] \quad (5.18)$$

where  $I_d^{FO}(z', \rho', \theta, \psi)$  is the first order multiple scattering solution for the diffuse intensity given by (5.5) for the collimated beam and by (5.7) for the spherical beam. The pattern function  $S_\infty(\cos \theta)$  is found as discussed in Section (5.3) and is independent of the type of incident wave involved, i.e., the pattern function is the same for the collimated and the spherical incident beam waves considered here. The attenuation coefficient  $\beta$  is chosen to optimize agreement between  $I_d^{comp}(\rho', z', \theta, \psi)$  and the rigorous solutions for  $I_d(\rho', z', \theta, \psi)$  given in Chapters 3 and 4 for the collimated and spherical beams, respectively.

Observe that according to (5.18) that  $I_d^{comp}(\rho', z', \theta, \psi) \approx I_d^{FO}(\rho', z', \theta, \psi)$  for  $z' \rightarrow 0$ , while  $I_d^{comp}(\rho', z', \theta, \psi) \approx I_d^{FO}(0, z', 0, 0)S_\infty(\cos \theta)$  for  $z' \rightarrow \infty$ . The latter limit yields estimates for the parameter  $\hat{\alpha}$  and the constant  $A_0$  since when  $z' \rightarrow \infty$  and  $\theta = 0$ , the scatter function  $S_\infty(1) = 1$  while  $I_d \approx I_{d,0}^{asy} = A_0 e^{-\bar{\sigma}_{\infty, \min} z'}$  and  $I_d^{comp} \approx I_{d,0}^{FO}(0, z', 0)$ , which is written here to show it is independent of  $\psi$ . Hence, the asymptotic attenuation rate  $\bar{\sigma}_{\infty, \min}$  can be set equal to the attenuation rate of the first order solution  $I_d^{FO}(0, z', 0)$  to obtain an estimate for the parameter  $\hat{\alpha}$  while the constant  $A_0$  can be estimated by setting it equal to the magnitude of  $I_d^{FO}(0, z', 0)$  using the estimated value of  $\hat{\alpha}$ . Since a rigorous solution was found for the collimated beam (see Chapter 3), the constant  $A_0$  is determined more accurately by plotting the ratio  $I_{d,0} / \bar{I}_{d,0}^{asy}$  versus  $z'$  as  $z' \rightarrow \infty$  for  $\rho' = 0$ ,  $\theta = 0$ , where  $I_{d,0}$  is the diffuse intensity determined from the rigorous solution,  $\bar{I}_{d,0}^{asy} \equiv I_{d,0}^{asy} / A_0 = e^{-\bar{\sigma}_{\infty} z'}$  since  $I_{d,0} / \bar{I}_{d,0}^{asy} \rightarrow A_0$  for  $z' \rightarrow \infty$ .

#### 5.4.1 Collimated and Spherical Beams

For the collimated beam, the term  $I_d^{FO}(\rho', z', \theta, \psi)$  in (5.18) is given by (5.5), which in the forward direction ( $\theta = 0$ ) is independent of  $\psi$  and reduces to



$$I_d^{FO}(\rho', z', \theta = 0) = \sigma_t^2 \frac{P_{ave} p(\theta = 0)}{4\pi^2 w'^2 \hat{\alpha}} e^{-(\rho'/w')^2} [e^{-\bar{\sigma}_t z'} - e^{-z'}] \quad (5.19)$$

with  $\bar{\sigma}_t = 1 - \hat{\alpha}W_0$  and  $p(0)$  equal to the phase function in (2.8) for  $\gamma = \theta = 0$ . For  $\rho' = 0$ ,  $\theta = 0$  the parameter  $\hat{\alpha}$  can be chosen using the limit  $I_d^{comp}(0, z', 0, \psi) \approx I_d^{FO}(0, z', 0) \approx I_d^{asy}$  for  $z' \rightarrow \infty$ . From (5.19) it then follows that one could choose  $\tau \equiv \bar{\sigma}_t / \bar{\sigma}_{\infty, \min} = (1 - \hat{\alpha}W_0)$  to find an initial estimate for  $\hat{\alpha}$ .

For the spherical beam, the term  $I_d^{FO}(\rho', z', \theta, \psi)$  needed in (5.17) is given by (5.7), which is then used to find  $I_d^{FO}(0, z', 0, 0)$ . In the forward direction ( $\theta = 0$ ) and on the  $z'$ -axis ( $\rho' = 0$ ), it can be shown that the first order solution in (5.7) reduces to the following expression (which is independent of  $\psi$ )

$$I_d^{FO}(0, z', 0) = \sigma_t^2 \frac{W_0 P_{ave} p(0) D(0)}{(4\pi)^2} \cdot \left\{ -\frac{e^{-\bar{\sigma}_t z'}}{z' + z'_0} + \frac{e^{-z'}}{z'_0} + (1 - \bar{\sigma}_t) e^{-z' + [1 - \bar{\sigma}_t] z'_0} [E_i(-[1 - \bar{\sigma}_t][z' + z'_0]) - E_i(-[1 - \bar{\sigma}_t] z'_0)] \right\} \quad (5.20)$$

where  $E_i(-x)$  is the exponential integral defined by

$$E_i(-x) = -\int_x^\infty e^{-t} \frac{dt}{t} = \gamma + \ln x - \int_{t=0}^x (1 - e^{-t}) \frac{dt}{t}, \quad (5.20a)$$

the Euler-Mascheroni constant  $\gamma = 0.5772156\cdots$ , and  $D(0)$  is the directive gain in the forward ( $\theta_0 = 0$ ) direction.

## 6. NUMERICAL RESULTS

### 6.1 Introduction

Numerical solutions by their very nature are approximate solutions. Therefore, attention must be paid to sources of inaccuracies. In general, errors can be minimized by increasing the truncation value for  $N$  at the expense of the computational time. As in [2] and [13] unless stated otherwise, the following global parameters are used in all of the simulations:  $W_0 = 0.75$ ,  $\Delta\gamma_s = 0.3$ ,  $\alpha = 0.8$ ,  $T' = 2$ ,  $\alpha_0 = 4\sqrt{5}$ ,  $\Delta\gamma_M = 0.012$ ; see [2,13] for physical justification of these assumed values. The following quantities vary among different simulations:  $N$ ,  $\nu_{\max}$ ,  $k_{\max}$ ,  $w'$ ,  $\rho'$ ,  $z'$ ,  $\theta$ ,  $\psi$ .

### 6.2 Scatter or Phase Function

Figure 6.1 shows the polar plot of both the exact expression (2.18) and the truncated series expansion (3.16) of the phase function. This figure shows no difference between the exact phase function and the approximated phase function. However, Figure 6.2 shows the semilog plot of the error  $\varepsilon_p$  between the exact and the approximated phase function, i.e.,

$$\varepsilon_p = \left| \frac{P_{\text{exact}} - P_{\text{approx}}}{P_{\text{exact}}} \right| \quad (6.1)$$

Evidently, the error (6.1) is small when taking a large number of terms for the Legendre polynomial expansion.

### 6.3 Convergence in Received Diffuse Power

Figures 6.3-6.7 allows one to observe the convergence in the numerical data that is obtained for the received diffuse power plotted versus time. By changing several parameters, particularly by increasing the value of  $N$ , and for different observation points, the convergence for received diffuse power curves is shown to improve.

In Figure 6.3 for an incident beam that is a plane wave, all of the received diffuse power curves in the crest region overlap with one another for different values of  $N$ . However, in the trough region, the received



diffuse power is observed to be the least accurate for  $N$  equals 23 and the most improved for  $N$  equal 47. Thus, better convergence is obtained by increasing  $N$ .

Similar to the plane wave case, the collimated beam wave with beamwidth of ten in Figure 6.4 shows a problematic convergence in the trough region. Even when  $N$  is thirty-nine, the curve in the trough region does not converge well. Note, however, that values of power in the trough region are very small. This may contribute to the numerical inaccuracy that is evident in this region, which may require using much larger values of  $N$  to improve the series representation of the solution.

In Figure 6.5 for the plane wave case ( $w' \rightarrow \infty$ ), the received power in the trough region seems to converge better for values near  $\theta_M = 9^\circ$  but appears to require larger values of  $N$  as  $\theta_M$  approaches zero. Similar to the plane wave case in Figure 6.5, Figure 6.6 shows that inaccuracies appear in the trough region as  $\theta_M$  approaches zero. As was shown in Figure 6.3, it is expected that larger values of  $N$  would yield more accurate results in the trough region. Since very low power occurs in the trough region and increasing  $N$  necessitates a considerable increase in computational time, values of  $w'$  greater than 10 were not considered. As will be seen shortly, such inaccuracies in the trough regions do not occur for small beam widths, such as  $w' = 1$ . Regardless of the different values of  $N$  used, it appears as shown in Figure 6.7 for the plane wave case that as the width  $w'$  of the incident beam wave becomes smaller, better convergence is obtained in the trough region.

#### 6.4 Comparisons with Quadrature Method

An alternative solution to the scalar time-dependent transport equation for narrow band, beam wave, pulse propagation in a forest is presented in [13]. In this method, referred to as the Quadrature or Q-method, the Fourier-Bessel transform is used along with the two-dimensional Gauss quadrature formula and an eigenvalue-eigenvector technique, following the procedure developed by Chang and Ishimaru for CW propagation [7,8]. Comparison of results obtained using the Q-method and the method presented here, referred to as the Spherical Harmonics-Hankel Transform or S-method, are presented in Figures 6.8 - 6.9. In Figure 6.8, the curves that are generated by the Q- method (lighter and thinner lines) lie very close to the curves that are generated by the S-method (darker and thicker lines). The two set of curves in Figure 6.9 display similar shapes and characteristics. Values nearly match each other over the crest region and possess the same shapes in the trough region. The Q- method yields consistently lower values for received power in

the trough region and in the vicinity of the crest maximum. Since the plane wave result was obtained using the method presented in [2], which is derivable from the S-method, it is reasonable to assume that the S-method is more accurate than the Q-method. This was expected since the Q-method is highly numerical as compared to the S-method. Since the plots of the data generated by two distinct methods essentially agree, credence is given to results based on the S-method.

## 6.5 Additional Considerations

The truncation at  $\nu_{\max} \geq 12$  of the series representation (2.5a) for the Gaussian incident pulses was found to yield values which agree sufficiently with the exact values determined from (2.2). In all the graphs,  $\nu_{\max}$  was chosen to lie between thirteen and fifteen in order that the received power curves also be accurate, the choice of  $\nu_{\max}$  being determined by a minimum error criteria. For example, in Figure 6.10, the normalized reduced incident power for different values of  $\nu_{\max}$  is plotted, which shows that  $\nu_{\max} \geq 12$  is needed to obtain sufficiently accurate results.

The  $k'_{\max}$  value that is required in the truncation of the Hankel transform in (3.31) is taken so that more than 99% of the integrand is included. To ensure that this is the case,  $k'_{\max}$  is selected to be  $5/w'$ , where  $w'$  is the normalized beamwidth.

The Gaussian quadrature method was used to perform the two integrations needed in the simulation. The  $k'$ -integration (3.31) is approximated by thirty-two terms while there are ninety-six terms for the integration over  $\gamma$ , which is needed to determine the expansion coefficient  $g_l$  in (3.19).

The solutions to the linear system of equations (3.28) for finding the particular solution and (3.39) for solving the boundary condition at  $z' = 0$  were obtained by using LU factorization, linear equation solver, and iterative refinement packages provided by the optimized LAPACK library. The eigenvalue solutions were obtained by using the ZGGEVX routine from the LAPACK library that is based on the QZ method in EISPACK [11]. When tested, both of these procedures gave absolute errors ranging from  $10^{-10}$  to  $10^{-16}$ . This accuracy is acceptable, as the library routines handle all variables using double precision, which means a precision that is accurate up to about sixteen digits.

Recall that the phase function is normalized in (2.8a) such that



$$\iint_{4\pi} p(\gamma) d\Omega = 4\pi \quad (6.2)$$

This dictates that  $g_0$  in (3.19) must equal unity. However,  $g_0$  does not equal unity when determined numerically from (3.19), which gives  $g_0 = 0.9881$  when  $\Delta\gamma_s = 0.3, \alpha = 0.8$ . To ensure that  $g_0$  is unity, the phase function  $p(\gamma)$  is redefined as  $p_{norm}(\gamma) = p(\gamma)/g_0$ , which guarantees that (6.2) is satisfied with  $p(\gamma)$  replaced by  $p_{norm}(\gamma)$ .

## 6.6 Boundary Condition

The diffuse intensity  $I_{d,0}$  is plotted versus  $\theta$  for  $\rho' = 0, z' = 0$  and  $w' = 10$  in Figure 6.11 to show that the boundary condition (3.2c) for the case  $\nu = 0$  is satisfied, i.e., that

$$I_{d,0} = 0 \text{ at } z' = 0, \quad 0 \leq \theta \leq \pi/2 \quad (6.3)$$

As seen in the graph, when  $\theta$  lies between  $0^\circ$  and  $90^\circ$ , the diffuse intensity is nearly zero. As  $N$  increases, the diffuse intensity becomes even smaller and closer to zero at  $z' = 0$  over the forward range  $0 \leq \theta \leq \pi/2$ .

Figure 6.12 shows that for different beamwidths  $w'$ , the boundary condition (6.3) is again very well satisfied for the case  $\nu = 0$ . Numerical inaccuracies produce the negligibly small, non-zero values for  $I_{d,0}$  over the range  $0 \leq \theta \leq 90^\circ$ . For  $\nu \neq 0$ , the boundary condition  $I_{d,\nu} = 0$  at  $z' = 0, \quad 0 \leq \theta \leq \pi/2$  is also well satisfied as shown in Figure 6.13 for  $\nu = 1$ . Observe that the values of  $|I_{d,1}|$  are significantly smaller than  $|I_{d,0}|$  as indicated in Figure 6.13 using the same parameters. Since  $\nu \neq 0$ , the diffuse intensity is complex, so its magnitude is plotted as distinct from the  $\nu = 0$  case, which is purely real.

## 6.7 Power Attenuation, Pulse Broadening and Distortion

In Figure 6.14, the diffuse intensity  $I_{d,0}$  at different off-axis locations initially increases rapidly, reaches its maximum in the vicinity of  $z' = 1$  and then attenuates more slowly as the beam penetrates deeper into the forest. The attenuation is also shown in the plots of received power in Figures 6.15-6.17 in the forward direction ( $\theta_M = 0$ ) and in Figures 6.18-6.19 in the direction  $\theta_M = 4.83^\circ$  for different values of penetration depths  $z'$  and different off-axis locations  $\rho'$ . The largest power is transmitted in the forward

direction ( $\theta_M = 0$ ) on the beam axis ( $\rho' = 0$ ). When the point of observation moves away from the  $z'$ -axis, the power decreases. Distortion in the trough region ( see e.g. the curve in Figure 6.16 for  $\rho' = 3$  ) occurs due to small numerical inaccuracy at the very low power levels.

Figure 6.18 clearly indicates that as the observation point moves away from the  $z' = 0$  boundary between the forest and the air, the received power not only attenuates but distorts due to pulse spreading. Figure 6.19 shows the received power for different beamwidths at different off-axis locations, but at the same penetration depth. Observe that as  $w'$  increases, the received power is stronger, the pulse shapes remain similar, but less distortion occurs in the trough region. The curves of received power that fall below  $-70$  dB are not included - because of inaccuracies. Figure 6.20 shows that in the crest region, all curves lie close together. The only difference occurs in the trough region where more pulse distortion occurs as the beamwidth  $w'$  gets smaller. Note that the  $w'=7$  case lies extremely close to the plane wave result, which shows the correct behavior of the solution as the beamwidth approaches large values.

Figures 6.21-6.23 depict power received at larger scan angles. In Figure 6.21 for  $\theta_M = 62^\circ$ , the received power is extremely low and exhibits considerable distortion as compared to the received power in Figure 6.20 for  $\theta_M = 4.83^\circ$ . The smaller widths possess the lowest received power in the trough region. The power received for the beam wave with  $w'=7$  resembles the plane wave case as noted previously. Figure 6.22 shows that the received powers lose their distinctive pulse shape for  $90^\circ < \theta_M < 180^\circ$ . In this range, the time variation of  $P'$  remains fairly constant but with magnitudes that continue to decrease as  $\theta_M$  approaches  $180^\circ$ . Figure 6.23 shows what happens to the received power for the range  $0 < \theta_M < 50^\circ$ . Observe that the crest of the received power decreases as  $\theta_M$  becomes larger. These graphs also indicate the effect of pulse broadening as the beam penetrates further into the forest. Figures 6.21-6.23 indicate that as  $\theta_M$  increases from  $0^\circ$ , the antenna receives less power and the pulse widens, indicating stronger multiscattering, while in the scan directions  $90^\circ < \theta_M < 180^\circ$ , the pulse loses its distinctive pulse shape; this happens because the antenna now faces the unbounded region ( $z' \rightarrow \infty$ ) in which considerable multiscattering occurs.



## 6.8 Angular Distribution of Diffuse Intensity

Figure 6.24 and 6.25 depict the scatter patterns of diffuse intensity  $I_{d,0}$  (time-independent case) at observation points in the forest both on and off the  $z'$ -axis at values of  $\rho'=0,1,2,2.5$ , and 3 and at two different penetration depths ( $z'=1$  and 5). In Figure 6.24 in the cross-sectional plane defined by  $\psi=0$  and  $\pi$  at the smaller value  $z'=1$ , observe that scattering near the axis is strongest in the forward  $\theta=0$  direction, but as the observation point gets further away from the  $z'$ -axis (i.e., for larger values of  $\rho'$ ), side scattering occurs. For larger values of  $z'$ , the patterns initially broaden. At the larger value  $z'=5$ , the scatter patterns exhibit a single major lobe that is tilted more away from  $z'$ -axis the larger the value of  $\rho'$ . At the observation point on the  $z'$ -axis ( $\rho'=0$ ), the major lobe is symmetrical about its maximum in the  $\theta=0$  direction. Additional plots (not presented here) showed that at even larger penetration depths, at observation points both on and off the  $z'$ -axis, the scatter patterns all covered to a symmetrical, narrow lobe with a maximum in the  $\theta=0$  direction, i.e. This observation led to the development of the asymptotic solution to the transport equation that was presented in Chapter 5. In Figure 6.25 in the cross-sectional plane defined by  $\psi=-\pi/2$  and  $\pi/2$ , the patterns initially broaden, become more isotropic in the backscatter direction in the range  $\pi/2 \leq \theta \leq \pi$ , and narrow in the forward scattering range  $0 \leq \theta \leq \pi/2$  (all the while diminishing in magnitude) and eventually – though not shown – coalesces into a single forward lobe (for all values of  $\rho'$ ) with a maximum in the  $\theta=0$  direction.

## 6.9 Approximate Solutions

In Figures 6.26-6.36, the diffuse intensity  $I_{d,0}$  for the collimated beam wave is plotted versus normalized penetration depth  $z'$  using the rigorous Spherical Harmonics-Hankel Transform (S) solution (3.31) for  $\nu=0$ , the first order solution (5.5a) and the composite solution (5.18). For  $\rho'=0$  and  $\theta=0$ , the composite solution is identical to the first order solution. For this case, three solutions are plotted in Figure 6.26 for  $\tau=1, 1.5$  and 2, which yields  $\hat{\alpha}=0.716, 0.408$  and 0.099, respectively, since  $\tau \equiv \bar{\sigma}_t / \bar{\sigma}_\infty = 1 - \hat{\alpha}W_0$ . From the curves, the first order solution for  $\tau=1$  yields the closest agreement with the rigorous S-method solution over the short, but important range  $0 < z' < 6.5$ , after which the first order solution for

$\tau = 1.5$  agrees best with the rigorous S solution over the large middle range  $6.5 < z' < 50$ . For  $z' > 50$ , the first order solution for  $\tau = 1$  again gives the best agreement. Note, however, that the diffuse intensity is very small for large penetration depths. The amplitude  $A_0$  of the asymptotic solution (5.9), referred to in the figures as Asymptotic #1, was determined as explained in Section 5.4 and was used here for both the amplitudes  $A_0$  in (5.9) and  $A_1$  in (5.16); the latter is referred to as Asymptotic #2 in the figures.

For the case  $\rho' = 0$  and  $\theta = 30^\circ$ , Figure 6.27 shows that the composite solution for  $\tau = 1.5$  agrees best with the rigorous S-method solution over the range  $0 < z' < 50$ , after which the composite solution for  $\tau = 1$  remains closest to the S-solution. For this case, the values of  $\beta$  were chosen (by trial and error) such that the maxima of the composite solutions coincide closely with the maximum of the rigorous solution; see Figure 6.27a.

Figure 6.28 for  $\rho' = 0$  and  $\theta = 30^\circ$  shows that a different choice for the parameter  $\beta$  for the composite solutions based on optimizing the results in Figure 6.33, rather than Figure 6.28, are not good choices. Neither the first order nor the composite solutions agrees with the S-solution in Figure 6.28a.

Figure 6.29 shows that the composite solution for  $\tau = 1$  gives a good estimate for the S-solution for  $0 < z' < 2$ ; the first order then is the better one, but soon the composite solution for  $\tau = 1.5$  is best until  $z' \approx 30$  when the first order solution then again agrees better with the S-solution. In Figure 6.29 note that the  $\beta$  values used were based on optimizing the composite solutions in Figure 6.27. Clearly, the composite solution has limited utility when  $\beta$  is not optimized. Similar comments apply to the remaining Figures 6.29-6.36.

From the data, it was determined that in the forward direction ( $\theta = 0$ ) the first order solution for  $\tau = 1$  can be used to approximate the rigorous S-solution and, therefore, is of use for real time situations (it does not depend on the choice of  $\beta$ ). This is significant because no information is needed from the rigorous solution. For  $\theta \neq 0$ , the first order solution is again useful, but for penetration depths  $z' > 10$ . Small penetration depths require adjustment of the attenuation parameter  $\beta$  to make the composite solution useful.



For  $\theta \neq 0$  and  $\rho' \geq 0$ , the parameter  $\beta$  for the composite solution needs to be optimized for each value of  $\theta$  and  $\rho'$ , i.e.,  $\beta$  can be selected to yield good results for the composite solution for the specified values of  $\theta$  and  $\rho'$ , but may not give good results for other values.

The curves presented in Figures 6.26-6.29 serve to illustrate how approximate solutions can be used to obtain sufficiently accurate estimates for the intensity of the signal in vegetation in real time for the soldier in the field.

## 7. CONCLUSION

The scalar time-dependent equation of radiative transfer was used to develop several theories of pulse beam wave propagation and scattering in vegetation, a medium characterized by many random discrete scatterers, which scatter energy strongly in the forward scattering direction. The specific problem analyzed is that of a periodic sequence of Gaussian shaped pulses incident from free space onto the planar boundary surface of a random medium half-space, such as a forest, that possesses a power scatter (phase) function consisting of a strong, narrow forward lobe superimposed over an isotropic background. After splitting the specific intensity into the reduced incident and diffuse intensities, the solution of the transport equation expressed in cylindrical coordinates in the random medium half-space was obtained by expanding the angular dependence of both the scatter function and the diffuse intensity in terms of Associate Legendre polynomials, by using a Fourier series/Hankel transform to obtain the equation of transfer for each spatial frequency, and by satisfying the boundary conditions that the forward traveling diffuse intensity be zero at the interface and zero at infinity.

Plots of intensity and received power in the random medium (forest) showed distortion due to pulse broadening, angular spread, power attenuation (especially at large penetration depths), and out-of-beam scattering. Comparison with a second completely different method of solution to the scale transport equation, called the Quadrature method, substantiated the results.

In addition, three new approximate theories were developed for beam waves. The first approximate theory, a first order multiple scattering theory, allowed for the estimation of the intensity at small penetration depths without resorting to computer intensive calculations while maintaining good accuracy. The second new theory yielded an asymptotic solution to the transport equation which is valid at large penetration depths into the forest. This allowed a characterization of the field deep in the forest also without extensive calculations. The third approximate theory was a composite solution which combined both the first order solution and the asymptotic solution and closed the gap between the first two approximate theories.

The three approximate theories were numerically compared to the rigorous theory. The first order theory was shown to agree with the rigorous theory at short vegetation penetration depths. At larger depths, it agrees in the forward scatter direction only, but not otherwise. The asymptotic theory was shown to have the correct behavior in all scatter directions and to agree with the rigorous theory at large penetration depths. The



development of an asymptotic theory is new; its feasibility was predicted by the extensive numerical data that was obtained from the rigorous theory. One important aspect of the asymptotic theory is that it is independent of the incident radiation and, therefore, remains valid for other cases as well and, in particular, for the spherical beam case.

As opposed to the rigorous theory, the three approximate theories are numerically efficient. The significance of this is that they are useful for near-real-time modeling of the wireless microwave communication channel in vegetation and, therefore, of interest to the soldier in the field.

## 8. REFERENCES

1. A. Ishimaru, *Wave Propagation and Scattering in Random Media, vol.1*. New York: Academic Press, 1978.
2. G.M. Whitman, F.K. Schwing, A. Triolo and N. Cho, "A Transport Theory of Pulse Propagation in a Strongly Forward Scattering Random Medium," *IEEE Transactions on Antenna & Propagation*, vol 44, no. 1, pp. 118-128, January 1996.
3. F.K. Schwing, E. J. Violette and R.H. Espeland, "Millimeter-Wave Propagation in Vegetation: Experiments and Theory," *IEEE Transactions on Geoscience and Remote Sensing*, vol. 26, no. 3, pp. 355-367, May 1988.
4. F.K. Schwing and R.A. Johnson, "A Transport Theory of Millimeter-Wave Propagation in Woods and Forests," *J. Wave-Material Interaction*, vol. 1, no. 2, pp. 205-235, April 1986.
5. G.M. Whitman, F.K. Schwing and J. Yuan, "Chebyshev Method of Solution to the Time-Dependent Transport Equation in Planar Geometry," *Proceedings of the 1985 International Symposium on Antennas and EM Theory*, pp. 171-177, Beijing, China: China Academic Publishers, August 1985.
6. G. M. Whitman, F.K. Schwing and N. Cho, "Moment Method Solution of the Time Dependent Transport Equation in Planar Geometry," *Proceedings of the 1985 International Symposium on Antennas and Propagation*, Kyoto, Japan, pp. 687-690, August 1985.
7. H-W. Chang and A. Ishimaru, "Beam Wave Propagation and Scattering in Random Media Base on the Radiative Transfer Theory," *J. of Wave-Material Interaction*, vol. 2, no. 2, pp. 41-69, January 1987.
8. H-W. Chang, "Beam Wave Propagation and Scattering in Random Media Base on the Radiative Transfer Theory," Ph.D. Dissertation, University of Washington, Seattle, 1986.
9. F.T. Ulaby, T.A. Van Deventer, J.R. East, T.F. Haddock and M.E. Coluzzi, "Millimeter-Wave Bistatic Scattering from Ground Vegetation Targets," *IEEE Transactions on Geoscience and Remote Sensing*, vol. 26, no. 26, pp. 229-243, May 1988.
10. A. Weinberg and E. Wigner, *The Physical Theory of Neutron Chain Reactions*, Chicago, Illinois: University of Chicago Press, 1958.
11. E. Anderson, Z. Bai, C. Bischof, S. Blackford, J. Demmel, J. Dongarra, J. Du Croz, A. Greenbaum, S. Hammarling, A. McKenney, and D. Sorensen, *LAPACK Users Guide*, 3rd ed. Philadelphia, PA: SIAM, [http://www.netlib.org/lapack/lug/lapack\\_lug.html](http://www.netlib.org/lapack/lug/lapack_lug.html), October 1999.
12. W.L. Stutzman and G.A. Thiele, *Antenna Theory and Design*, 2nd ed. New York: John Wiley and Sons, 1997.
13. S.K. Hu, "Bounded Beam Wave Pulse Propagation and Scattering in Random Media Based on the Radiative Transfer Theory using the 2-D Gauss Quadrature Formula," MS Thesis, New Jersey Institute of Technology, Newark, NJ, January 2000.



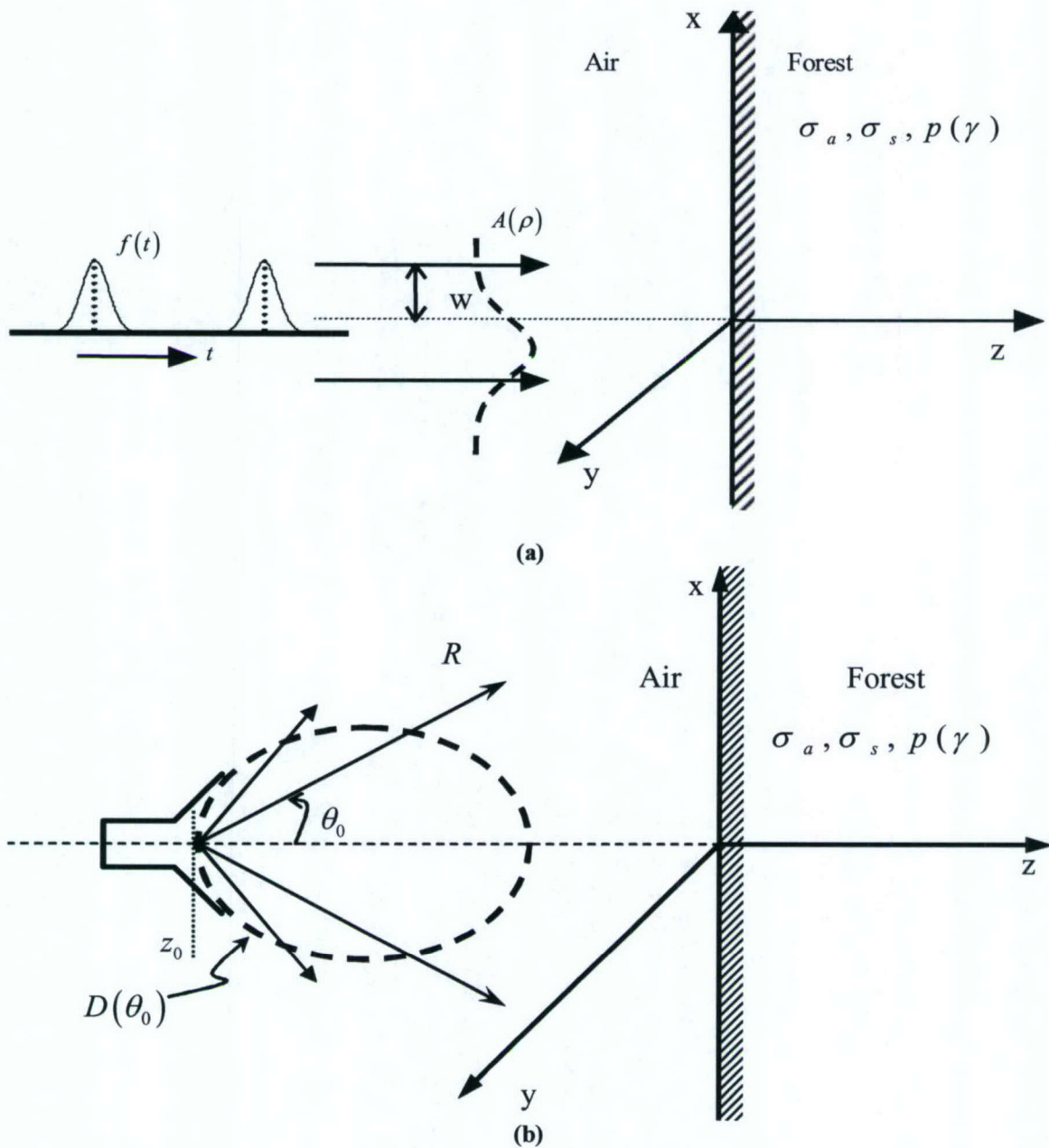


**Figure 2.1** Bounded beam wave pulse train incident onto a forest half-space  
 (a) Collimated incident beam wave pulse train with  $\rho$ -dependent Gaussian amplitude  $A(\rho)$   
 (b) Spherically diverging incident beam wave pulse train with directive gain  $D(\theta_0)$  and the phase center of the beam located at  $z = z_0 < 0$

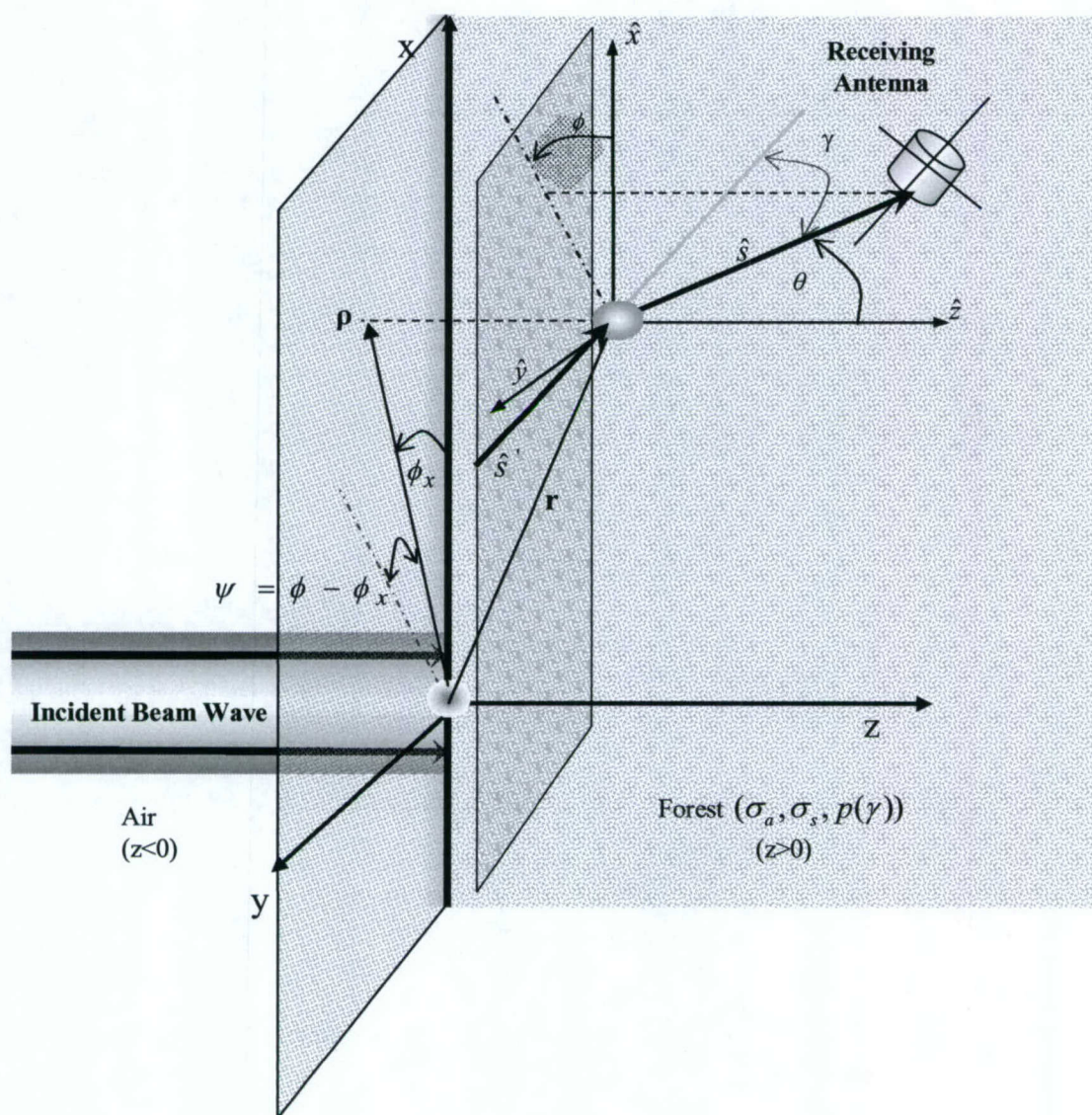


**Figure 2.2** The basic geometry for scattering in the forest half-space of an incident beam wave pulse train. The “sphere” represents a scatter point in the forest. The tilted cylinder represents a receiving antenna, which is shown enlarged in Figure 2.3.



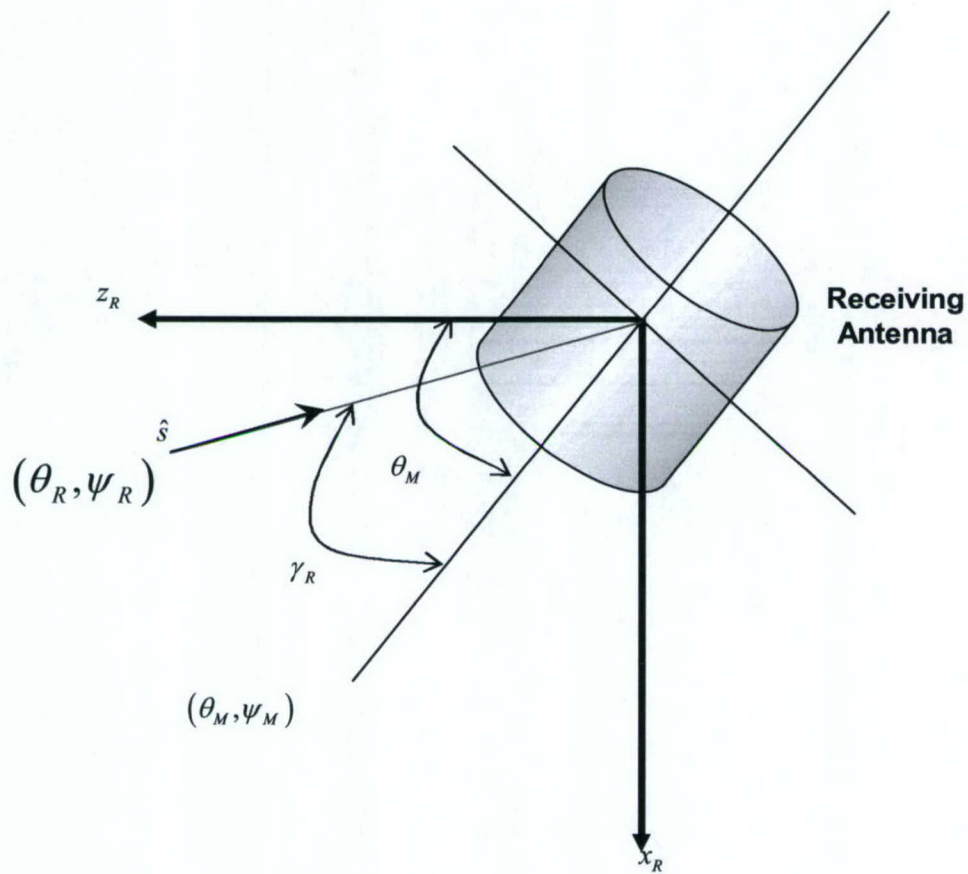


**Figure 2.3** The coordinate geometry of the receiving antenna, which is depicted as a tilted cylinder with a main beam direction  $(\theta_M, \psi_M)$ ; note  $\theta = \theta_M$ .

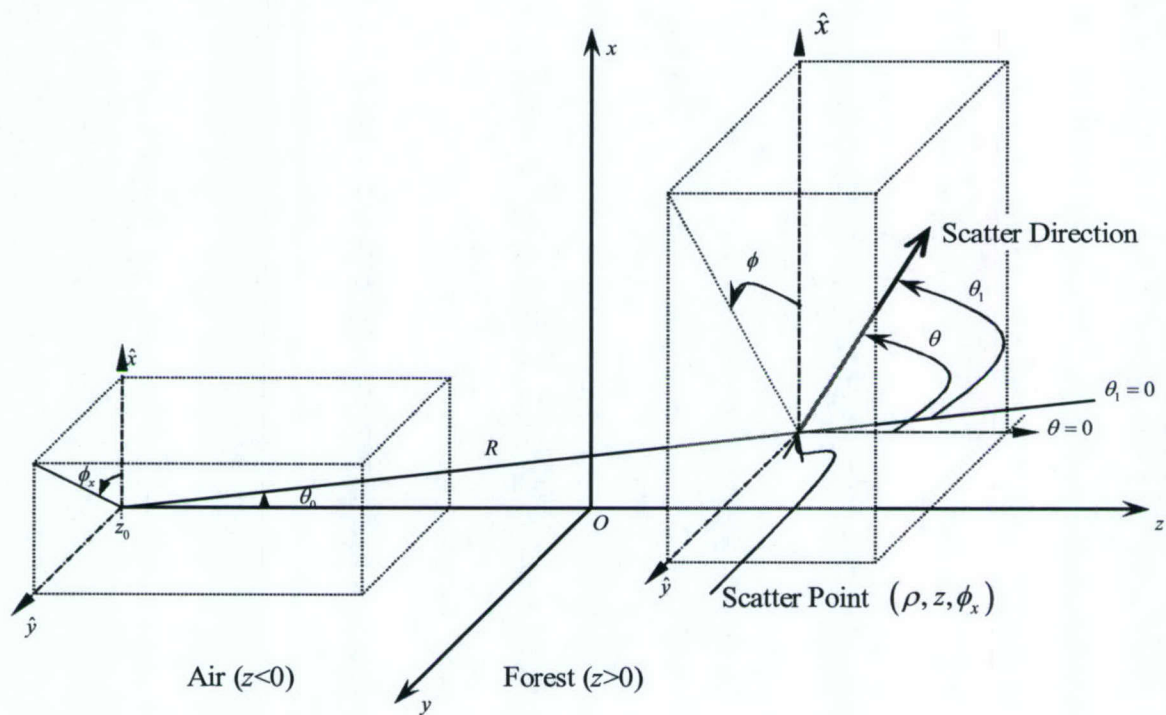


**Figure 5.1** Geometry for asymptotic solution, case 2.



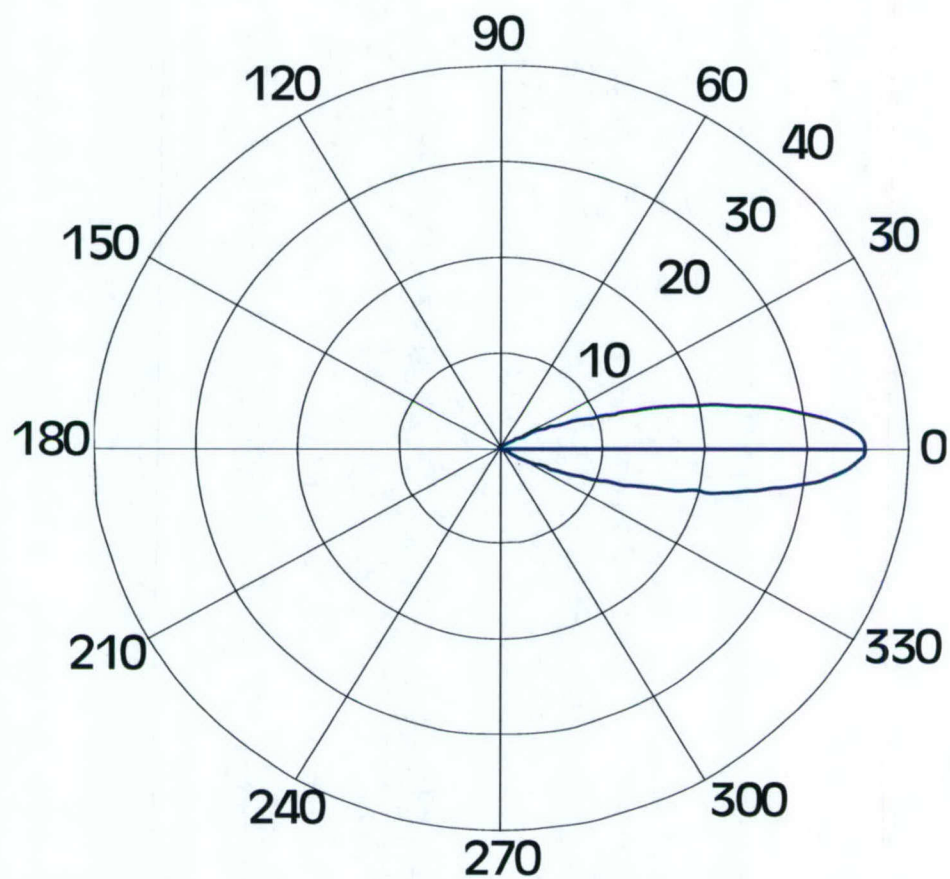


**Figure 6.1** Scatter or phase function  $p(\gamma)$  simulated by using (2.18) and by (3.16) truncated at  $N=31$ .

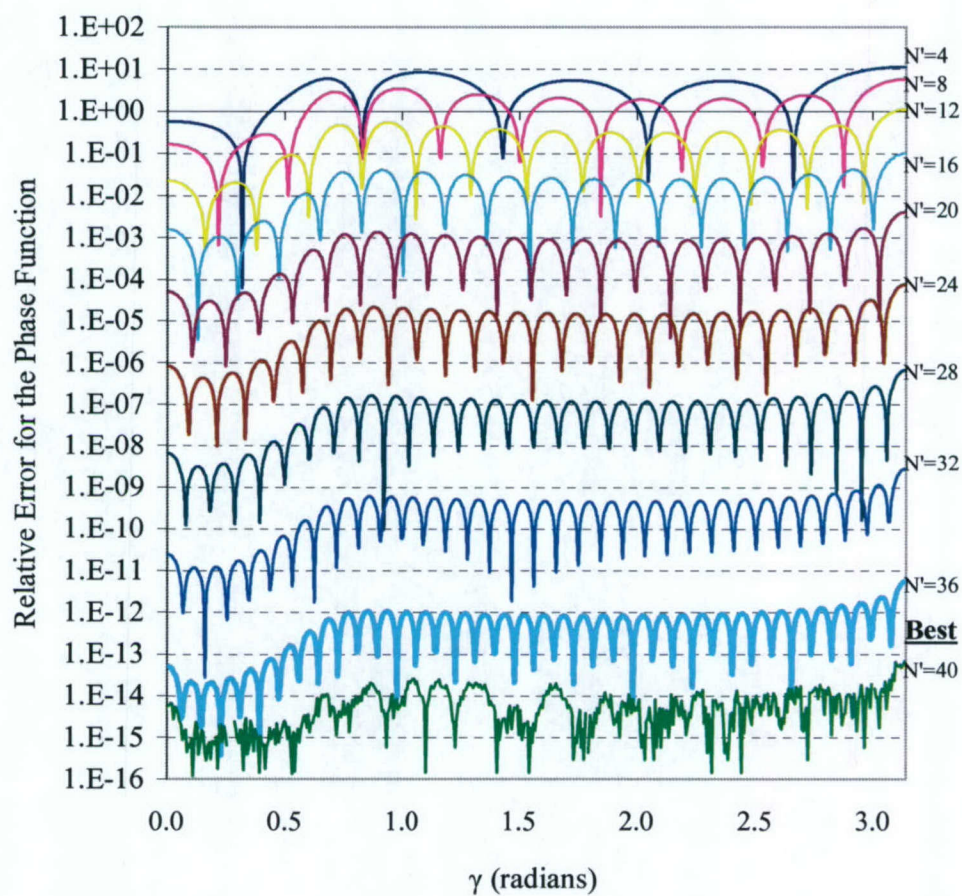


**Figure 6.2** Error analysis of the phase function, where  $N'=N+1$  is the number of terms for the truncation of (3.16).



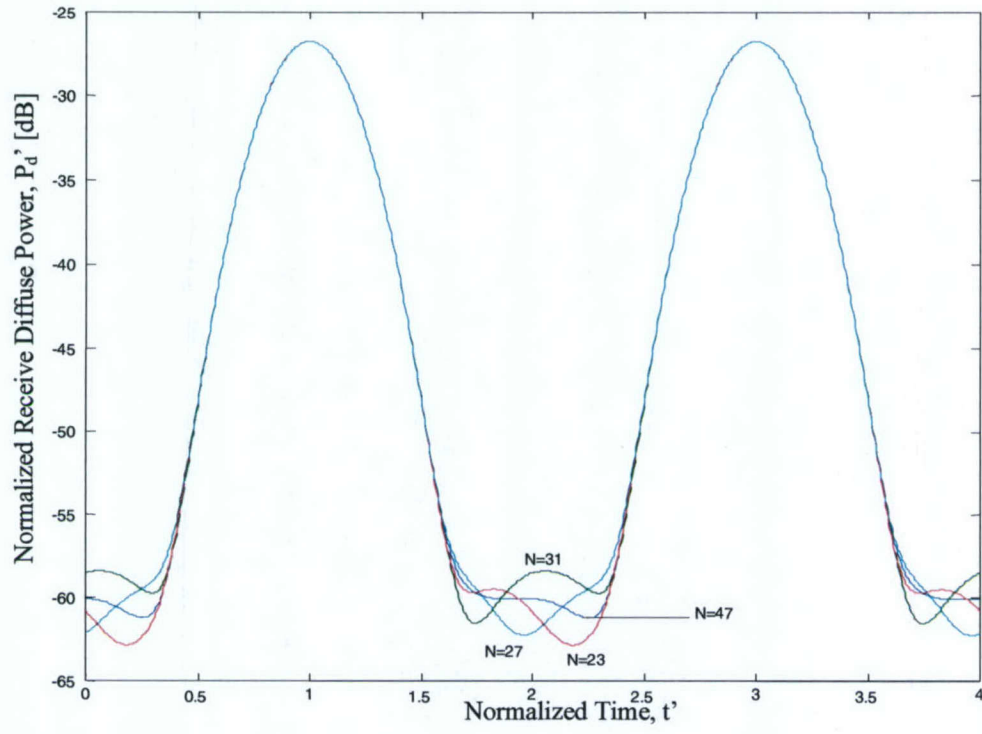


**Figure 6.3** Normalized received diffuse power  $P_d'$  versus normalized time  $t'$  for different values of  $N$  for  $w' \rightarrow \infty$  (plane wave),  $\rho' = 0$ ,  $z' = 1$ ,  $\theta_M = 0$  ( $\psi_M$  is undefined when  $\rho' = 0$ ),  $\nu_{\max} = 15$ .

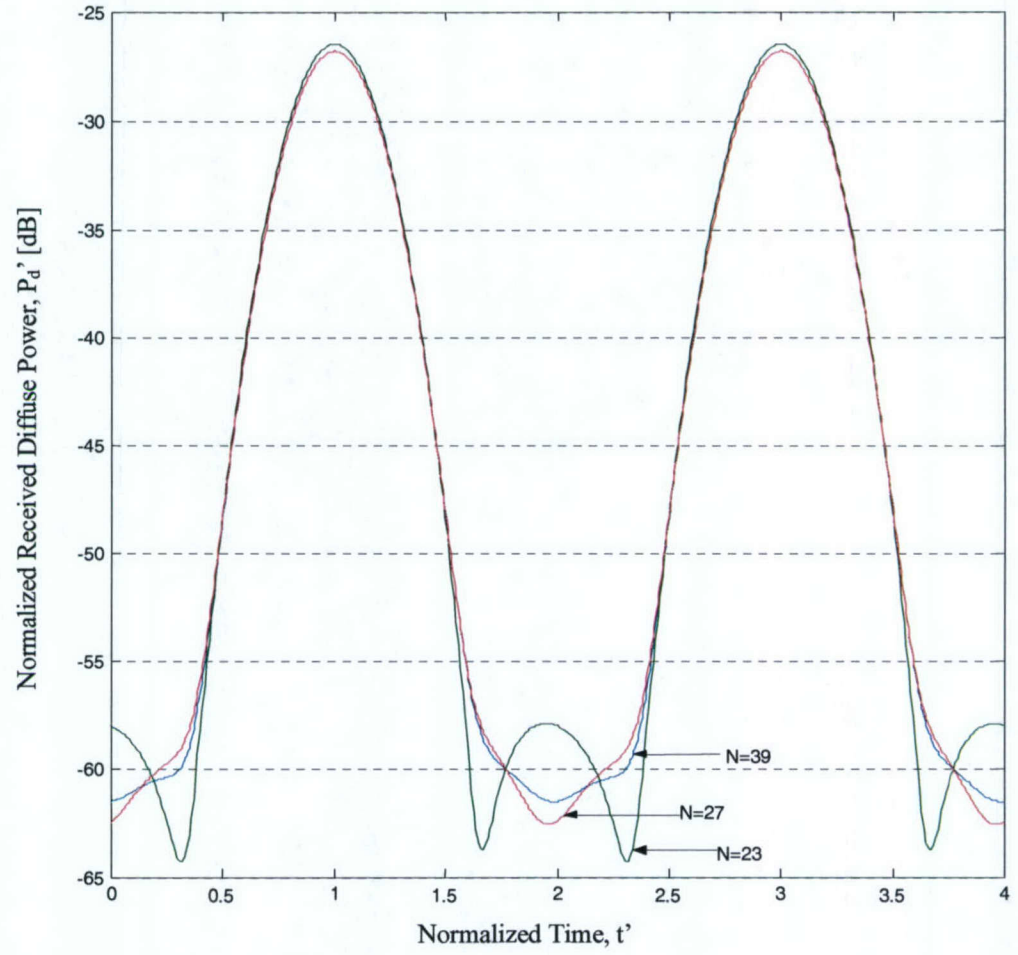


**Figure 6.4** Normalized received diffuse power  $P_d'$  versus normalized time  $t'$  for  $N=23, 27, 39$  and  $w'=10, \rho'=0, z'=1, \theta_M=0, \nu_{\max}=15$ .



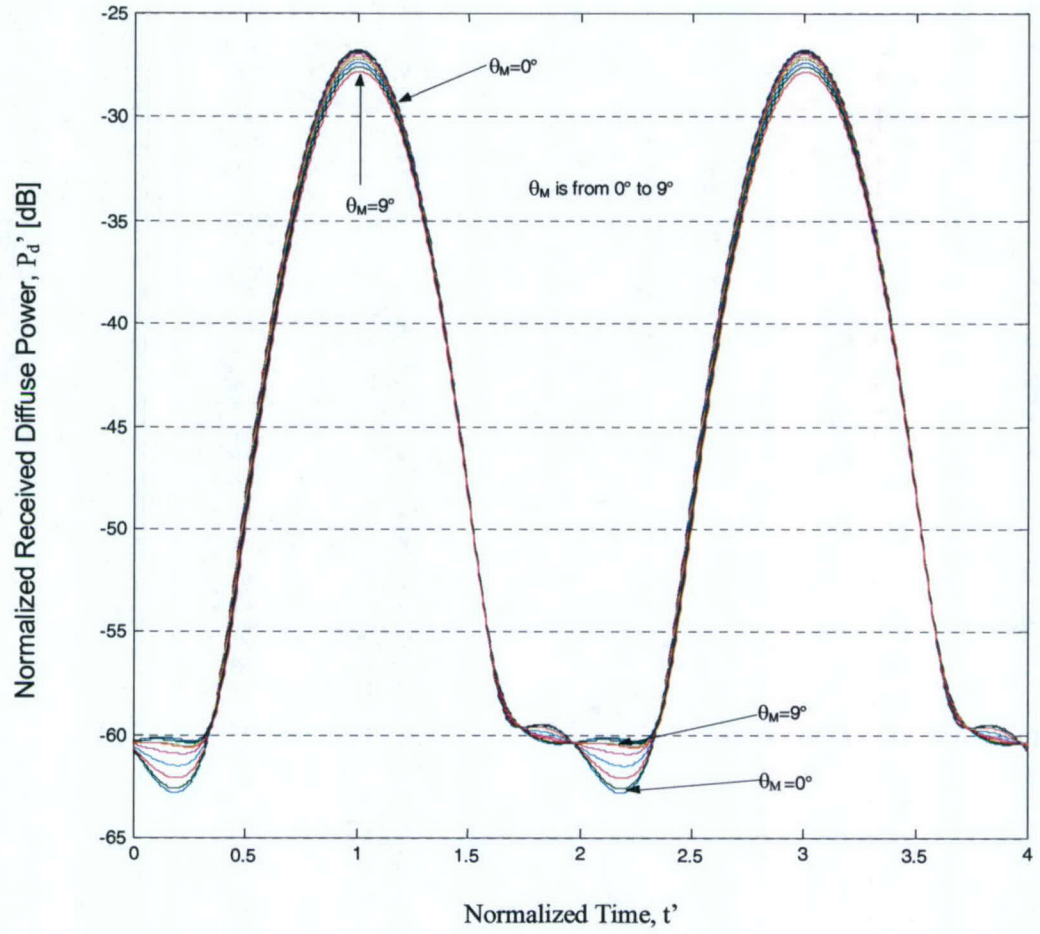


**Figure 6.5** Normalized received diffuse power  $P_d'$  versus normalized time  $t'$  for different values of  $\theta_M$  in the range  $0^\circ \leq \theta_M \leq 9^\circ$  and  $w' \rightarrow \infty$  (plane wave),  $\rho' = 0$ ,  $z' = 1$ ,  $v_{\max} = 15$ ,  $N = 31$ .

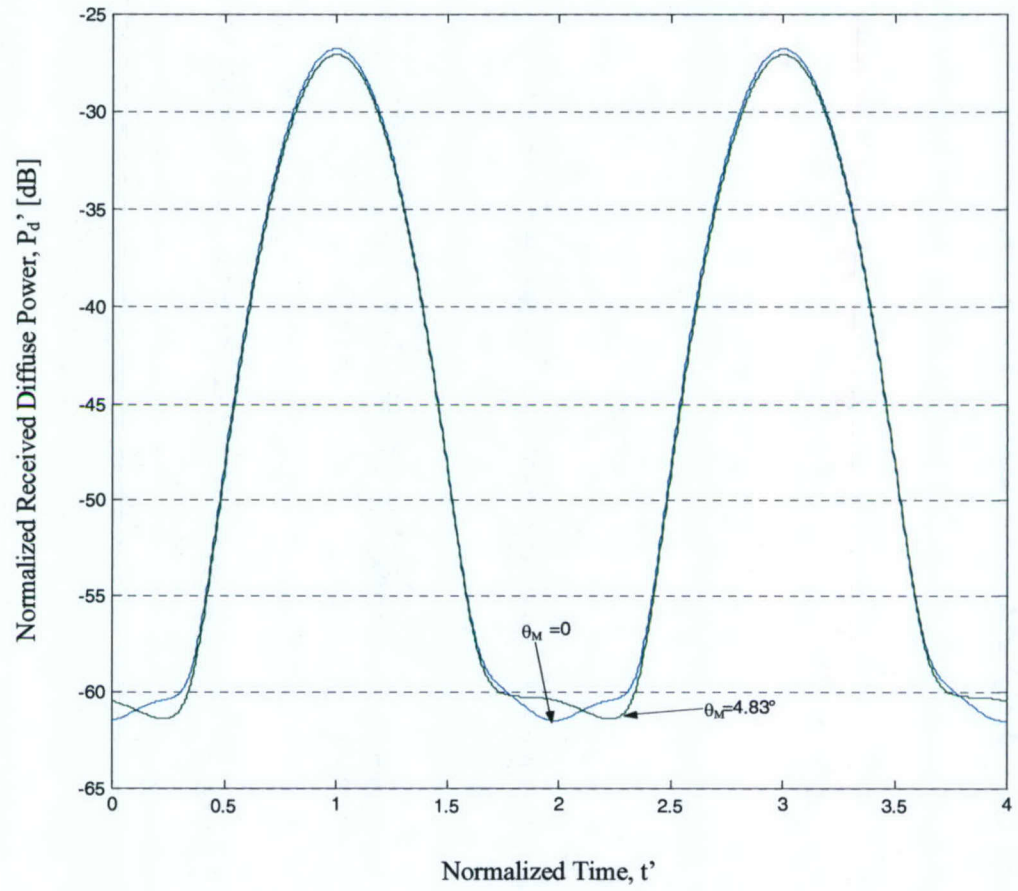


**Figure 6.6** Normalized received diffuse power  $P_d'$  versus normalized time  $t'$  for  $w' = 10$ ,  $\rho' = 0$ ,  $z' = 1$ ,  $\theta_M = 0^\circ$  and  $4.83^\circ$ ,  $\nu_{\max} = 15$ ,  $N = 39$ .



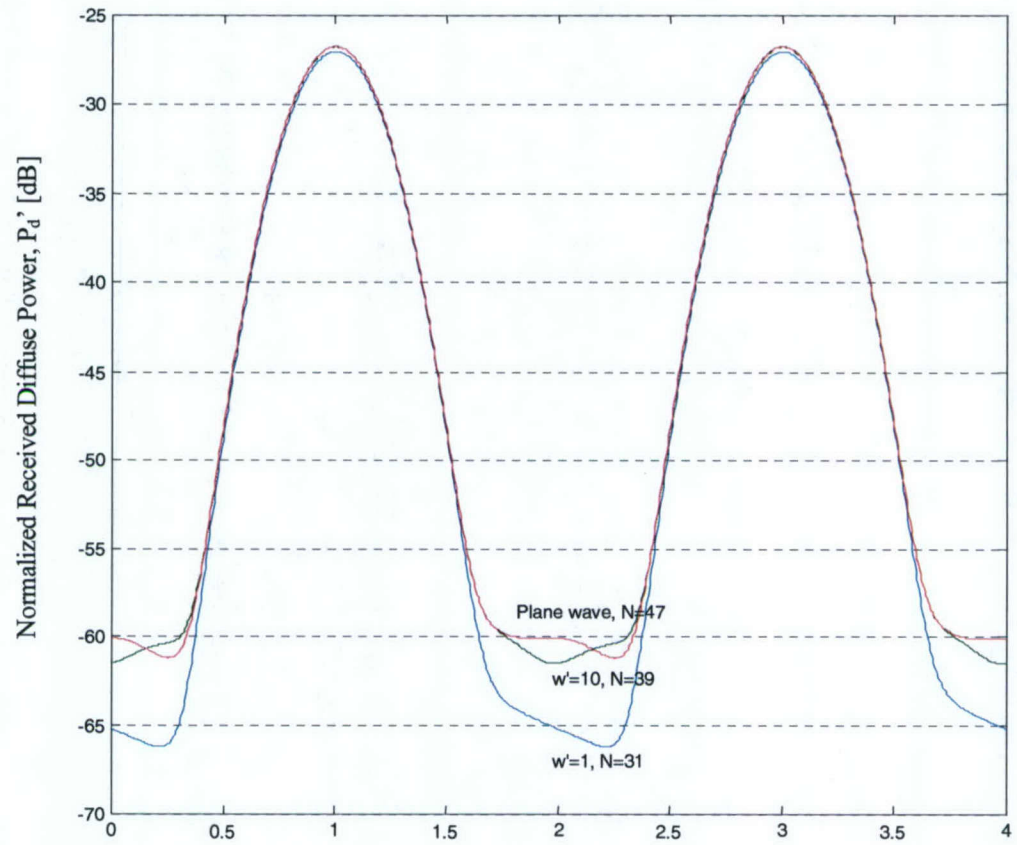


**Figure 6.7** Normalized received diffuse power  $P_d'$  versus normalized time  $t'$  for  $w'=1, 10$  and  $w' \rightarrow \infty$  (plane wave) with associated values of  $N = 31, 39$  and  $47$ , respectively, and  $\rho'=0, z'=1, \theta_M=0, v_{\max}=15$ .

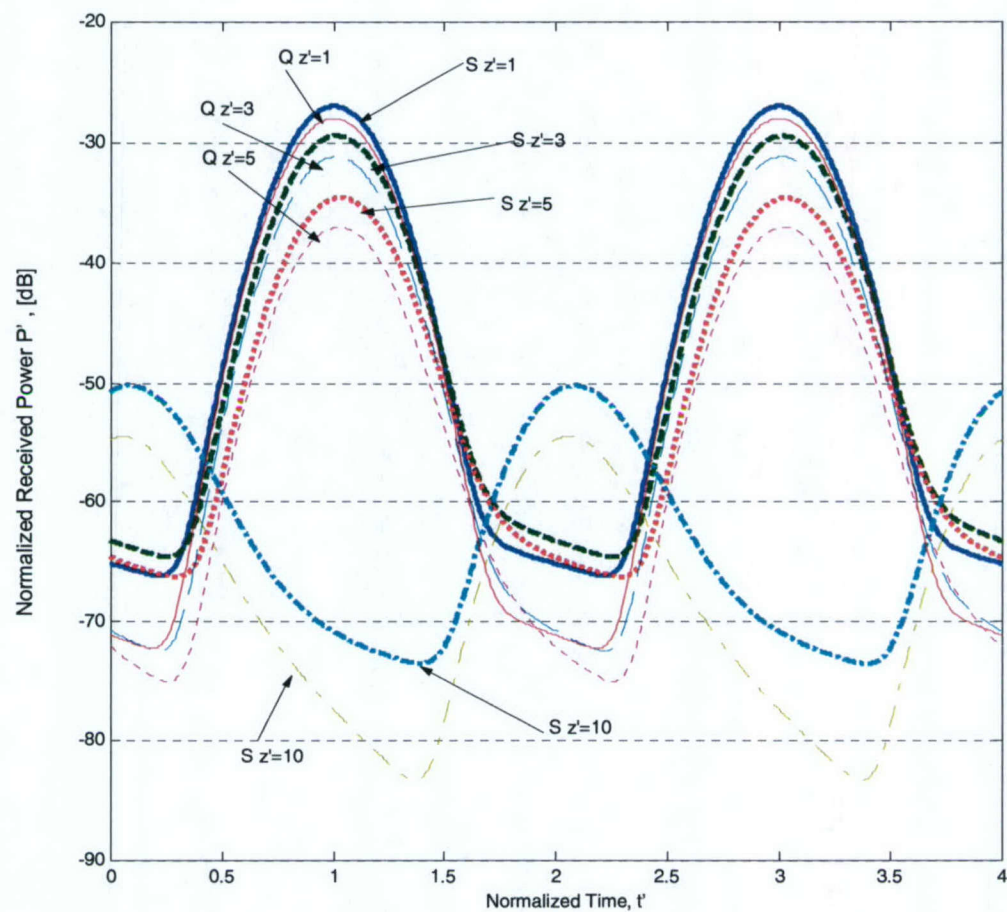


**Figure 6.8** Comparisons between Quadrature method (Q) and Spherical Harmonics-Hankel Transform method (S) of normalized received power  $P'$  versus normalized time  $t'$  for  $z'=1, 3, 5, 10$  and  $w'=1$ ,  $\rho'=0$ ,  $\theta_M=4.83^\circ$ ,  $v_{\max}=15$ ,  $N=31$ .

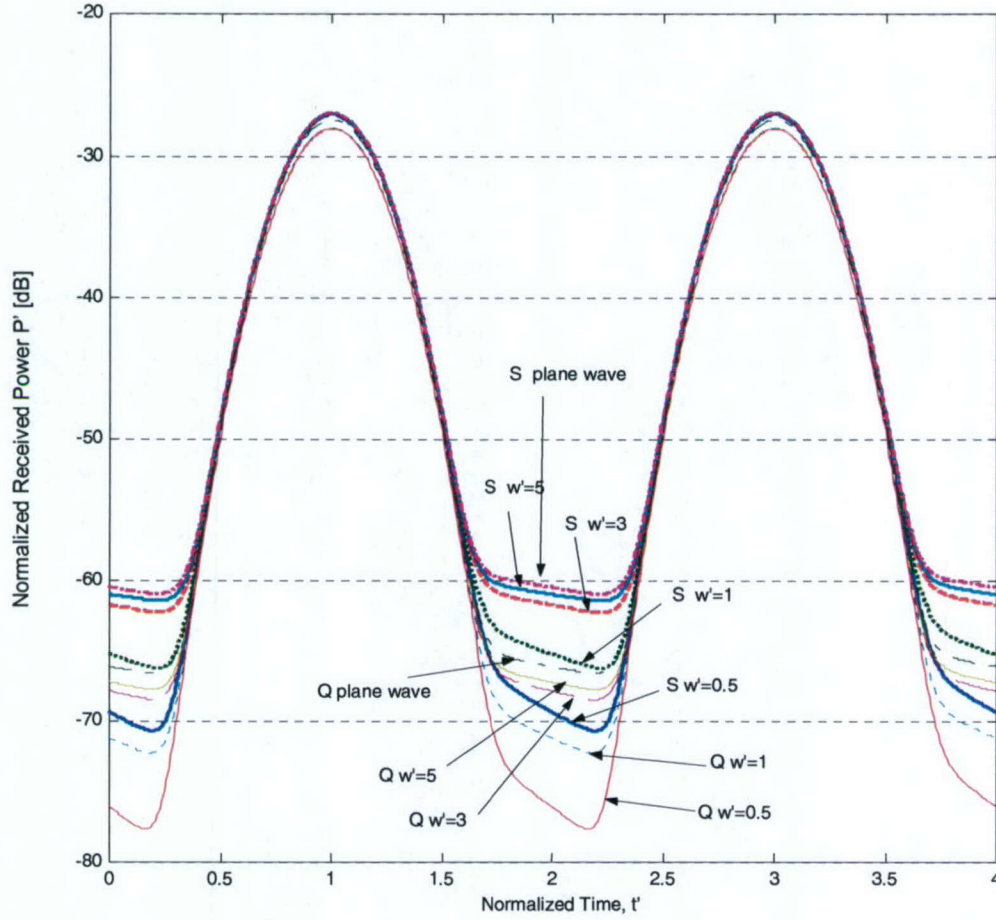


**Figure 6.9** Comparison between Quadrature method (Q) and Spherical Harmonics-Hankel Transform method (S) of the normalized received power  $P'$  versus normalized time  $t'$  for  $w' = 0.5, 1, 3, 5, \infty$  and  $\rho' = 0, z' = 1, \theta_M = 4.83^\circ, \nu_{\max} = 15, N = 27$ .



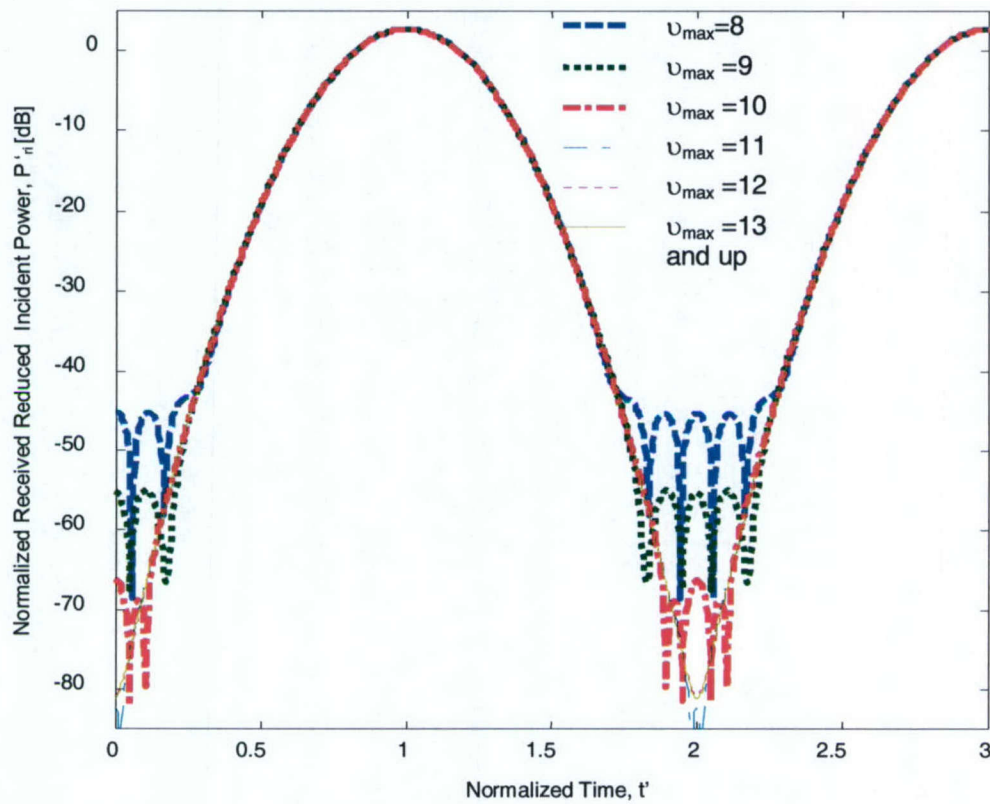


**Figure 6.10** Normalized reduced incident power  $P'_{ri}$  versus normalized time  $t'$  for  $\rho'=0$ ,  $z'=1$ ,  $\theta_M=0$  for different values of  $v_{max}$ .

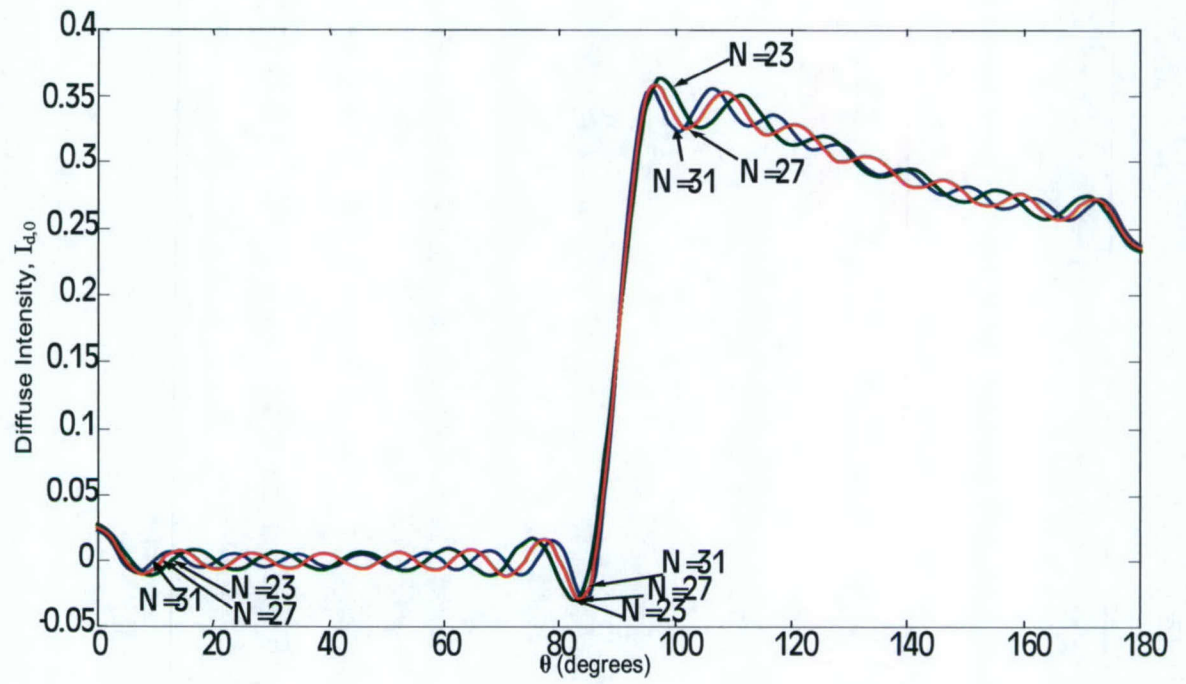


**Figure 6.11** Diffuse Intensity  $I_{d,0}$  versus  $\theta$  for  $w'=10$ ,  $\rho'=0$ ,  $z'=0$ ,  $v=0$  and  $N=23,27,31$ .

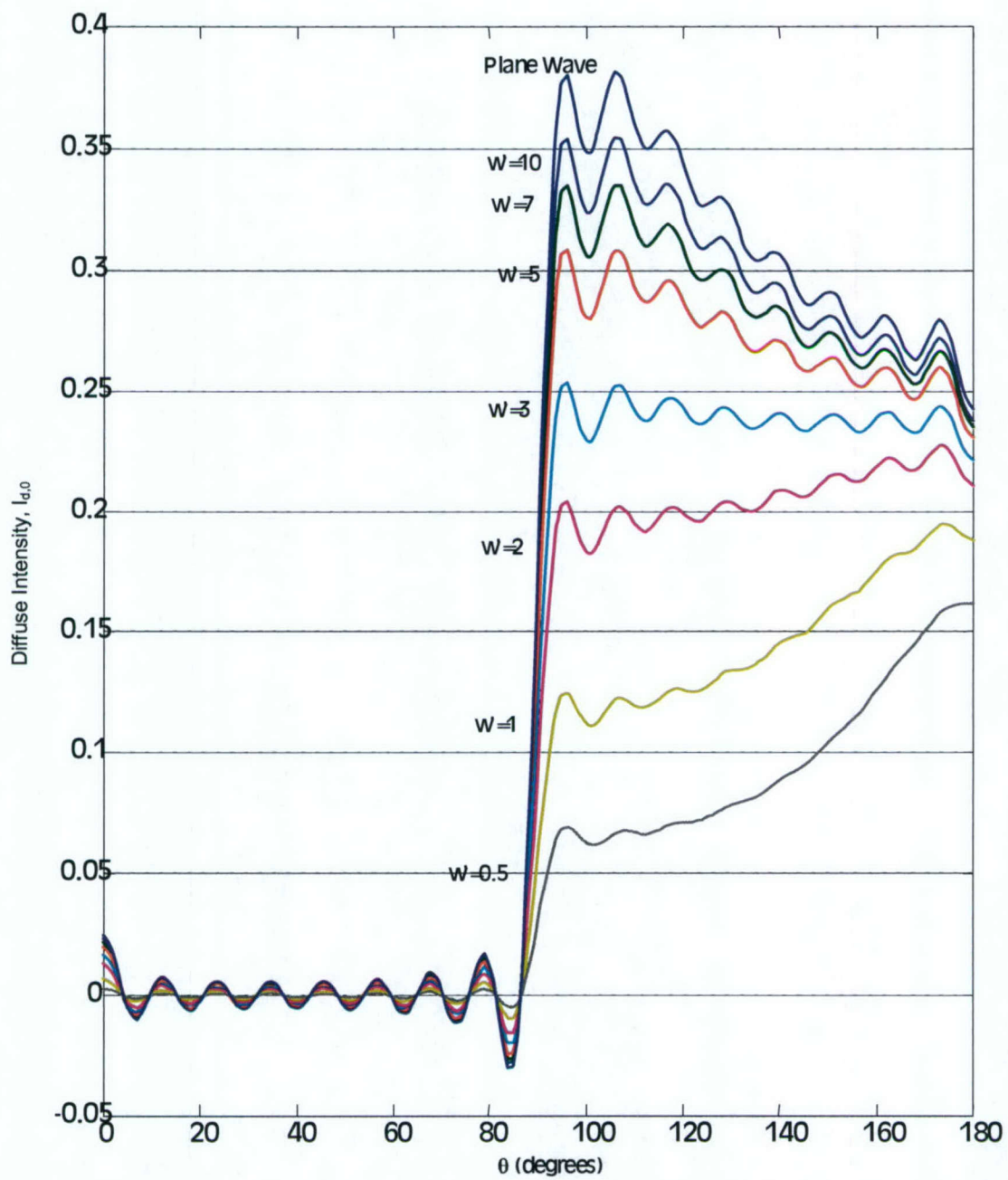


**Figure 6.12** Diffuse intensity  $I_{d,0}$  versus  $\theta$  for beamwidths  $w' = 0.5, 1, 2, 3, 5, 7, 10, \infty$  and  $\rho'=0$ ,  $z'=0$ ,  $v=0$ ,  $N=31$ .



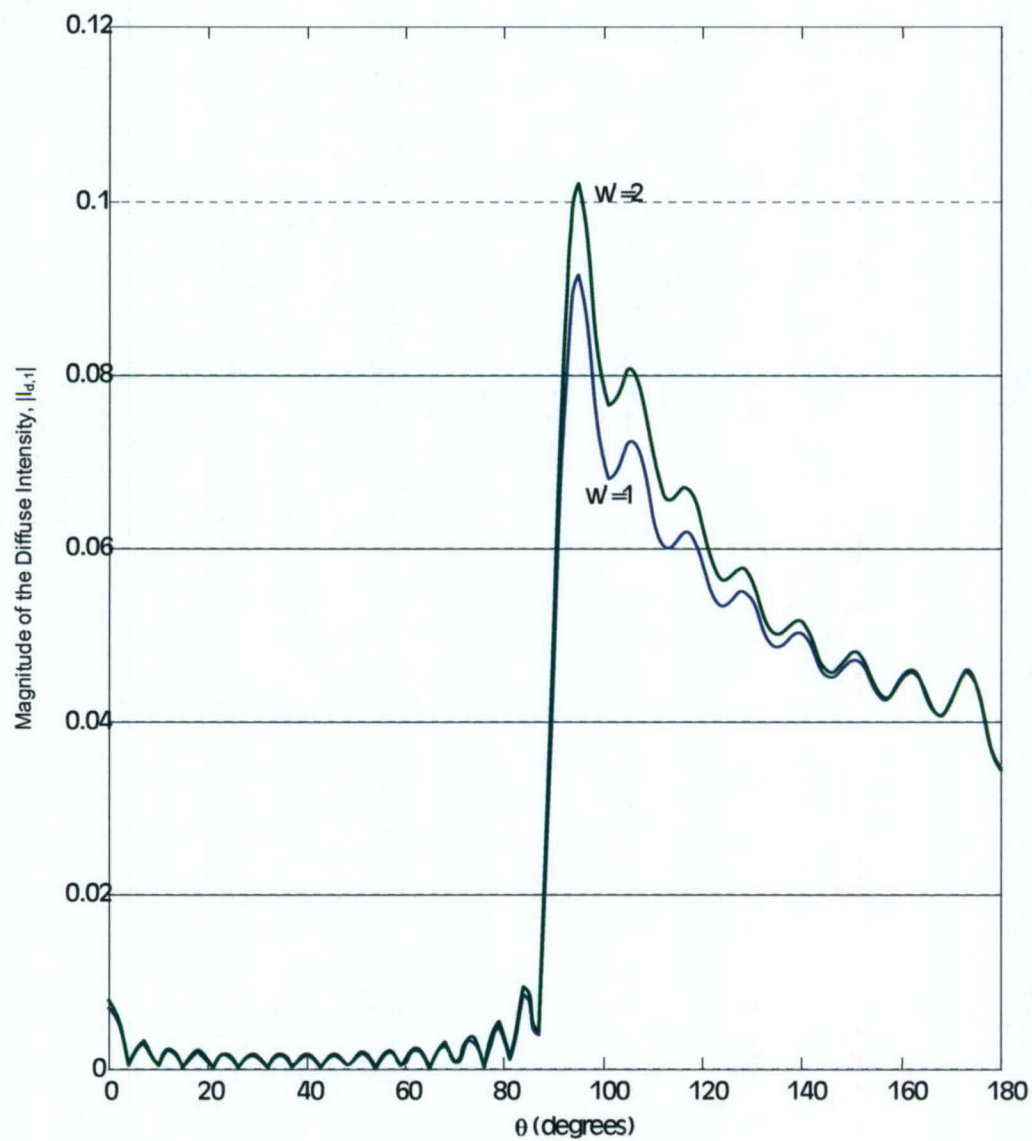


**Figure 6.13** Magnitude of diffuse intensity  $|I_{d,1}|$  versus  $\theta$  for  $w'=1, 2$  and  $\rho'=0, z'=0, \nu=1, N=31$ .

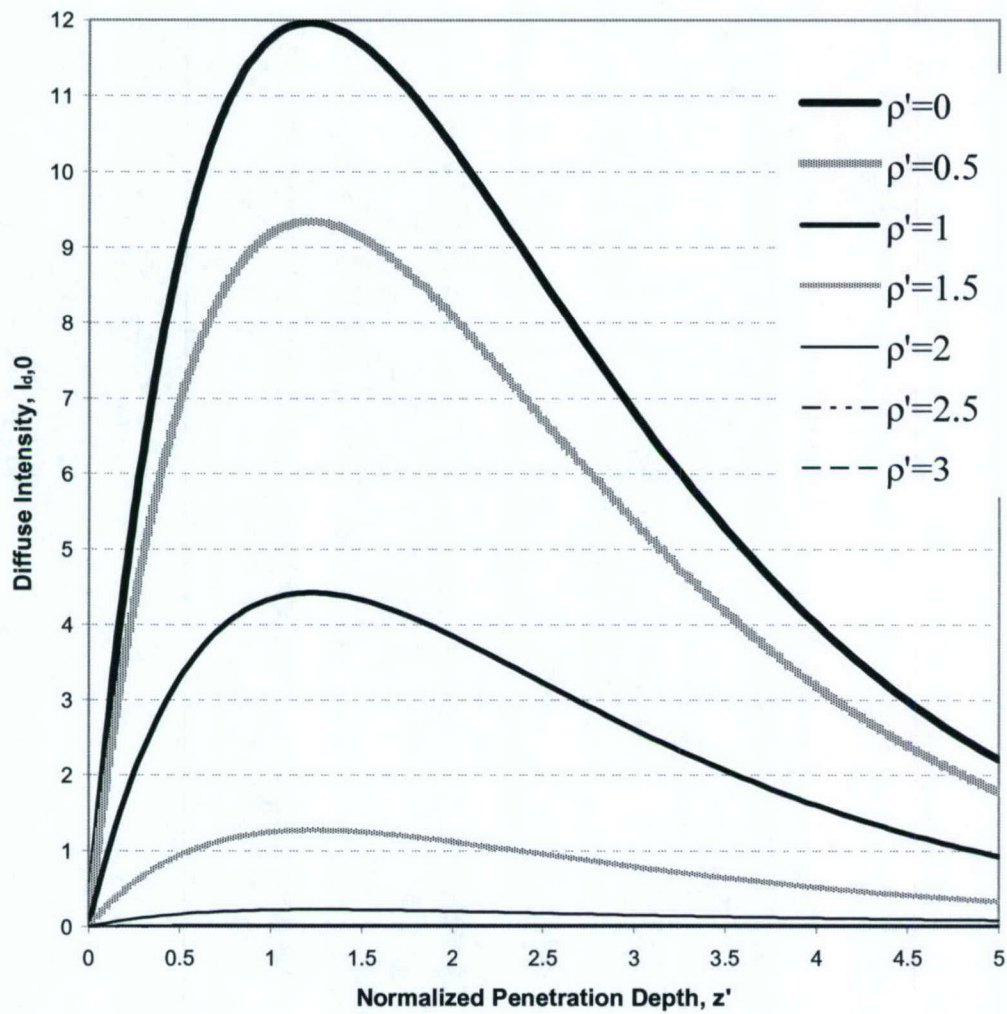


**Figure 6.14** Diffuse Intensity  $I_{d,0}$  versus normalized penetration depth  $z'$  for  $w'=1$ ,  $\rho'=0$ ,  $\theta=0$ ,  $\nu=0$ ,  $N=31$ .

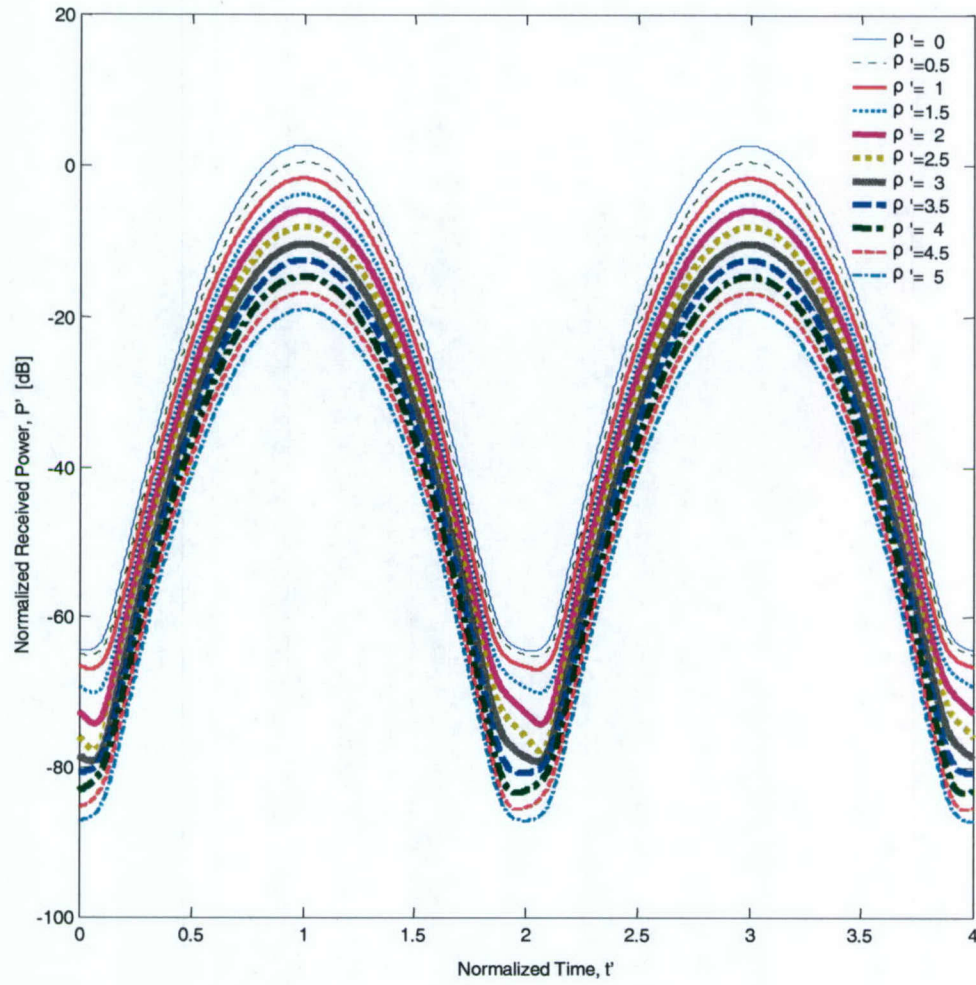


**Figure 6.15** Normalized received power  $P'$  versus normalized time  $t'$  for  $\rho'$  varying from 0 to 5 and  $w' = 1$ ,  $z' = 1$ ,  $\theta_M = 0$ ,  $\psi_M = 0$ ,  $v_{\max} = 15$ ,  $N = 31$ .



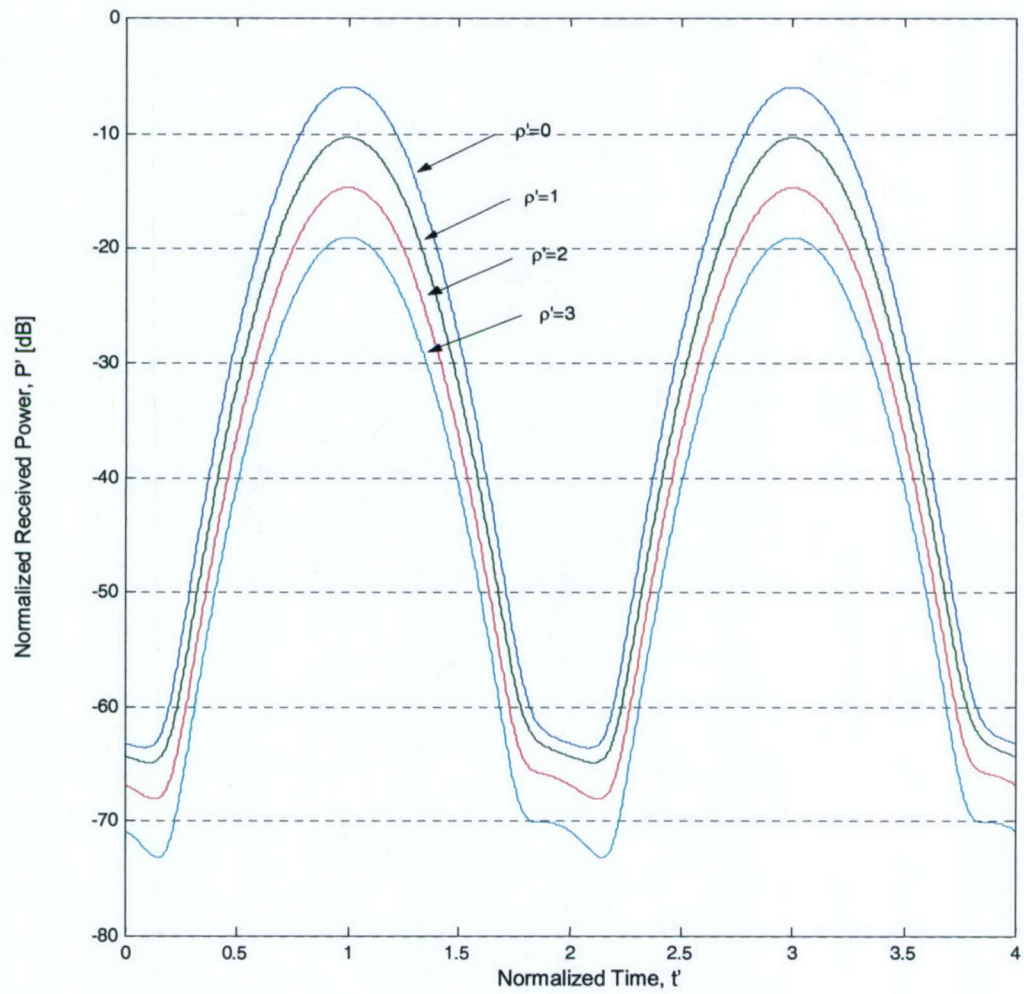


**Figure 6.16** Normalized received power  $P'$  versus normalized time  $t'$  for  $\rho' = 0, 1, 2, 3$  and  $w' = 1$ ,  $z' = 3$ ,  $\theta_M = 0$ ,  $\psi_M = 0$ ,  $v_{\max} = 15$ ,  $N = 27$ .

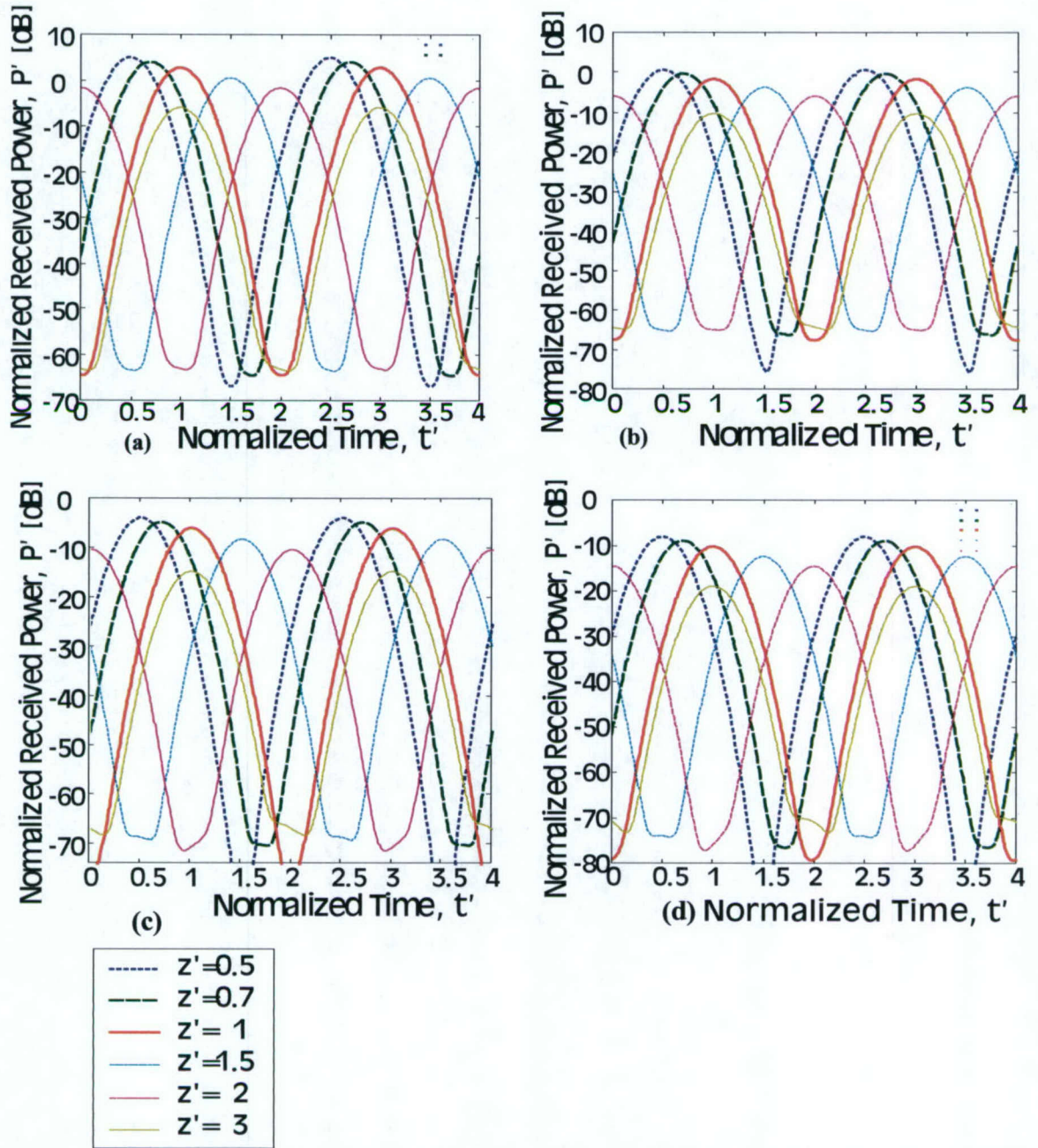
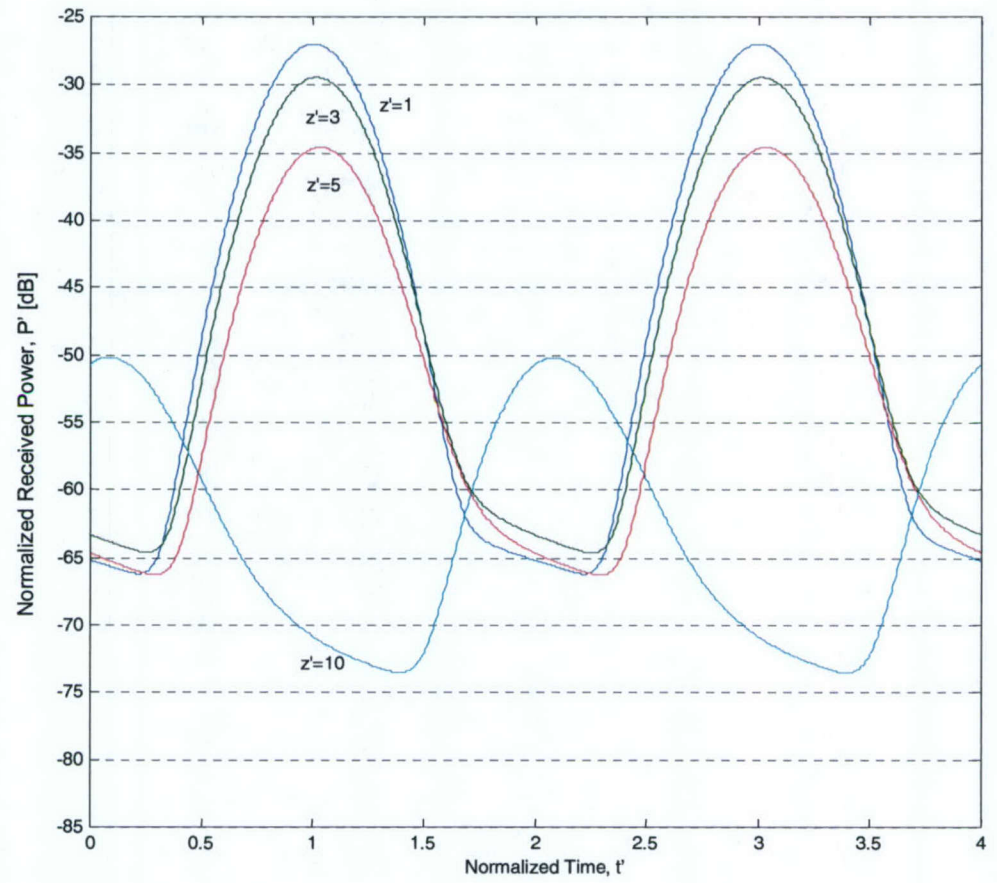
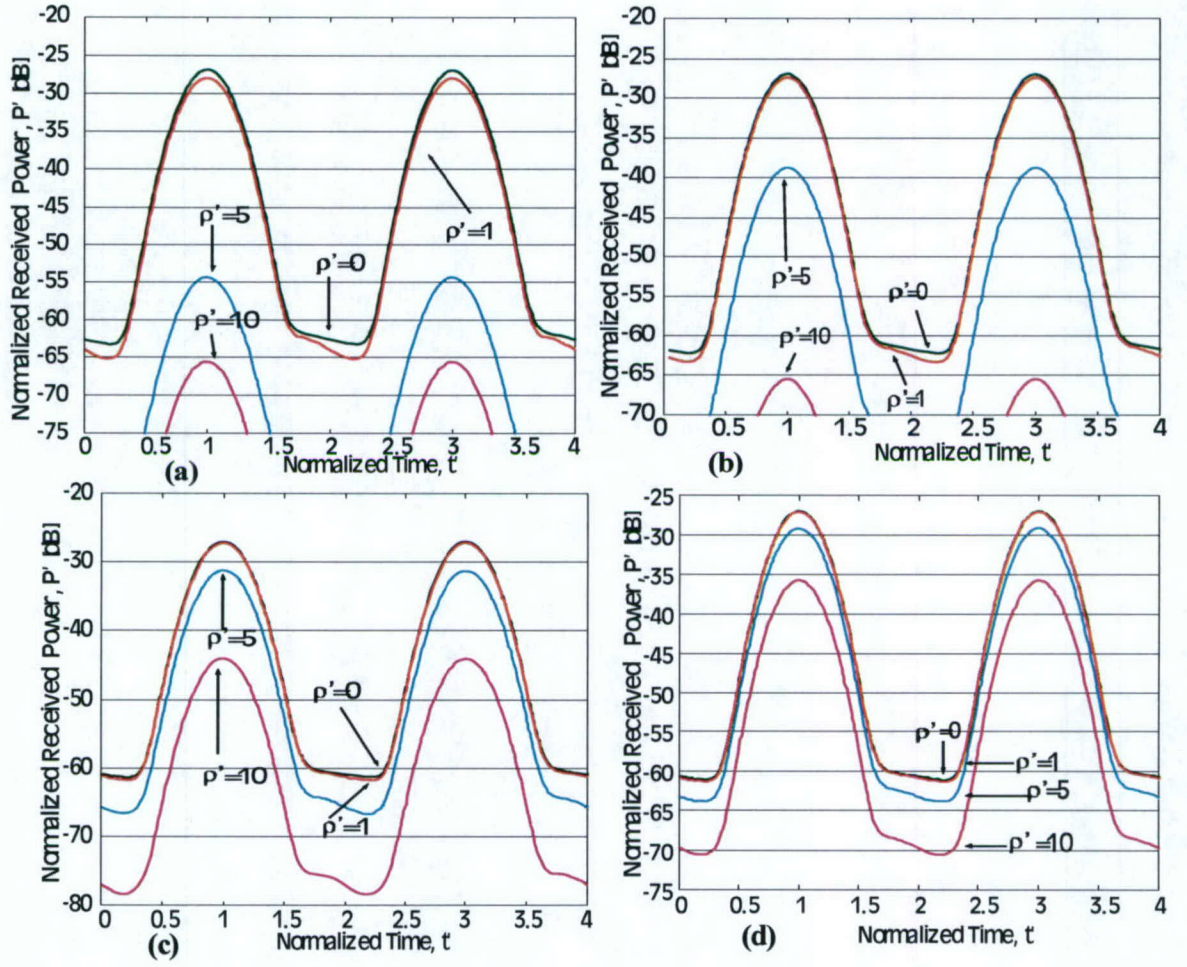


Figure 6.17 Normalized received power  $P'$  versus normalized time  $t'$  for  $z'=0.5, 0.7, 1, 1.5, 2, 3$  and  $w'=1, \theta_M=0, \psi_M=0, \nu_{\max}=15, N=27$ , (a)  $\rho'=0$ , (b)  $\rho'=1$ , (c)  $\rho'=2$ , (d)  $\rho'=3$ .



**Figure 6.18** Normalized received power  $P'$  versus normalized time  $t'$  for  $z'=1,3,5,10$  and  $w'=1$ ,  $\rho'=0$ ,  $\theta_M=4.83^\circ$ ,  $\psi_M=0$ ,  $v_{\max}=15$ ,  $N=27$ .





**Figure 6.19** Normalized received power  $P'$  versus normalized time  $t'$  for (a)  $w' = 2$ , (b)  $w' = 3$ , (c)  $w' = 5$ , (d)  $w' = 7$  with  $\rho' = 0, 1, 5, 10$  and for  $z' = 1$ ,  $\theta_M = 4.83^\circ$ ,  $\psi_M = 0$ ,  $v_{\max} = 15$ ,  $N = 27$ .

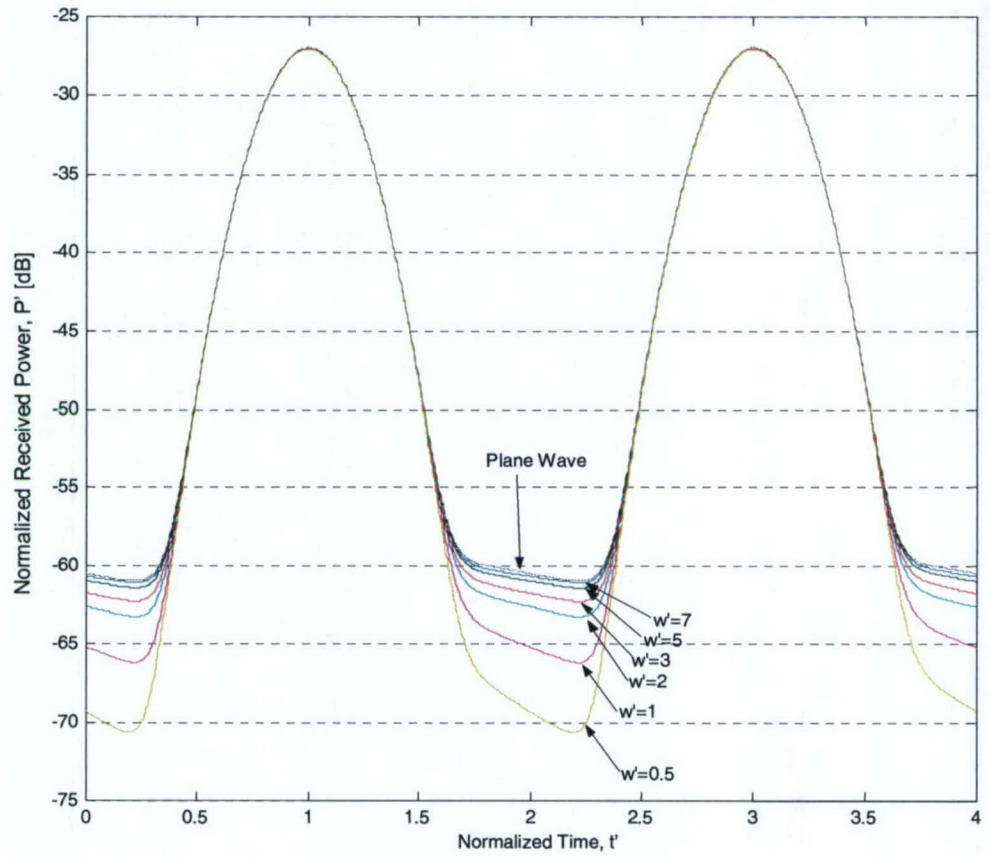


**Figure 6.20** Normalized received power  $P'_d$  versus normalized time  $t'$  for collimated beam wave with beamwidths  $w'=0.5, 1, 2, 3, 5, 7$  and for a plane wave ( $w' \rightarrow \infty$ ),  $\rho=0$ ,  $z'=1$ ,  $\theta_M=4.83^\circ$ ,  $\nu_{\max}=15$ ;  $N=31$  for the plane wave case and  $N=27$  for collimated beam waves.

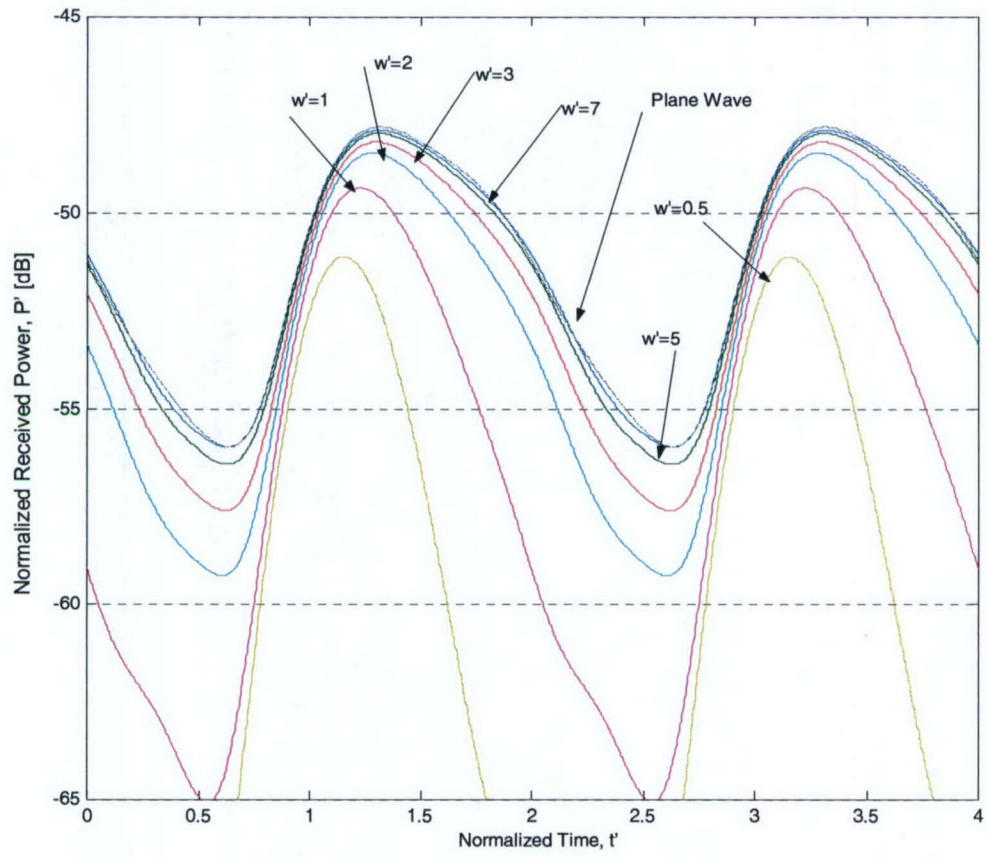


**Figure 6.21** Normalized received power  $P'$  versus normalized time  $t'$  for collimated beam waves with beamwidths  $w'=0.5, 1, 2, 3, 5, 7$  and for a plane wave ( $w' \rightarrow \infty$ ),  $\rho=0$ ,  $z'=1$ ,  $\theta_M=62^\circ$ ,  $\nu_{\max}=15$ ,  $N=31$  for the plane wave case and  $N=27$  for collimated beam waves.



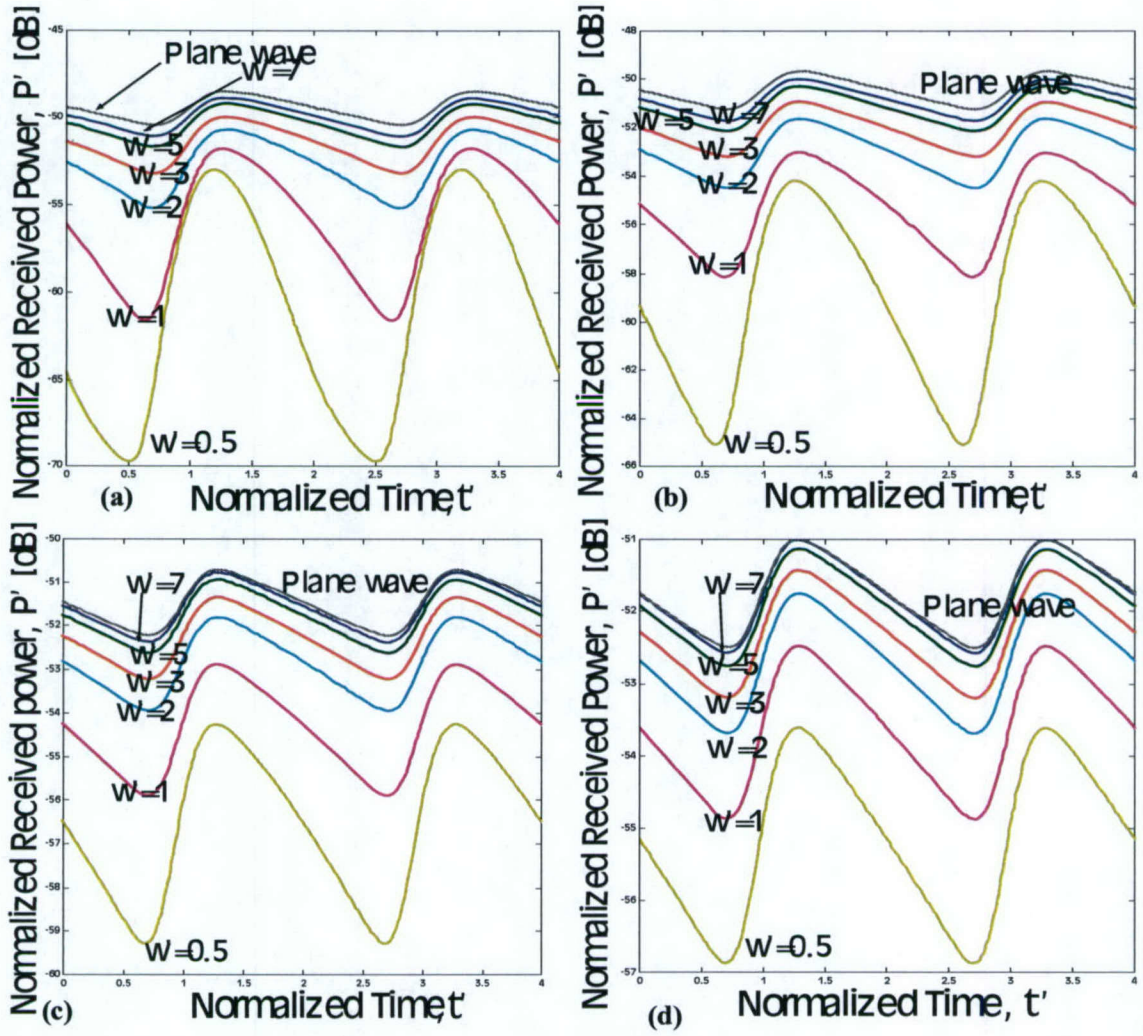


**Figure 6.22** Normalized received power  $P'$  versus normalized time  $t'$  for collimated beam waves with beamwidths  $w' = 0.5, 1, 2, 3, 5, 7$  and for a plane wave ( $w' \rightarrow \infty$ ),  $\rho = 0$ ,  $z' = 1$ , (a)  $\theta_M = 87^\circ$ , (b)  $\theta_M = 118^\circ$ , (c)  $\theta_M = 150^\circ$ , (d)  $\theta_M = 175^\circ$ ,  $\nu_{\max} = 15$ ,  $N = 31$  for the plane wave case and  $N = 27$  for collimated beam waves.

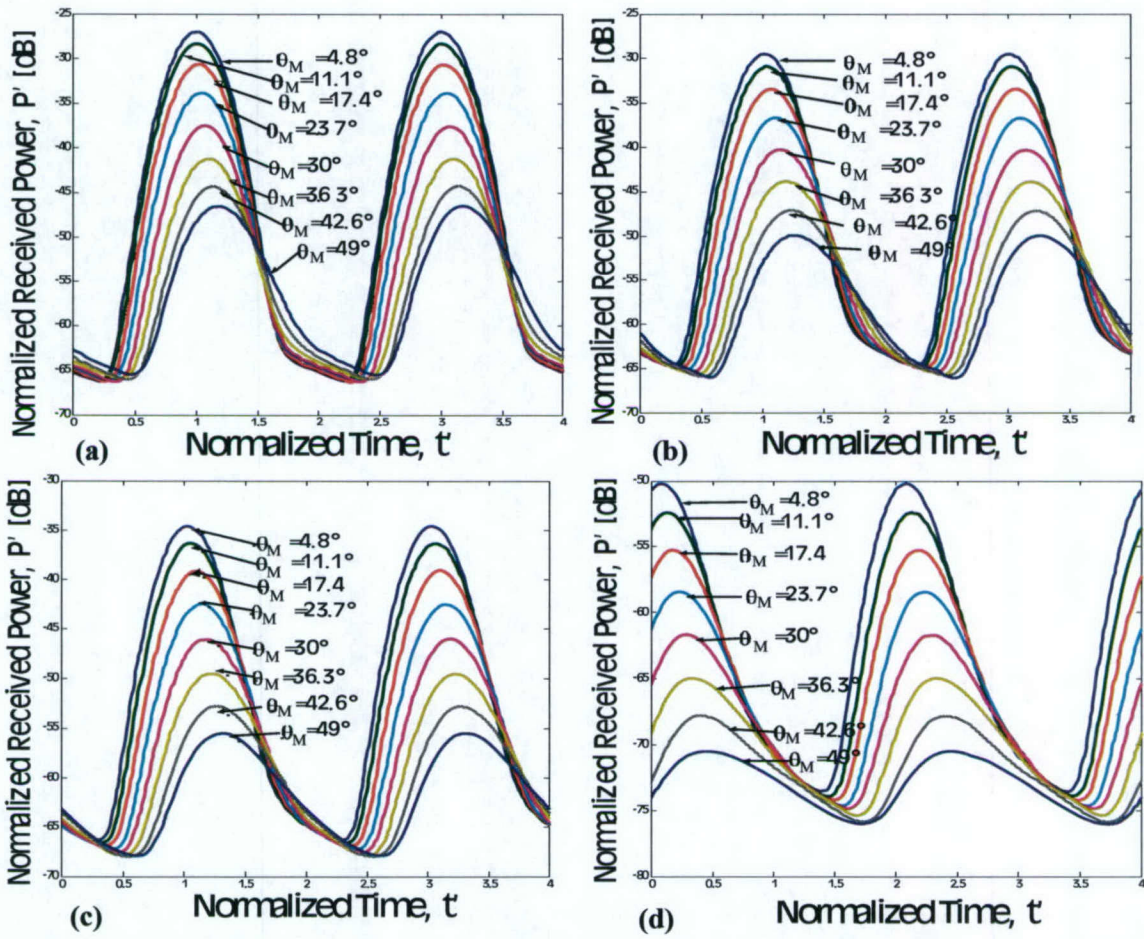
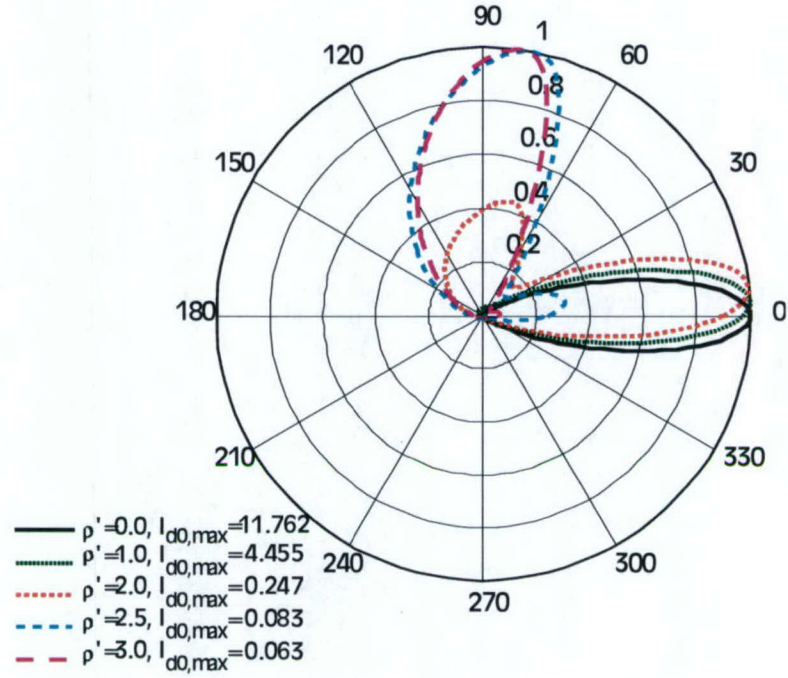
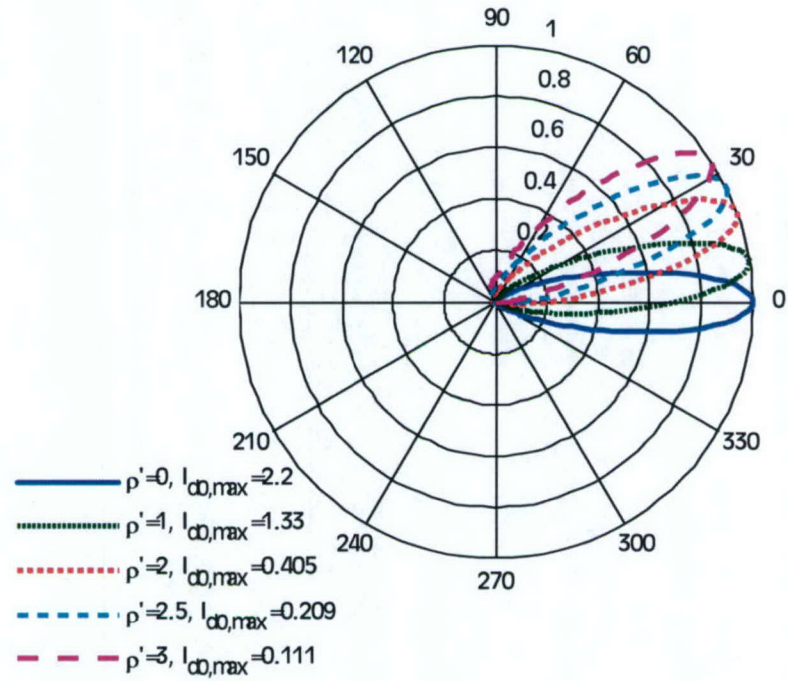


**Figure 6.23** Normalized received power  $P'$  versus normalized time  $t'$  for different values of  $\theta_M$  and for (a)  $z'=1$ , (b)  $z'=3$ , (c)  $z'=5$ , and (d)  $z'=10$  with  $w'=1$ ,  $\rho'=0$ ,  $\nu_{\max}=15$ ,  $N=27$ .





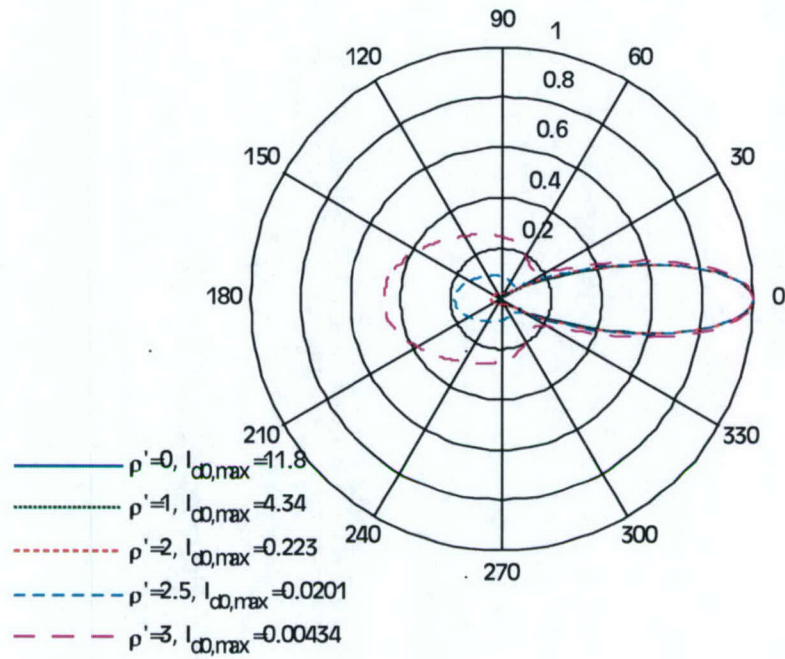
(a)



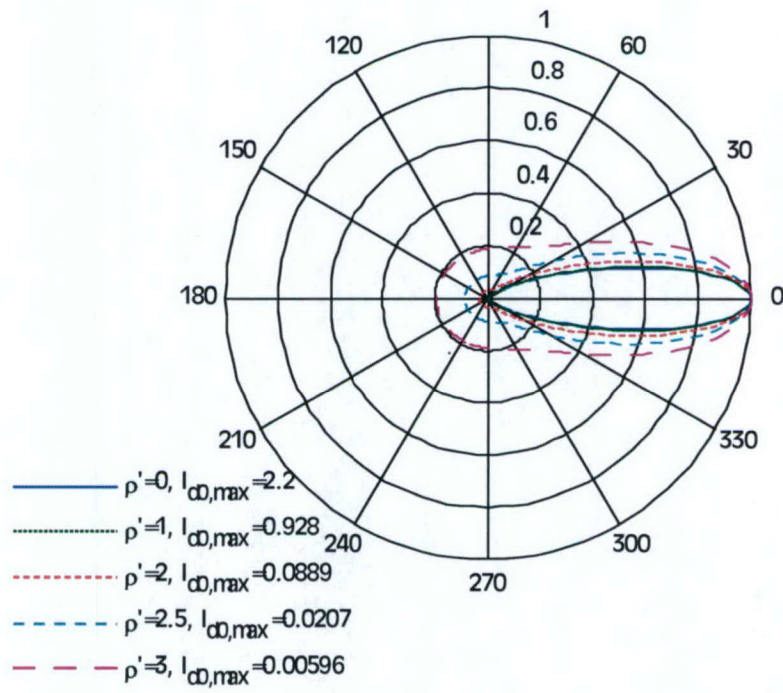
(b)

**Figure 6.24** Diffuse Intensity  $I_{d,0}$  vs  $\theta$  for  $\rho' = 0, 1, 2, 2.5, 3$  at (a)  $z'=1$  and (b)  $z'=5$  with  $w'=1$ ,  $\psi = 0, \pi$  and  $N=31$ .



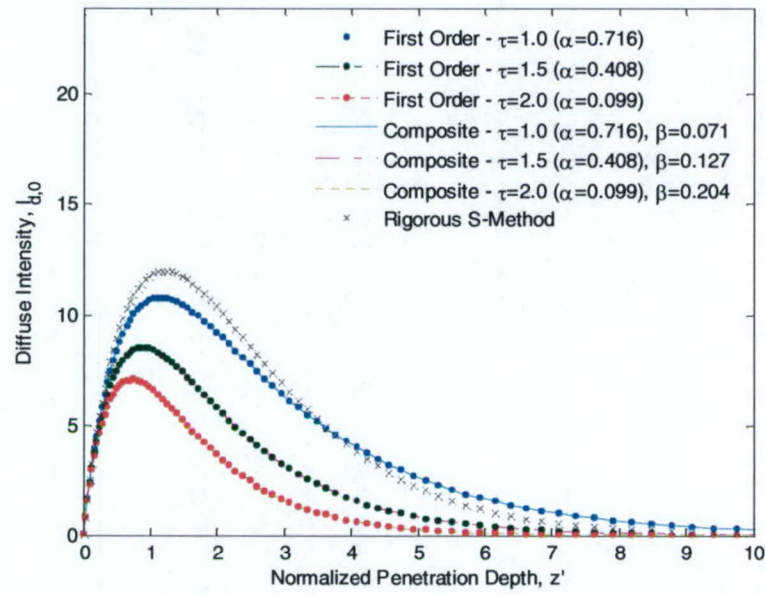


(a)

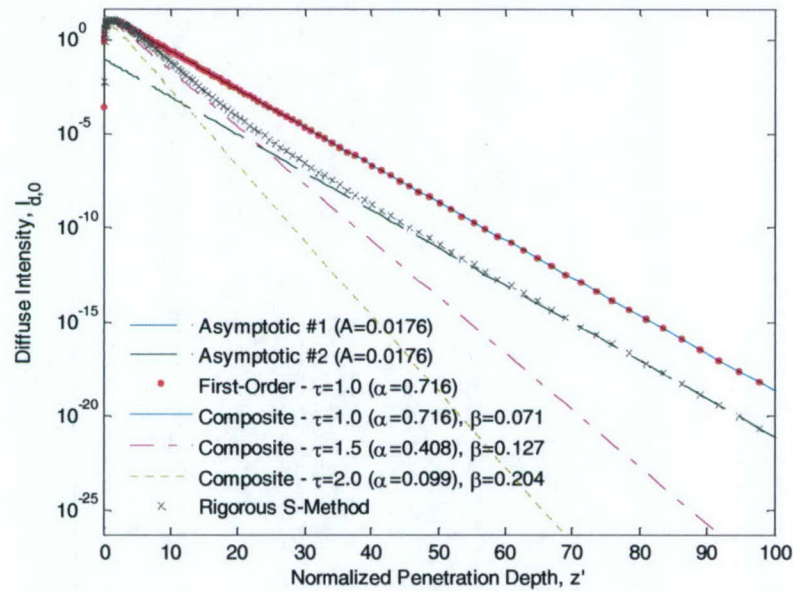


(b)

**Figure 6.25** Diffuse Intensity  $I_{d,0}$  vs  $\theta$  for  $\rho' = 0, 1, 2, 2.5, 3$  at (a)  $z'=1$  and (b)  $z'=5$  with  $w'=1$ ,  $\psi = -\pi/2, \pi/2$  and  $N=31$ .

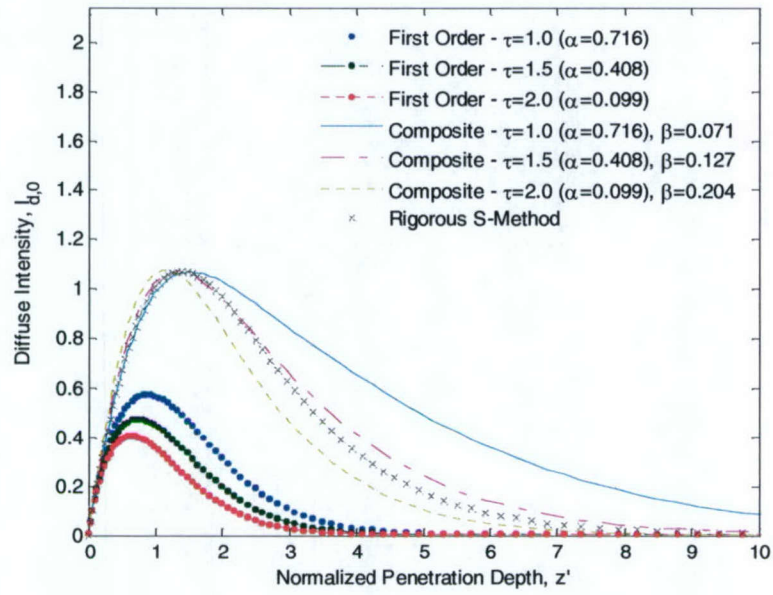


(a)

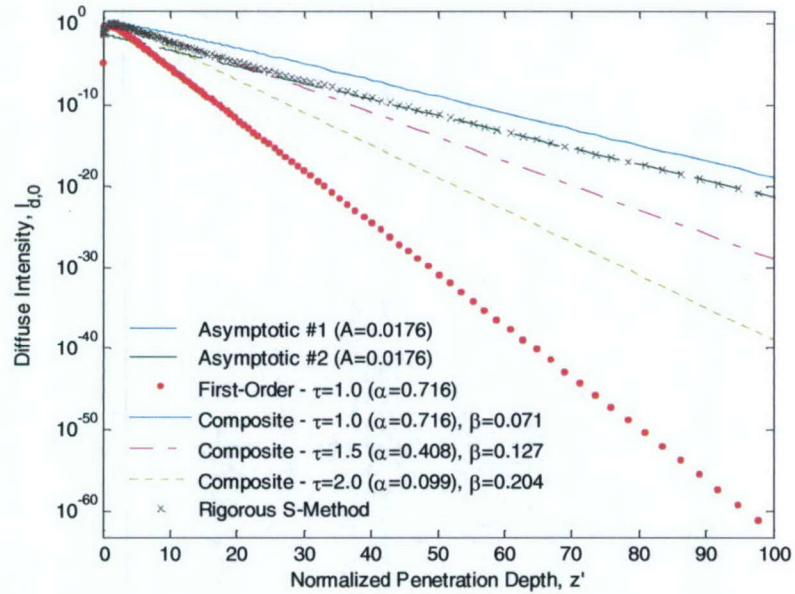


(b)

**Figure 6.26** Diffuse Intensity  $I_{d,0}$  vs normalized penetration depth  $z'$  for the collimated beam case using the rigorous and approximate solutions for  $\rho' = 0$  and  $\theta = 0^\circ$  for (a)  $0 \leq z' \leq 10$  and (b)  $0 \leq z' \leq 100$  with  $w' = 1$ ,  $\psi = 0$  and  $N = 31$ . Note that the values of  $\beta$  do not apply in this case.



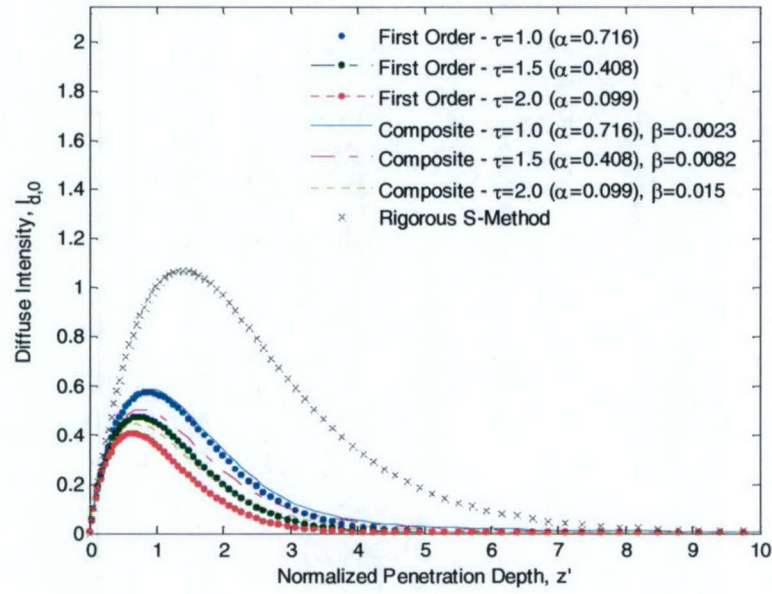
(a)



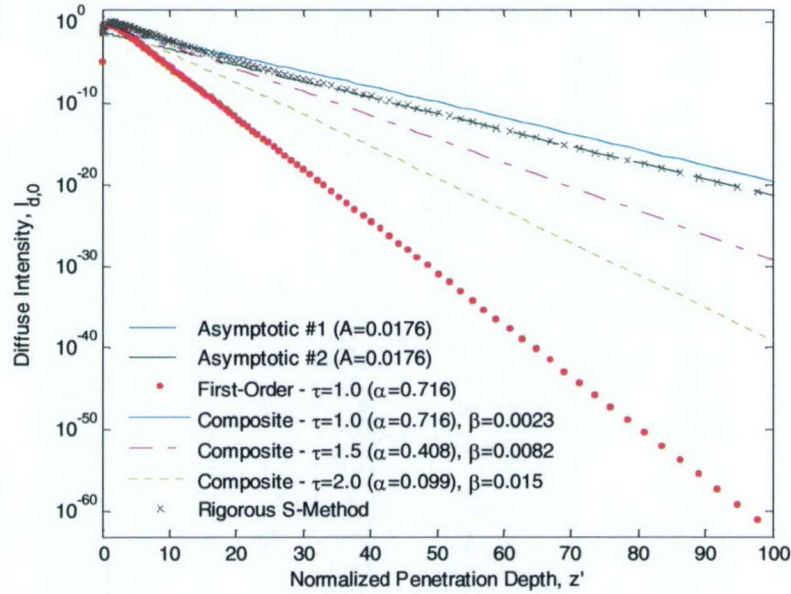
(b)

**Figure 6.27** Diffuse Intensity  $I_{d,0}$  vs normalized penetration depth  $z'$  for the collimated beam case using the rigorous and approximate solutions for  $\rho' = 0$  and  $\theta = 30^\circ$  for (a)  $0 \leq z' \leq 10$  and (b)  $0 \leq z' \leq 100$  with  $w' = 1$ ,  $\psi = 0$  and  $N = 31$ . Note that the values of  $\beta$  are chosen to optimize the composite solution in this case.



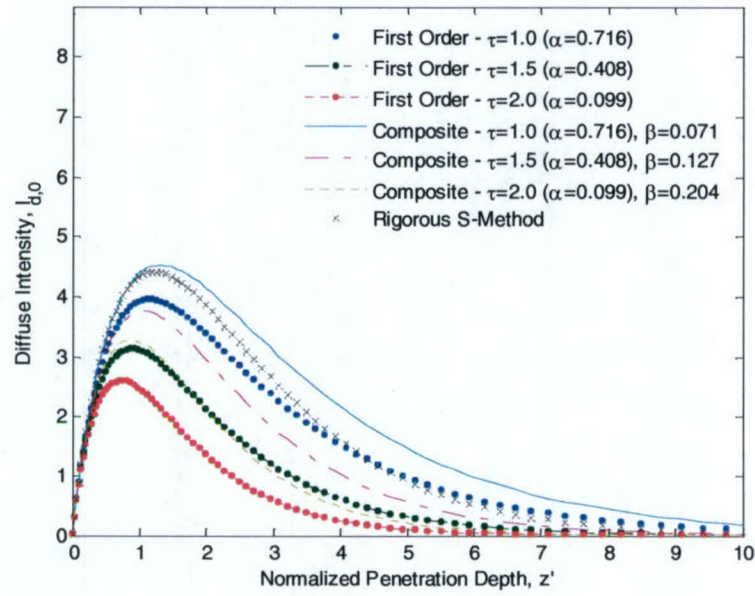


(a)

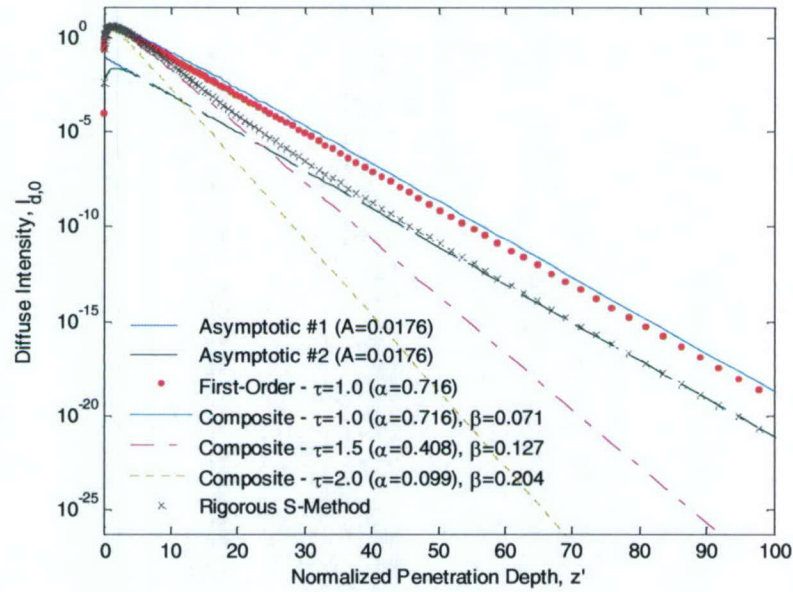


(b)

**Figure 6.28** Diffuse Intensity  $I_{d,0}$  vs normalized penetration depth  $z'$  for the collimated beam case using the rigorous and approximate solutions for  $\rho' = 0$  and  $\theta = 30^\circ$  for (a)  $0 \leq z' \leq 10$  and (b)  $0 \leq z' \leq 100$  with  $w' = 1$ ,  $\psi = 0$  and  $N = 31$ . Note that the values of  $\beta$  are chosen to optimize the composite solution for  $\rho' = 2$  and  $\theta = 0^\circ$  in Figure 6.34.

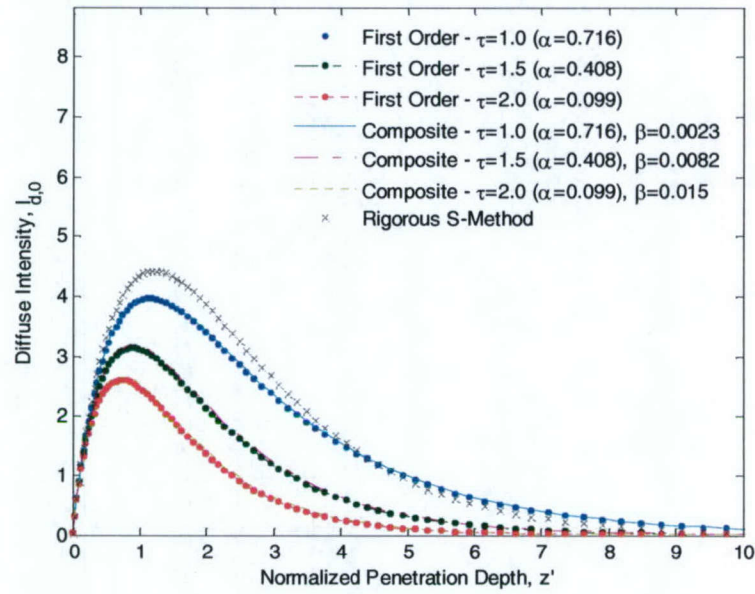


(a)

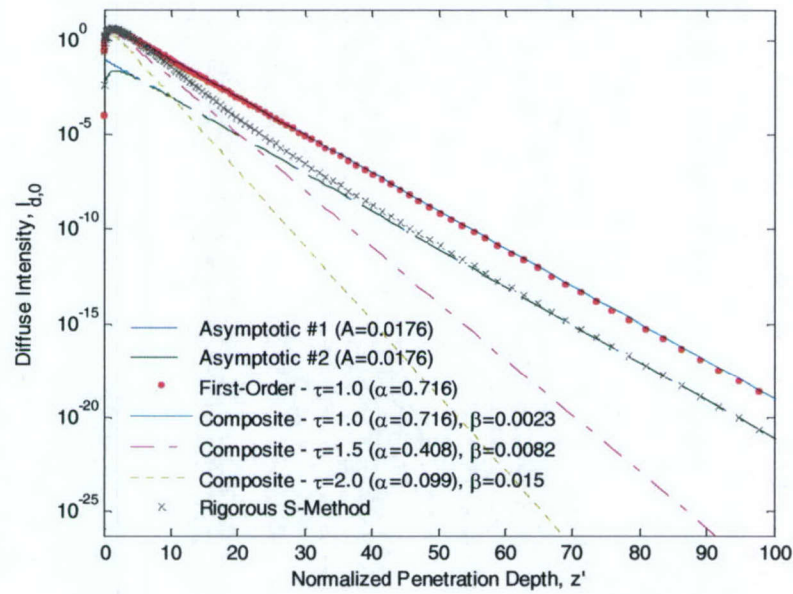


(b)

**Figure 6.29** Diffuse Intensity  $I_{d,0}$  vs normalized penetration depth  $z'$  for the collimated beam case using the rigorous and approximate solutions for  $\rho' = 1$  and  $\theta = 0^\circ$  for (a)  $0 \leq z' \leq 10$  and (b)  $0 \leq z' \leq 100$  with  $w' = 1$ ,  $\psi = 0$  and  $N = 31$ . Note that the values of  $\beta$  are chosen to optimize the composite solution for  $\rho' = 0$  and  $\theta = 30^\circ$  in Figure 6.27.



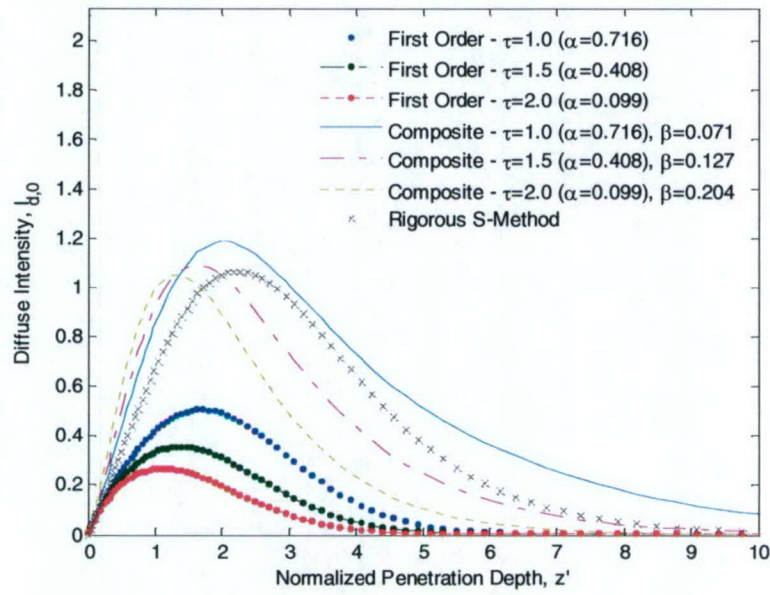
(a)



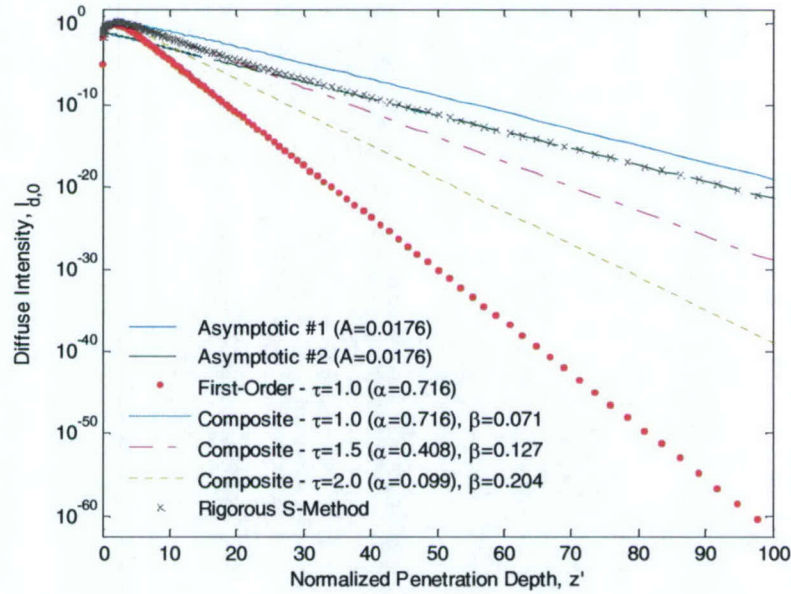
(b)

**Figure 6.30** Diffuse Intensity  $I_{d,0}$  vs normalized penetration depth  $z'$  for the collimated beam case using the rigorous and approximate solutions for  $\rho' = 1$  and  $\theta = 0^\circ$  for (a)  $0 \leq z' \leq 10$  and (b)  $0 \leq z' \leq 100$  with  $w' = 1$ ,  $\psi = 0$  and  $N = 31$ . Note that the values of  $\beta$  are chosen to optimize the composite solution for  $\rho' = 2$  and  $\theta = 0^\circ$  in Figure 6.34.



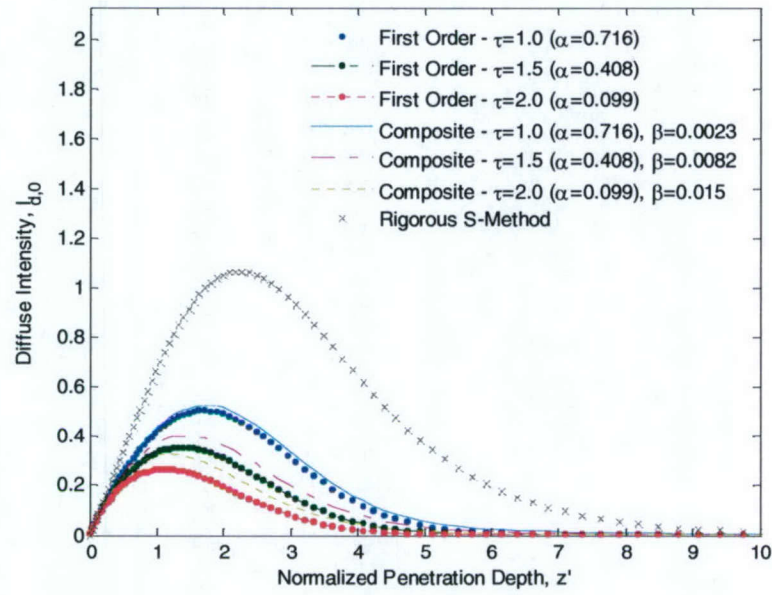


(a)

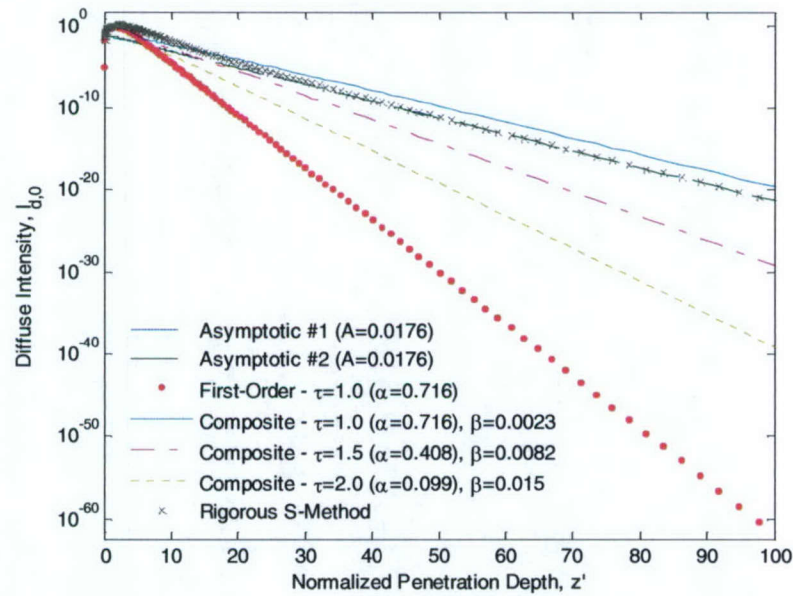


(b)

**Figure 6.31** Diffuse Intensity  $I_{d,0}$  vs normalized penetration depth  $z'$  for the collimated beam case using the rigorous and approximate solutions for  $\rho' = 1$  and  $\theta = 30^\circ$  for (a)  $0 \leq z' \leq 10$  and (b)  $0 \leq z' \leq 100$  with  $w' = 1$ ,  $\psi = 0$  and  $N = 31$ . Note that the values of  $\beta$  are chosen to optimize the composite solution for  $\rho' = 0$  and  $\theta = 30^\circ$  in Figure 6.27.

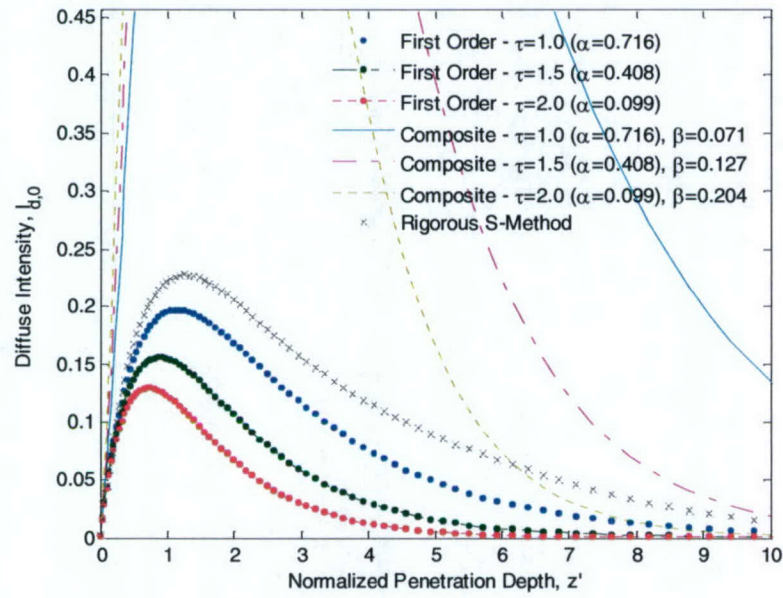


(a)

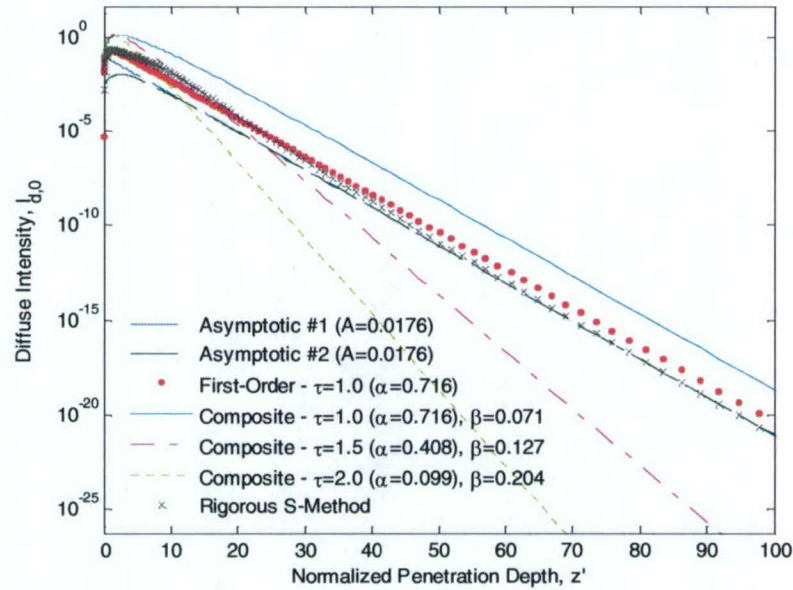


(b)

**Figure 6.32** Diffuse Intensity  $I_{d,0}$  vs normalized penetration depth  $z'$  for the collimated beam case using the rigorous and approximate solutions for  $\rho' = 1$  and  $\theta = 30^\circ$  for (a)  $0 \leq z' \leq 10$  and (b)  $0 \leq z' \leq 100$  with  $w' = 1$ ,  $\psi = 0$  and  $N = 31$ . Note that the values of  $\beta$  are chosen to optimize the composite solution for  $\rho' = 2$  and  $\theta = 0^\circ$  in Figure 6.34.



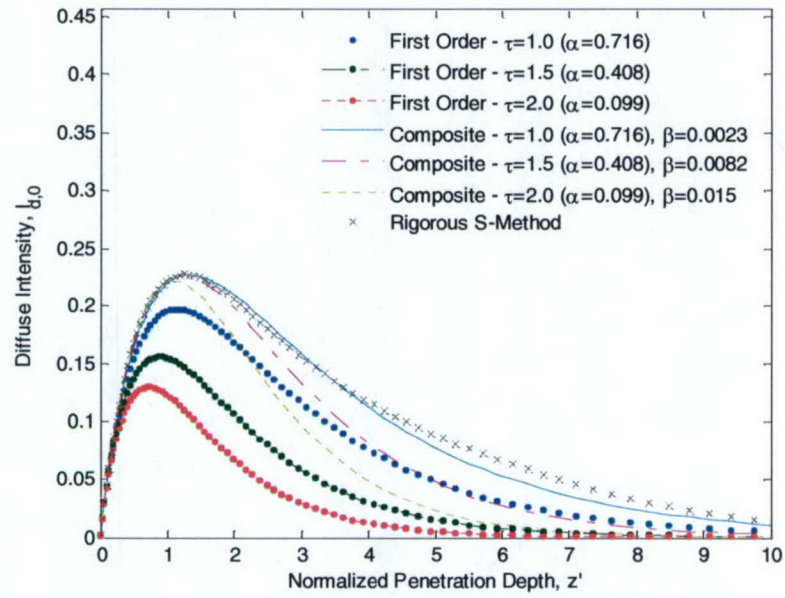
(a)



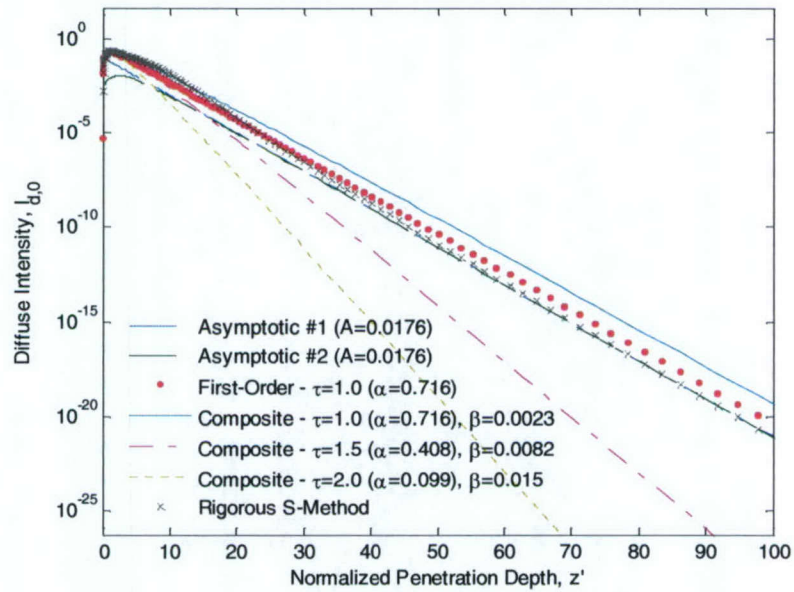
(b)

**Figure 6.33** Diffuse Intensity  $I_{d,0}$  vs normalized penetration depth  $z'$  for the collimated beam case using the rigorous and approximate solutions for  $\rho' = 2$  and  $\theta = 0^\circ$  for (a)  $0 \leq z' \leq 10$  and (b)  $0 \leq z' \leq 100$  with  $w' = 1$ ,  $\psi = 0$  and  $N = 31$ . Note that the values of  $\beta$  are chosen to optimize the composite solution for  $\rho' = 0$  and  $\theta = 30^\circ$  in Figure 6.27.



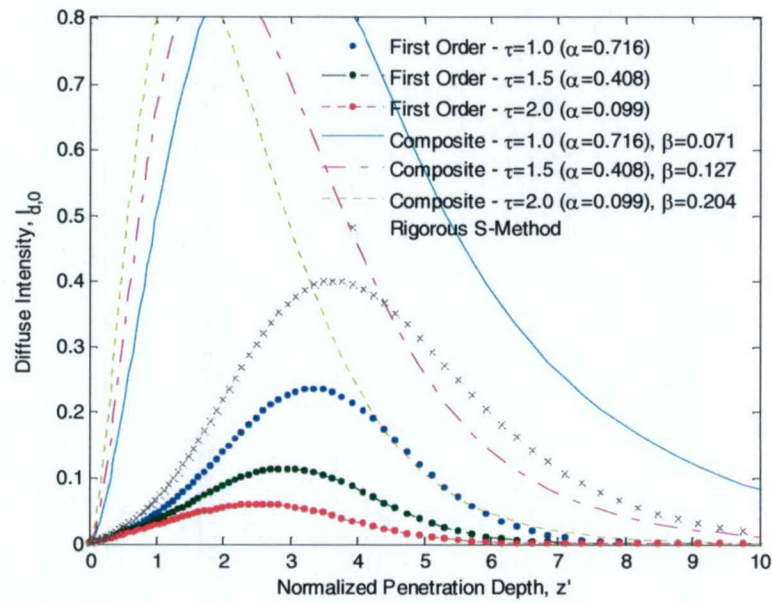


(a)

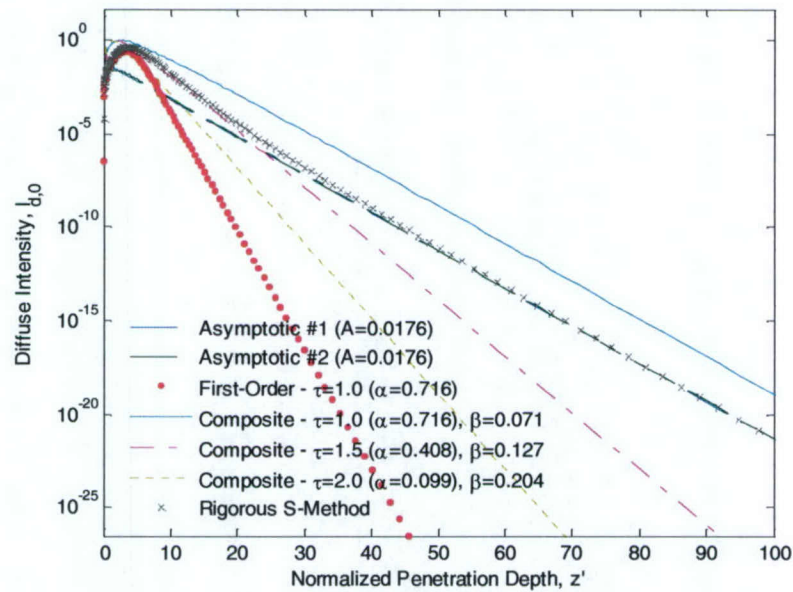


(b)

**Figure 6.34** Diffuse Intensity  $I_{d,0}$  vs normalized penetration depth  $z'$  for the collimated beam case using the rigorous and approximate solutions for  $\rho' = 2$  and  $\theta = 0^\circ$  for (a)  $0 \leq z' \leq 10$  and (b)  $0 \leq z' \leq 100$  with  $w' = 1$ ,  $\psi = 0$  and  $N = 31$ . Note that the values of  $\beta$  are chosen to optimize the composite solution in this case.

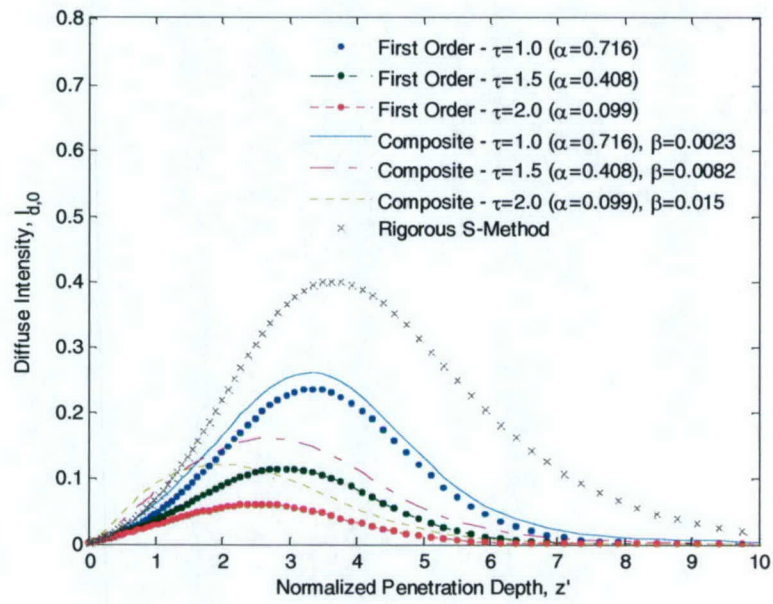


(a)

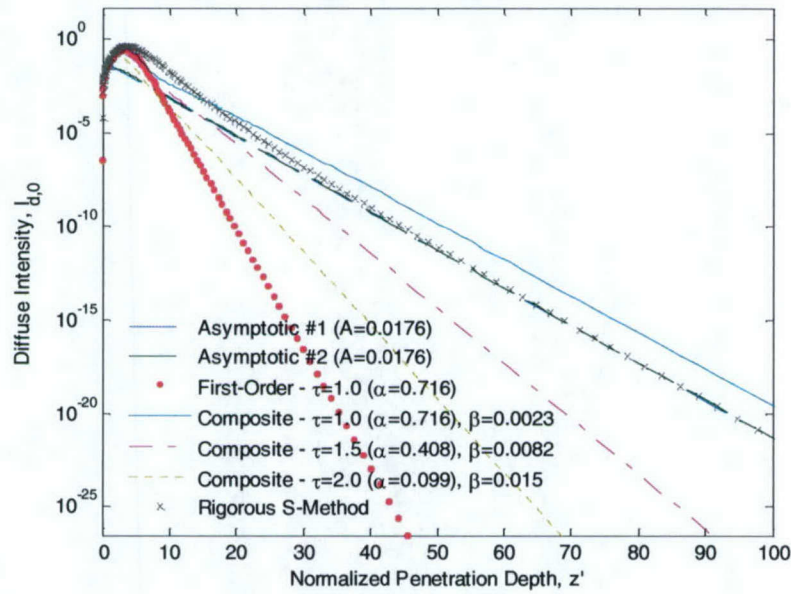


(b)

**Figure 6.35** Diffuse Intensity  $I_{d,0}$  vs normalized penetration depth  $z'$  for the collimated beam case using the rigorous and approximate solutions for  $\rho' = 2$  and  $\theta = 30^\circ$  for (a)  $0 \leq z' \leq 10$  and (b)  $0 \leq z' \leq 100$  with  $w' = 1$ ,  $\psi = 0$  and  $N = 31$ . Note that the values of  $\beta$  are chosen to optimize the composite solution for  $\rho' = 0$  and  $\theta = 30^\circ$  in Figure 6.27.



(a)



(b)

**Figure 6.36** Diffuse Intensity  $I_{d,0}$  vs normalized penetration depth  $z'$  for the collimated beam case using the rigorous and approximate solutions for  $\rho' = 2$  and  $\theta = 30^\circ$  for (a)  $0 \leq z' \leq 10$  and (b)  $0 \leq z' \leq 100$  with  $w' = 1$ ,  $\psi = 0$  and  $N = 31$ . Note that the values of  $\beta$  are chosen to optimize the composite solution for  $\rho' = 2$  and  $\theta = 0^\circ$  in Figure 6.34.